VILNIUS UNIVERSITY
NATIONAL CENTER FOR PHYSICAL SCIENCE AND TECHNOLOGY

Saulius
Daugėla

Transport of Lithium and Sodium Cations in Solid Electrolytes

DOCTORAL DISSERTATION

Technological Sciences,
Material Engineering T008

VILNIUS 2019

This dissertation was written between 2015 and 2019 at Vilnius University.
The research was supported by Research Council of Lithuania.

Academic supervisor:
Assoc. Prof. Dr. Tomas Šalkus (Vilnius University, Technological sciences, Materials engineering – T008).

VILNIAUS UNIVERSITETAS
NACIONALINIS FIZINIŲ IR TECHNOLOGIJOS MOKSLŲ CENTRAS

Saulius
Daugėla

Ličio ir natrio katijonų pernaša kietuosiuose elektrolituose

DAKTARO DISERTACIJA

Technologijos mokslai,
medžiagų inžinerija T008

VILNIUS 2019

Disertacija rengta 2015–2019 metais Vilniaus universitete.
Mokslinius tyrimus rėmė Lietuvos mokslo taryba.

Mokslinis vadovas:
doc. dr. Tomas Šalkus (Vilniaus universitetas, technologijos mokslai, medžiagų inžinerija – T008)

ACKNOWLEDGEMENTS

I would like to thank to my scientific supervisor Dr. Tomas Šalkus for patient guidance and support that he has provided throughout the period of my PhD studies. I would also like to thank him for numerous consultations, responded questions and all valuable scientific advices.

I am also especially grateful to prof. Algimantas Kežionis for the impedance spectroscopy measurements and all scientific explanations that helped me to understand the research area better.

My sincere thanks to other collaborators of our group at Vilnius University – prof. Antanas Feliksas Orliukas, Dr. Edvardas Kazakevičius, Dr. Saulius Kazlauskas and Dr. Vilma Kavaliukė – for the sharing experience and help with the experiments.

Acknowledgements also to my collaborators from other departments and universities of Lithuania – Dr. A. Maneikis, Dr. M. Lelis, and Dr. V. Jasiulaitienė, – and to my foreign colleagues: Dr. A. Dindune, Dr. D. Valdniece, Dr. J. Ronis, Dr. T. Pietrzak, Dr. M. Barre, Dr. A. G. Belous, Dr. O. I. V'yunov, Dr. S. D. Kobylianska, Dr. L. O. Vasylechko, and Dr. M. Mosialek. Their help and advices made my studies more perspicuous and engrossing, and so my PhD thesis more intelligible and reliable.

I am also very grateful to prof. R. Grigalaitis and Dr. R. Butkutė for deep study of this thesis and providing insightful comments and suggestions that have made this work stronger, and to our department's head prof. J. Matukas who cared much about my academic needs.

I would also especially thank to my family for every kind of support during my PhD studies.

CONTENTS

ABBREVIATIONS

1D – one dimensional
2D – two dimensional
3D – three dimensional
AC – alternating current
ASSB – all solid state battery
bcc – body centered cubic
CPE – constant phase element
CV – cyclic voltammetry
DC – direct current
DSC – differential scanning calorimetry
DTA – differential thermal analysis
EDX – energy dispersive X-ray
fcc –face centered cubic
hcp – hexagonal close packed
IS – impedance spectroscopy
LCO – lithium cobalt oxide
LIPON – lithium phosphorus oxy-nitride
LISICON –lithium super-ionic conductors
LLNbO – lithium lantanum niobate oxide
LLTO – lithium lanthanum titanium oxide
LLZ – lithium lanthanum zirconium (oxide)
LLZO – lithium lanthanum zirconium oxide
LNLTO – lithium lanthanum titanium oxide doped with sodium (Na)
LSTH – lithium strontium hafnium tantalum (oxide)
LSTZ – lithium strontium tantalum zirconium (oxide)
LTO – lithium titanate oxide
MOCVD – metal-organic chemical vapour deposition
NASICON – Na super-ionic conductors
NASIGLAS – glasses of NASICON type
PEO – poly-ethylene oxide
RF – radio frequency
RT – room temperature
s. g. – space group
SEM – scanning electron microscopy
SPE – solid polymeric electrolyte
SPS – spark-plasma sintering

TGA – thermogravimetric analysis
TZP – tetragonal polycrystalline zirconium (oxide)
VFT – Vogel–Fulcher–Tammann (equation)
XPS – X-ray photoelectron spectroscopy
XRD – X-ray diffraction
XRF – X-ray fluorescence

INTRODUCTION

Solid state electrolytes have captured the attention of scientists and engineers due to their potential application in various electrochemical devices, such as batteries, fuel cells, gas sensors, capacitors, etc. They are also called superionic conductors or fast ion conductors due to their favourable crystal structure for ion transport and consequently high ionic conductivity, similar to that of conventional liquid electrolytes which have many drawbacks in practical usage and handling. Solid electrolytes can be classified according to their ionic species, such as, Ag^+, Li^+, Na^+, H^+, O^{2-}, F^-, Cl^- and others. Thus far Li^+ solid electrolytes were the most actual ones, because in the several latter decades lithium batteries have been introduced in almost all spheres of science and industry and many attempts of scientific and engineering groups are targeted on developing of reliable Li^+ ion batteries of high electrical capacity. But, nevertheless, the materials which have been used until now are either not efficient enough or they are too expensive or even toxic and, at present, scientists are under the necessity of searching new types of solid electrolytes and, in particular, with cheaper ionic species, such as, sodium. Two groups of solid electrolytes – perovskites and NASICONs (Na super-ionic conductors) – have been well investigated and characterized so far as appropriate ones for solid state batteries. Other groups are less analyzed and investigated and still require much attention on the electrochemical and charge transfer properties within them and that is in particular actual when speaking about Na-ion electrolytes which are very attractive because of their much lower price and high abundance compared to those ones of Li-ion type.

During the period of PhD studies much attention was paid on both Li and Na based solid electrolytes and also on mixed Li^+/Na^+ ion superionics. Mixed electrolytes are very favourable when analyzing the peculiarities of the charge migration within the structure of an electrolyte.

In this PhD thesis two groups of solid electrolytes have been investigated: pyrophosphates and perovskites. The pyrophosphates which have similar structure to NASICONs have been much less investigated until now, – in particular those which are sodium based ones. In this work much attention was paid to the impact of substituting Li by Na and consequently to the influence on the electrical properties due to these cationic exchanges. Another group perovskites which are distinguished by vacancy rich crystal structure have also been investigated in this thesis in terms of Li substituting

by Na. Since lithium ions are mobile ones in this structure, the impact of Li exchange by Na on both the ionic conductivity and charge carrier mobility have been investigated.

The latter tasks and problems were solved by using the advanced material characterization method – impedance spectroscopy (IS). By using this advanced technique the dynamics of mobile ions and the origins of several different processes within materials can be revealed and described by measuring the impedance of a solid electrolyte in a broad frequency range at different temperatures.

Aim. The aim of the dissertation was to investigate Li^+ and Na^+ solid electrolytes and to characterize them in terms of the crystal structure, elemental composition and ion transport properties within them.

Main tasks of this thesis:

1) To synthesize $Na_{2-x}Li_xMnP_2O_7$ (x = 0, 0.25, 0.5, 1.5, 2), $Na_2ZnP_2O_7$, $NaCsMnP_2O_7$, $NaCsZnP_2O_7$, $Na_2Zn_{0.5}Mn_{0.5}P_2O_7$, $NaCsZn_{0.5}Mn_{0.5}P_2O_7$, and $Li_{0.5-y}Na_yLa_{0.5}Nb_2O_6$, powder with different x and y parameters and to prepare ceramics.
2) To investigate the crystal structure of the prepared ceramics by X-ray diffraction method.
3) To analyze the surfaces of the prepared ceramics by X-ray photoelectron spectroscopy.
4) To investigate the electrical properties of the prepared ceramics by impedance spectroscopy in the frequency range from 10 Hz to 3 GHz and the temperature range from 300 K to 800 K.

Scientific novelty:

1) For the first time the electrical properties of $Na_2MnP_2O_7$ were registered and both the phase transition and proton conductivity were confirmed by the method of impedance spectroscopy.
2) New compounds $Na_{2-x}Li_xMnP_2O_7$ (x = 0.0, 0.5, 1.0, 1.5, 2.0), $Na_2ZnP_2O_7$, $NaCsMnP_2O_7$, $NaCsZnP_2O_7$, $Na_2Zn_{0.5}Mn_{0.5}P_2O_7$, and $NaCsZn_{0.5}Mn_{0.5}P_2O_7$ have been synthesized and investigated by XRD and IS.
3) For the first time $Li_{0.5-y}Na_yLa_{0.5}Nb_2O_6$ (y = 0.0, 0.1, 0.2, 0.3, 0.4, 0.5) ceramics have been investigated in the broad frequency range from 10 Hz to 3 GHz at high temperatures.
4) For the first time the anomalies of the lattice parameters with temperature in $NaCsMnP_2O_7$ (400-500 K) and $Cs_2MnP_4O_{12}$ (500-600 K) and their influence on the electrical parameters were found.

5) For the first time the electrical properties of $NaLiMnP_2O_7$ were registered and the phase transition in $Na_2Mn_3(P_2O_7)_2$ phase was confirmed by the methods of impedance spectroscopy and differential thermal analysis.

Statements presented for the defence:

1. A reversible phase transition takes place in $Na_2MnP_2O_7$ ceramics in 630-660 K temperature interval. $Na_2MnP_2O_7$ phase transition can be detected by impedance spectroscopy in the mixed phase compounds and reveals as the change of conductivity activation energy.
2. At 800 K temperature the Li^+ ions mobility in the system $Li_{0.5-y}Na_yLa_{0.5}Nb_2O_6$ does not depend on stoichiometric factor y.

Author's contribution

1. The author of this dissertation has sintered ceramics; prepared the samples for X-ray diffraction, X-ray photoelectron spectroscopy measurements. He also assisted in some XRD and DTA measurements.
2. The preparation of samples for impedance spectroscopy measurements. All measurements of impedance spectroscopy with three different spectrometers and result analysis.
3. A part of the results were obtained in collaboration with scientists from other institutions. The synthesis of all pyrophosphates and some other materials was conducted in *Institute of Inorganic Chemistry, Riga Technical University* (Latvia). The synthesis of niobates was performed in *Vernadskii Institute of General and Inorganic Chemistry* (Kyiv, Ukraine). Some XRD, XPS, XRF and DTA/TGA/DSC measurements were performed in *Riga Technical University*, in *Department of Oxides and Frorides, Institute of Molecules and Materials in Le Mans* (France), in *Center for Hydrogen Energy Technologies, Lithuanian Energy Institute* (Kaunas, Lithuania), and in *Faculty of Physics, Warsaw University of Technology* (Warsaw, Poland).

Practical importance of the dissertation:

During the period of PhD studies new Li and Na ion solid electrolytes were synthesized and investigated. Pyrophosphates and niobates can be used as cathode materials or electrolytes in solid state batteries for various electrochemical devices, such as vehicles, phones, etc.

List of publications on the theme of the thesis (indexed by *ISI Web of Science*):

1. S. Daugėla, T. Šalkus, A. Kežionis, V. Venckutė, D. Valdniece, D. Dindune, M. Barre, A. F. Orliukas. *Anomalous temperature dependences of $Na_2MnP_2O_7$ electrical properties*. Solid State Ionics 302, 72-76 (2017).
2. S. Daugėla, A. Kežionis, T. Šalkus, A. F. Orliukas, A. G. Belous, O. I. V'yunov, S. D. Kobylianska, L.O. Vasylechko. *Peculiarities of ionic conduction in $Li_{0.5-y}Na_yLa_{0.5}Nb_2O_6$ system at high temperatures.* Solid State Ionics 300, 86-90 (2017).
3. A. F. Orliukas, V. Venckutė, S. Daugėla, A. Kežionis, A. Dindune, D. Valdniece, J. Ronis, M. Lelis, M. Mosiałek, T. Salkus. *Synthesis, structure and impedance spectroscopy of $NaCsZn_{0.5}Mn_{0.5}P_2O_7$ pyrophosphate ceramics*. Solid State Ionics 302, 92-97 (2017).
4. V. Venckutė, A. Dindune, D. Valdniece, A. Krumina, M. Lelis, V. Jasulaitienė, A. Maneikis, S. Daugėla, T. Šalkus, A. Kežionis. *Preparation, structure, surface and impedance analysis of $Na_2Zn_{0.5}Mn_{0.5}P_2O_7$ ceramics*. Lithuanian Journal of Physics 57(3), 183-193 (2017).

List of other publications (indexed by *ISI Web of Science*):

1. A. J. Janavičius, R. Purlys, A. Mekys, Ž. Norgėla, S. Daugėla, R. Rinkūnas. *Superdiffusion of carbon by vacancies irradiated with soft X-rays in Cz silicon*. Latvian Journal of Physics and Technical Sciences 5, 68-75 (2015).
2. T. Šalkus, E. Kazakevičius, J. Reklaitis, V. Venckutė, S. Daugėla, R. Davidonis, D. Baltrūnas, A. Dindune, D. Valdniece, A. F. Orliukas. *Study of the $Li_3Fe_{1.2}Sc_{0.75}Y_{0.05}(PO_4)_3$ ceramics by impedance and Mössbauer spectroscopy.* Solid State Ionics 302, 30-34 (2017).
3. M. Dudek, B. Lis, R. Lach, S. Daugėla, T. Šalkus, A. Kežionis, M. Mosiałek, R. P. Socha, J. Morgiel, M. Gajek, M. Sitarz, M. Ziąbka. *$Ba_{0.95}Ca_{0.05}Ce_{0.9}Y_{0.1}O_3$ as an electrolyte for proton conducting ceramic fuel cells.* Electrochimica Acta 304, 70-79 (2019).

List of the presentations in conferences:

1) A. J. Janavičius, R. Purlys, R. Rinkūnas, S. Daugėla. *Superdiffusion of carbon in silicon by vacancies irradiated with soft X-rays*. 17th International Conference-School Advanced Materials and Technologies 2015. 27-31 08 2015, Palanga, Lithuania (poster presentation).
2) S. Daugėla, T. Šalkus, A. Kežionis, V. Venckutė, D. Valdniece, A. Dindune, M. Barre, A. F. Orliukas. *Anomalous temperature*

dependences of $Na_2MnP_2O_7$ electrical properties. 12th International Symposium on Systems with fast Ionic Transport (ISSFIT-12) 3-7 07 2016, Kaunas (poster presentation).

3) S. Daugėla, T. Šalkus, A. Kežionis, D. Valdniece, A. Dindune, M. Barre, A.F. Orliukas. *Anomalous temperature dependence of $Na_2MnP_2O_7$ electrical properties*. 18th International Conference-School Advanced Materials and Technologies 2016. 27-31 08 2016, Palanga, Lithuania (poster presentation).
4) S. Daugėla, T. Šalkus, A. Kežionis, V. Venckutė, D. Valdniece, A. Dindune, M. Barre, A. F. Orliukas. *Electrical properties of $Na_2MnP_2O_7$ with regard to some other pyrophosphates*. 6th seminar - Properties of ferroelectric and superionic systems. 17-18 11 2016, Uzhgorod, Ukraine (oral presentation).
5) S. Daugela, T. Salkus, A. Kezionis, D. Valdniece, A. Dindune, M. Barre, A.F. Orliukas. *Anomalous Temperature Dependences of $Na_2MnP_2O_7$ Electrical Properties. Broadband Impedance Study of Memristor Oxide Films (project seminar).* 08 07 2016, Vilnius (oral presentation).
6) S. Daugela, V. Venckute, A. Dindune, D. Valdniece, A. Krumina, M. Lelis, V. Jasulaitiene, A. Maneikis, T. Salkus, A. Kezionis, A. F. Orliukas. *Preparation, Structure, Surface and Impedance Spectroscopy of $Na_2Zn_{0.5}Mn_{0.5}P_2O_5$ Ceramics*. 19th International Conference-School Advanced Materials and Technologies 2017. 27-31 08 2017, Palanga, Lithuania (poster presentation).
7) S. Daugėla, A. Kežionis, T. Šalkus, B. Lis, M. Dudek. *$Ca_{0.05}Ba_{0.95}Ce_{0.9}Y_{0.1}0_3$ ir $BaCe_{0.9}Y_{0.1}0_3$ keramikų impedanso spektroskopijos tyrimai*. 42th Lithuanian National Conference of Physics. 4-6 10 2017, Vilnius (poster presentation).
8) S. Daugela, A. Kezionis, T. Salkus, B. Lis, M. Dudek. *Impedance Spectroscopy Investigation of $Ca_{0.05}Ba_{0.95}Ce_{0.9}Y_{0.1}0_3$ and $BaCe_{0.9}Y_{0.1}0_3$ Ceramics*. New Multiferoics and Superionic Conductors for Acoustoelectronics and Solid State Ionics (project seminar). 10 10 2017, Vilnius (oral presentation).
9) S. Daugėla, T. Šalkus, A. Dindune, D. Valdniece, M. Barre, A. Kežionis. *Temperature Dependences of $Na_xLi_{2-x}MnP_2O_7$ Electrical properties*. 13th International Symposium on Systems with fast Ionic Transport (ISSFIT-13) 3-7 07 2018, Minsk, Belarus (poster presentation).

10) A. F. Orliukas, S. Daugėla, V. Kavaliukė, A. Dindune, D. Valdniece, M. Lelis, V. Jasulaitienė, A. Maneikis, T. Šalkus, A. Kežionis. *Peculiarities of electrical properties of some pyrophosphates as proposed electrode materials for Li and Na – ion secondary batteries*. 13th International Symposium on Systems with fast Ionic Transport (ISSFIT-13) 3-7 07 2018, Minsk, Belarus (poster presentation).
11) S. Kazlauskas, E. Kazakevičius, A. Žalga, S. Daugėla, A. Kežionis. *Electrical Properties of Gadolinium Doped Ceria Ceramics*. 13th International Symposium on Systems with fast Ionic Transport (ISSFIT-13) 3-7 07 2018, Minsk, Belarus (poster presentation).

Layout of the thesis

This thesis consists of seven chapters, but not all of them are numbered in contents. The first named "Abbreviations" lists all the shortenings used in this thesis. The second is "Introduction", which includes the aim, main tasks, scientific novelty of the work, statements presented for the defence, practical importance, author's contribution to publications used in the thesis, and the lists of both publications and conferences during the period of PhD studies. The third chapter is an "Overview" of literature in topics of the PhD thesis research. The fourth is "Experimental" which is devoted for describing of methods and measurement techniques used in this work. The fifth chapter is named "Results and discussions" and consists of two sections in order to represent the results of two types of different materials – pyrophosphates and niobates – investigated and discussed. The sixth chapter is "Conclusions" which briefly summarizes the results reported in previous chapter. The last chapter is named "References" which is for listing of all publications and other bibliography used for preparation of this thesis and mentioned or cited in it.

1. OVERVIEW

1.1 Appliance of solid electrolytes for lithium and sodium ion batteries

Conventional Li-ion batteries usually consist of a liquid electrolyte [1], which capacitates to transfer Li ions from cathode to anode and vice versa. Liquid electrolyte has a very good property that it is highly conductive at low or ambient temperatures, but in spite of that several disadvantages are present: battery degradation due to continuous charging and discharging cycles, flammability, dissolution and leakage of the electrolyte, also the formation of dendrites of Li, which increases the risk of explosion, is the severe problem inherent in the liquid electrolyte battery [2-4]. In order to overcome these problems a solid electrolyte can be used instead of liquid one. Solid electrolyte is the basic attribute of a solid state battery despite of cathodic and anodic materials used in the battery. The great advantage of the solid state battery is the tenuous self-discharge rate (up to several percents per year), more uniform output voltage and increased charge/discharge cycles (>1000 cycles to 80% of rated capacity at 50% discharge), resistance to shock and vibrations [5, 6]. The use of ASSBs in commercial applications is limited by high costs due to long time and high temperatures required for synthesis, and also expensive materials (Ge, Ti, La, Y, Sc, In) needed [7].

Solid State battery is analogical to a liquid electrolyte battery except of the phase state of the electrolyte. The battery consists of anode, cathode and the solid electrolyte (see Fig. 1.1). The anode is attached to copper foil due to better electrical conductivity of the battery. The cathode in turn is attached to aluminum foil [8]. When the battery is charging, there is movement of the ions from cathode (e.g. $LiCoO_2$) crystal toward the electrolyte interface and the ions occupy their places in the anode (e.g. Li_xC_6). When the battery is discharging, the reverse process takes place and Li^+ ions travel via the solid electrolyte towards the $LiCoO_2$ cathode [2, 8].

Sodium solid state batteries are slightly less effective than lithium ones [9, 10], but nevertheless are much cheaper because of wide spread whereas lithium metal is not only much more expensive, but also its reserves are in politically sensitive areas [11-13].

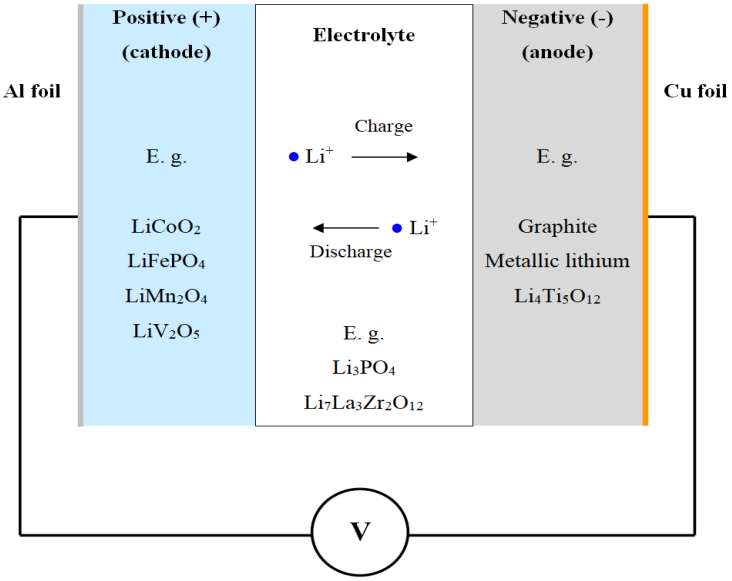

Fig. 1.1. A schematic representation of lithium based all solid state battery (ASSB), showing some of possible cathode, anode and electrolyte materials.

1.1.1 Appliance for cathode

The cathode of the solid state battery must be structurally stable during lithiation and delithiation processes, must have superior energy density and good cyclical capacity. Lithium metal oxides are widely used cathode materials for lithium based solid state batteries. The most popular cathode material is lithium cobalt oxide (LCO) [14-19] and it's stoichiometric structure is $LiCoO_2$. LCO exhibits relatively high specific energy of about 150 mAh g^{-1} [2, 20] and octahedral arrangement with a lithium atoms' layer between oxygen and cobalt [2, 21]. Also it is worth to note that actually $LiCoO_2$ conductivity is superior to those of its rivals $LiMnO_4$ and $LiFePO_4$ [22], but on the other hand $LiCoO_2$ shows larger difference between charge and discharge rates [23, 24] compared to $LiMnO_4$ and $LiFePO_4$ [25-27].

Lithium manganese oxide is another material suitable for the cathodes of solid state batteries. $LiMn_2O_4$ compound has very low resistance to the passage of lithium ions during charging and discharging processes because of its spinel based structure [28-30]. $LiMn_2O_4$ has some unwanted properties too: lower capacity than LCO and notable phase change during processes of ions transport [2].

Another cathode material is lithium based phosphate $LiFePO_4$. It is known to be less hazardous and less expensive to produce compared to other

lithium based oxide materials. The theoretical capacity of $LiFePO_4$ is reported to be 170 mAh/g [31]. Furthermore, $LiFePO_4$ has an olivine based structure which increases the transfer of ions and consequently decreases the resistance to the path of ion transfer [20, 28, 32, 33]. But in spite of that phosphorus in $LiFePO_4$ has a high self-discharge rate, which causes the undesirable degradation of this material [2]. Another drawback is relatively low electrical conductivity (about $10^{-9} – 10^{-10}$ S/cm) [31].

Metal chalcogenides TiS_2 and V_2O_5 are also known as good cathode materials [34, 35]. V_2O_5 has comparably high theoretical capacity of 294 mAh/g [35].

Actually, the overall performance is solid state batteries is mostly limited by the cathode materials because of their specific capacity which is known to be lower [2, 36], but anyway thin film Li-ion batteries can overcome these problems allowing to achieve more than 200 Wh/kg energy density [37].

1.1.2 Appliance for anode

Anode is the part of a solid state battery which stores Li/Li^+ atoms within it. Great capacity and sufficient difference in the electrochemical potential vs. cathode are required for good anodic material [38, 39]. One option is pure lithium metal. It has very good discharge capacity up to 700 mAg g^{-1} [40] and very adequate capacity retention. However pure lithium anodes have some disadvantages. Firstly, pure lithium metal is not suitable for using at elevated temperature conditions [41]. The other problem is a discernible increase in self-heating of Li anodes when the number of cells of operation rises. It is related to the changes of the surface area when the lithiation process takes place [2, 42]. Also in the case of pure metallic lithium anode the formation of Li dendrites takes place. This phenomenon causes non-uniform current density across the cell, which leads to hazardous temperature gradient throughout the cell [2, 43, 44].

Another suitable material for solid state anode is lithium titanium oxide (LTO) of a stoichiometric form $Li_4Ti_5O_{12}$. LTO has octahedral structure which is very helpful for integrating lithium ions within it when operating the battery [43, 45, 46]. Also, LTO is almost free of structural changes during lithiation and delithiation processes and is pretty stable [2, 47]. The drawback of $Li_4Ti_5O_{12}$ anode is that it has the specific energy of 175 mAh g^{-1} [48, 49], which is not sufficient in some cases [2]. Wilkening et al. reported [50] that the electrical conductivity value of $Li_4Ti_5O_{12}$ was $1.3 \cdot 10^{-5}$ S/m at 433 K temperature with the activation energy of 0.94 eV. Similar mediocre

conductivity values of $Li_4Ti_5O_{12}$ were recently confirmed by Schichtel et al [51].

The most common material for anode of solid state batteries is carbon and carbon based materials [52-57]. Graphite is widely used anode material in solid state batteries [58-63] and especially in commercial applications [6, 64]. It is attractive material because of its price, processing technologies and the ability to suffer large number of charging and discharging cycles. Since the interlayer forces (van der Walls ones) are negligible and the gap between layers is broad (3.35 Å) [65] the layered structure of graphite is advantageous for the lithium incorporation in it [66-69] with the highly anisotropic conduction properties [70]. Graphitic carbon is commonly used as the anode in commercial lithium and sodium batteries because of its higher specific charge, more negative redox potential than most metal oxides or polymers, better cycling performance than pure lithium alloy and less volumetric expansion in the lithiation process [2, 71].

Pure silicon and carbon/silicon anodes [72-76] have also been investigated. Carbon added into silicon can reduce the undesirable volume expansion attributed to silicon anode during lithiation [77]. Wang et al. demonstrated that after 20 charge/discharge cycles the $C_{0.8}Si_{0.2}$ reversible capacity was 794 mAh g^{-1} [78]. Chan et al. showed another way to reduce the volume expansion of silicon when used as anode material. They used silicon nanowires as lithium battery anodes and reported about less stress of anode during battery operation. This particularity is related to the amorphous state of silicon nanowires [79].

Recently germanium was proposed as promising anode material with a very high theoretical capacity of 1625 mAh/g for $Li_{22}Ge_5$ [80]. Laforge et al. [81] achieved the maximum stable Ge anode capacity of 1460 mAh/g. Chockla et al. [82] prepared Ge nanowires by solution-grown method and demonstrated the stable battery cycling of 1248 mAh/g after 100 cycles and above 600 after 1200 cycles.

1.2.3 Appliance for electrolyte

Solid electrolytes have these requirements: high ionic conductivity (preferably at room temperature (RT)) and negligible electronic conductivity; good thermal stability matching thermal expansion coefficients with both electrodes; decent chemical stability (especially with elemental Li or Li-alloy negative anodes) and high electrochemical decomposition voltage (desirable >5 V); environmental benignity and low cost. The

adequate number of mobile ions is required for fluent conductivity. Also the sufficient quantity of vacancies in the lattice is required for smooth transferring of the ions, and the activation energy of charge carriers must be low [2, 83]. Solid state electrolytes can be classified into two types: bulk electrolytes and thin electrolytes. The thickness of bulk electrolytes varies in the range of several hundred micrometers while the thickness of the thin electrolytes is only up to several microns. Thin film electrolytes require more advanced methods to fabricate them, for example pulsed laser deposition, chemical vapour deposition, radio frequency (RF) sputtering etc., while bulk solid state electrolytes are usually produced by mechanical milling, pressing and sintering [2, 84].

Most widely used solid state electrolytes are solid polymeric electrolytes (SPE) [85]. SPEs are advantageous because of their high conductivity similar to the one of liquid electrolytes. SPEs are commonly used with added inorganic salt. Those complex materials are more stable than pure polymer. That stability is due to low lattice energy. Frequently used complexes are PEO-$LiCF_3SO_3$ and PEO-$LiBF_4$ [2, 85].

NASICON (Na Super Ionic conductors) type electrolytes of general form $LiM_2(PO_4)_3$ are also investigated as possible electrolyte material [86, 87]. The primary factors that restrict the use of NASICON structure electrolytes are grain boundary effects, which behave as the scattering sites for ion transportation reducing the total ionic conductivity to 10^{-5} S/cm [86, 88].

Also the crystals with the garnet structure having general formula $X_3Z_2(TO_4)_3$ (X = Ca, Fe, etc., Z = Al, Cr, etc., T = Si, As, V, Fe, Al) are investigated and used materials as solid state electrolytes [89, 90]. The highest ionic conductivity and low activation energy in garnet-related structures has been reported to be approximately 4×10^{-4} S/cm at room temperature for the cubic $Li_7La_3Zr_2O_{12}$ (LLZO) [89].

There are several less popular material types investigated as bulk electrolyte materials. It is polymer gel electrolyte, vanadium-based electrolytes and polymer solid state electrolytes based on Polyethylene glycol (PEG) coupled with organic hybrids and plasticizers [2]. We will not discuss them in detail.

The thin film solid state electrolytes require very precise techniques. LiPON (lithium-phosphorus-oxy-nitride) is the most commonly used thin film solid state electrolyte [91, 92]. The lithium phosphorus oxy-nitride electrolyte is deposited by RF magnetron sputtering from a ceramic target of Li_3PO_4 using a nitrogen process gas to form the plasma. The films are

amorphous and free of any columnar microstructure or boundaries. LiPON is also very stable at elevated temperatures and in contact with metallic lithium. Electronic resistivity of LiPON is greater than 10^{14} Ω·cm. The self-discharge rates of most thin film batteries including LiPON electrolyte are negligible [92].

1.2 Crystal structures of solid electrolytes and their ionic conductivities

1.2.1 NASICON structure electrolytes

NASICON is an acronym of sodium (Na) Super Ionic Conductor which usually denotes a family of solid electrolytes with the same crystallographic structure. For Na^+ ion migration the compound was optimized to have chemical formula $Na_{1+x}Zr_2Si_xP_{3-x}O_{12}$ ($0 < x < 3$). In a broader sense that acronym is also used for analogous compounds where Na, Zr and (or) Si are replaced by big number of isovalent elements [93, 94]. NASICON electrolytes have high ionic conductivities in the order of 10^{-3} S/cm which is comparable to those of liquid electrolytes. The conduction pathway is caused by hopping of mobile Na ions amongst interstitial sites of the NASICON crystal lattice [95].

The crystal structure of NASICON was characterized by Hagmann and Kierkegaard in 1968 describing the structure of three isovalent compounds: $NaZr_2(PO_4)_3$, $NaTi_2(PO_4)_3$ and $NaGe_2(PO_4)_3$ [96]. The most common NASICON composition $Na_3Zr_2Si_2PO_{12}$ crystal is built up of corner-sharing PO_4-SiO_4 tetrahedra and ZrO_6 octahedra which are linked by corners and form 3D interconnected channels of the covalent network and two types of interstitial positions (M′ and M″) where mobile cations are distributed. The Zr, Ti or Ge ions are octahedrally surrounded by oxygen ones [86, 96, 97]. The space group of $Na_3Zr_2Si_2PO_{12}$ is denoted to be $R\bar{3}/c$ [96] and it is very common one for NASICONs. Keeping in mind the general NASICON structure $Na_{1+x}Zr_2Si_xP_{3-x}O_{12}$ it is known that sodium ions are located at two types of interstitial positions. The mobile cations move from one site to another through bottlenecks, whose size, and thus the NASICON electrical conductivity, depends on the nature of the skeleton ions and on the carrier concentration, on the site occupancy [86, 98] and also on the gas nature and concentration in the surrounding atmosphere. There does not seem to be conspicuous difference between the conductivities in air and inert gas. The

surrounding oxygen partial pressure independence of ionic conductivity of an oxide is an evidence of a pure ionic conductivity and consequently indicates that the electronic conductivity is low [99].

Furthermore, the conductivities of compositions containing less sodium (e.g. $Na_{2.8}Zr_{2-x}Si_{1.8-4x}P_{1.2+4x}O_{12}$) are lower than those of $Na_3Zr_2Si_2PO_{12}$. The lattice parameter is increased when the sodium part increases in the compound and thus the barrier to Na^+ ions transference is decreased causing higher conductivity [100]. Also it was shown by several groups that reducing the zirconium content in a composite causes lower conductivity [101, 102]. These results are manifest illustration that the control of the stoichiometry is substantial in order to obtain the optimal conductivity.

The conductivity of $Na_{1+x}Zr_2Si_xP_{3-x}O_{12}$ decreases for $x<2$ or when all Si atoms are substituted by P in the crystal lattice (and vice versa). The conductivity can be increased by adding rear earth elements to NASICON, such as yttrium [99]. Yttrium, either added directly as a dopant or indirectly using additions of tetragonal polycrystalline zirconia (TZP) containing 3% Y_2O_3, is well known in increasing the conductivity of NASICON [99].

NASICON materials can be prepared as single crystals, polycrystalline ceramic, thin films or as a bulk glass which is known as NASIGLAS. Most of them react with molten sodium at 300 °C and therefore are unsuitable for batteries containing sodium in an electrode [95], but are suitable in a sodium sulphur battery where the sodium stays solid [103, 104]. So the main application envisaged for NASICON materials is as the solid electrolyte in all solid state sodium ion battery.

The materials of the same structure but containing lithium instead of sodium are also named as NASICON. For example, one well known typical example is $LiZr(PO_4)_3$ [105-107]. American group of Subramanian at al. [108] prepared a remarkable investigation about $LiB(IV)_2(PO_4)_3$ (B = Ti, Zr or Hf). The good suitability of Ti in pair with Sc for that system in terms of conductivity was reported with the highest conducive value of $8.8 \cdot 10^{-4}$ S/cm for $Li_{1.8}(Sc_{0.8}Ti_{1.2})(PO_4)_3$ at room temperature. Russian group of Bykov et al. [109] prepared a comprehensive study about $Li_3M_2(PO_4)_3$ (M = Fe, Sc, Cr). Aono et al. [110] prepared $LiGe_2(PO_4)_3$, $LiTi_2(PO_4)_3$ and $LiHf_2(PO_4)_3$, Orliukas et al. [111] prepared $Li_3Ti_{1.5}(PO_4)_3$. It was found that $LiTi_2(PO_4)_3$ has high ionic conductivity, but still not sufficient. The enhanced ionic conductivity was achieved after partially replacing M^{4+} ions by trivalent Al^{3+} and Fe^{3+}. That substitution of Ti^{4+} in $LiTi_2(PO_4)_3$ by M^{3+} and M^{2+} was

analyzed in detail by Aono group [112-114], Orliukas group [115-121] and other ones [122-125]. The conductivities were found to be adequate especially with the substitution by In with the conductivity value of $1.9 \cdot 10^{-4}$ S/cm at room temperature [122]. The effects of increasing Li-ion conductivity, lowering porosity and formation of the second glassy phases at grain boundaries were investigated in point of fractional changes. The highest ionic conductivity value of $7 \cdot 10^{-4}$ S/cm was achieved for $Li_{1.3}M_{0.3}Ti_{1.7}(PO_4)_3$ (M = Al, Sc) at 25 °C, but $Li_{1+x}Al_xGe_{2-x}(PO_4)_3$ and $Li_{1+x}Fe_xHf_{2-x}(PO_4)_3$ were found to be more stable. Aono et al. [126] also demonstrated that denser NASICON electrolytes can be obtained by adding Li_3PO_4 and Li_3BO_3 to $LiTi_2(PO_4)_3$ because of better contact between grains and lower porosity.

Fu [127] prepared fast Li-ion conducting glass-ceramics from the $2[Li_{1+x}Ti_2Si_xP_{3-x}O_{12}]$-$AlPO_4$ system by melt-quench method. The major phase was based on $LiTi_2P_3O_{12}$ in which Ti^{4+} and P^{5+} ions were partially replaced by Al^{3+} and Si^{4+}, respectively. Increasing x (up to x = 0.4 when substitutions reaches saturation) resulted in a considerable enhancement in conductivity, with the maximum conductivity value of $1.5 \cdot 10^{-3}$ S/cm at 25 °C temperature, which is adequate for ASSBs applications.

There are two exceptional groups of NASICON on which many efforts and attempts were made. These two groups are LATP and LAGP: $Li_{1+x}Al_xTi_{2-x}(PO_4)_3$ and $Li_{1+x}Al_xGe_{2-x}(PO_4)_3$, respectively [128].

The perspective $Li_{1+x}Al_xTi_{2-x}(PO_4)_3$ was analyzed by partial VO_4 substituting for PO_4 within the framework [129], using different fractions of Li, Al and Ti atoms and different preparation technique [130-138]. The highest ionic conductivity achieved (by citric acid assisted sol-gel method) was of $6.13 \cdot 10^{-4}$ S/cm with the activation energy of 0.29 eV at 25 °C temperature for crystallized glass-ceramics of $Li_{1.4}Al_{0.4}Ti_{1.6}(PO_4)_3$ [136]. The voltages (vs. Li/Li^+) corresponding to the redox peaks for $Li_{1+x}Al_xTi_{2-x}(PO_4)_3$ electrolytes are usually beyond 2.4 V [132]. The high value of conductivity, good chemical stability properties, relatively easy fabrication suggest it as a promising material for solid electrolytes in ASSBs. Wu et al. [139] prepared LATP type thin film solid state Li-ion battery $LiMn_2O_4/Li_{1.3}Al_{0.3}Ti_{1.7}(PO_4)_3/LiMn_2O_4$ by spray technique. The ionic conductivity of LATP sintered pellet was of $3.46 \cdot 10^{-4}$ S/cm. It was found that the battery can be cycled with a 0.21% capacity loss per cycle when 50 cycles were performed. A. Dindune et al. [140] reported that partial substitution of Al by Y in the LATP system can cause the changes of the

interplanar distances into ceramics and increase the conductivity of grain boundaries by several times simultaneously decreasing the activation energy for mobile lithium ions. The group of Orliukas also investigated the partial substituting of Al_xTi_x in the LATP system by Zr, Ge , Sc and Y [141-146]. The values of the activation energy related to the grain conductivity and relaxation frequency in this type of materials were found to be very close. That was attributed to the fact that the temperature dependence of the grain conductivity is caused only by Li^+ ions mobility, while a number of charge carriers remains temperature independent [141, 143].

Another very perspective group of NASICON electrolytes is $Li_{1+x}Al_xGe_{2-x}(PO_4)_3$ (LAGP) electrolyte. The electrolytes of this group showed very good electrical properties once started to investigate [147-150]. LAGP glass-ceramics prepared by melt-quench method and recrystallization showed the ionic conductivity value of $4.0 \cdot 10^{-4}$ S/cm at 25 °C temperature for $Li_{1.5}Al_{0.5}Ge_{1.5}(PO_4)_3$ [151]. The same material with excess of Li_2O enhanced the conductivity up to $7.25 \cdot 10^{-4}$ S/cm at the same temperature [152]. The Li_2O excess acts twofold: first by self-incorporating into the crystal lattice and the second being as a secondary phase and acting like a nucleating agent to distinctly boost the crystallization of the glasses during heating process, thus leading to an improved interconnection between the grains and hence to a denser microstructure with a unvaried grain size. The microscopic characteristics of the Li-cation motion in LAGP superionic conductors are deduced via a hopping mechanism [153, 154]. The $Li_{1.5}Al_{0.5}Ge_{1.5}(PO_4)_3$–$0.05Li_2O$ demonstrated the excellent electrochemical stability and was stable up to 6 V vs. Li/Li^+ [152]. Soon Thokchom et al. [155] prepared new glass-ceramics (sintering temperature 850 °C) based on $Li_{1.5}Al_{0.5}Ge_{1.5}(PO_4)_3$ superionic conductor and reported even higher ionic conductivity of $5.1 \cdot 10^{-3}$ S/cm at 27°C. Also some investigations were done by doping of Ge not only by Al, but also by Ti [156], Cr [147, 157] and both by Al and Cr [158]. The $Li_{1+x}Cr_xGe_{2-x}(PO_4)_3$ was found to be less conductive than $Li_{1+x}Al_xGe_{2-x}(PO_4)_3$ [147]. Substitution of Ge^{4+} by Al^{3+} and Cr^{3+} induced more Li^+ ions in vacant sites and also increased the unit cell parameters and enhanced the ionic conductivity of the glass–ceramics. The highest Li-ion conductivity of $6.65 \cdot 10^{-3}$ S/cm at 26°C was obtained for $Li_{1.5}Al_{0.4}Cr_{0.1}Ge_{1.5}(PO_4)_3$ composition with low activation energy of 0.29 eV and electrochemical stability up to 7 V vs. Li/Li^+ [158]. The excellent electrochemical stability of LAPG is oftentimes emphasized [159].

Recently the cold sintering process (CSP) was introduced for processing of LAPG superionic ceramics [160, 161]. This method significantly reduces the formation temperature and duration of the synthesis of a solid electrolyte. This method requires a liquid phase precursor based on the water-soluble Ge^{4+} oxalate complex. The solid electrolyte without the formation of intermediate compounds is determined by chemical interactions in a liquid phase precursor containing multicomponent solution [160].

The only one drawback of LAGP type NASICONs is a price of GeO_2 (one of precursors) [162], but the electrical and electrochemical properties of LAGP are very attractive for applications in ASSBs.

1.2.2 Garnet structure electrolytes

Lithium containing garnets were described in 1968 for the first time [163]. Nowadays garnet structure electrolytes are essential candidates as solid state electrolytes for ASSB. Garnets have typical structure $A_3B_2X_3O_{12}$ with XO_4 tetrahedra and BO_6 octahedra connected via edge sharing [164, 165] and typically crystallize in a face centered cubic structure (s. g. $Ia\bar{3}d$) [166]. Garnets have several generations depending on number of the Li atoms in a crystal structure [167]. They are Li_3-phases $Li_3Ln_3Te_2O_{12}$ (Ln = Y, Pr, Nd, Sm-Lu) and $Li_{3+x}Nd_3Te_{2-x}Sb_xO_{12}$ (x = 0.05-1.5); Li_5-phases $Li_5La_3M_2O_{12}$ (M = Nb, Ta, Sb); Li_6-phases $Li_6ALa_2M_2O_{12}$ (A = Mg, Ca, Sr, Ba; M = Nb, Ta) and Li_7-phases $Li_7La_3M_2O_{12}$ (M = Zr, Sn). The very high ionic conductivity measured in electrolytes of garnet structure has been reported to be $4\cdot10^{-4}$ S/cm at 25 °C for the cubic $Li_7La_3Zr_2O_{12}$ (LLZO) [89]. It is surprising that grain boundary resistance was found to be less than 50% of total resistance, so it means that total ionic conductivity is in the same magnitude as bulk ionic one and thus resulting in high total ionic conductivity [168].

Geiger et al. [169] discovered that a phase transition from tetragonal to cubic system takes place at 100-150 °C in $Li_7La_3Zr_2O_{12}$, and the cubic phase was found to be more conductive. Cubic $Li_7La_3Zr_2O_{12}$ can be stabilized at room temperature relatively to its slightly less conducting tetragonal phase via small amount of Al^{3+} [169]. Otha et al. partially doped Nb^{5+} on Zr^{4+} sites obtaining $Li_{6,75}La_3(Zr_{1.75}Nb_{0.25})O_{12}$ and reported ionic conductivity to be $8\cdot10^{-4}$ S/cm at 25 °C and wide electrochemical stability window 0-9 V vs Li/Li^+ [168, 170]. Li et al. prepared $Li_{7-x}La_3Zr_{2-x}Ta_xO_{12}$ ($0<x<1$) by conventional solid state reaction method in alumina crucible and found that $Li_{6.4}La_3Zr_{1.4}Ta_{0.6}O_{12}$ has highest ionic conductivity of $1.0\cdot10^{-3}$ S/cm when x

= 0.6 with an activation energy of 0.35 eV at room temperature [171]. The highest achieved ionic conductivity in garnet structure electrolytes was reported by Buannic et al [172]. They prepared $Li_{6.65+y}Ga_{0.15}La_3Zr_{2-y}Sc_yO_{12}$ by dual substitution strategy. The Ga substitution is for stabilizing cubic crystal structure and the Sc substitution is for increasing Li ion number. $Li_{6.75}Ga_{0.15}La_3Zr_{1.90}Sc_{0.10}O_{12}$ (y = 0.10) showed ionic conductivity of $1.8 \cdot 10^{-3}$ S/cm at 27 °C [172].

The garnet structure Li-ion conductors are very promising for application in ASSBs. The main drawback is that it is not enough stable in the ambient atmosphere due to moisture and CO_2 [168, 173, 174]. Thus, the focus now is on increasing the stability of LLZO in the ambient atmosphere conditions.

1.2.3 Perovskite structure electrolytes

A number of compounds take perovskite name after the natural mineral $CaTiO_3$, which was first discovered in the Ural Mountains by Gustav Rose in 1839 and is named after Russian mineralogist L. A. Perovski [175]. Other natural perovskite structure compounds are loparite and silicate perovskite [175].

Perovskites have general chemical formula of ABO_3, where 'A' and 'B' are two cations of very different sizes, and O is an oxygen anion that bonds to both. The 'A' cations are larger than the 'B' ones. The ideal cubic structure has the B cation in 6-fold coordination, surrounded by an octahedron of anions, and the A cation in 12-fold cuboctahedral coordination. $MgSiO_3$ is good example of a true cubic perovskite. The relative ion size requirements for stability of the cubic structure are quite strict, so slight flexion and distortion can produce several lower symmetry distorted versions, in most cases orthorhombic and tetragonal ones [175].

The first perovskite-type solid electrolyte was $Li_{3x}La_{2/3-x}TiO_3$ (LLTO) prepared by Inaguma et al. [176] in 1993. Li^+ and La^{3+} ions occupy central A sites while Ti^{4+} ions occupy corner B sites. Oxygen ions form bottleneck causing potential barriers for Li-ion migration from one A site to an adjacent one [168]. The total ionic conductivity of $3\text{-}5 \cdot 10^{-4}$ S/cm at 300 K for $Li_{3x}La_{2/3-x}TiO_3$ was reported [177]. Similarly, it has been discovered that the polycrystalline lithium lanthanum titanate $Li_{0.34(1)}La_{0.51(1)}TiO_{2.94(2)}$ shows high ionic conductivity of more than $2 \cdot 10^{-5}$ S/cm at room temperature and bulk ionic conductivity of $1 \cdot 10^{-3}$ S/cm [168, 176]. Changing of lattice parameters influences size of the bottlenecks and therefore the conductivity, so many attempts tried to enlarge the lattice parameters of LLTO perovskites. The

conductivity of LLTO can be enhanced by the amorphous silicate layer introduced into grain boundary, thus enhancing the total ionic conductivity over $1 \cdot 10^{-4}$ S/cm at room temperature. The amorphous layer closely binds the grains, removes the anisotropy of exterior shells of grains and also supplements the lithium ions in various sites of grain boundary [178].

Li and La can be substituted by Sr in order to increase the lattice parameters of the perovskite structure and thus to enhance the ionic conductivity. But on the other hand doping by Sr also causes of Li-ion concentration. Inaguma et al. [179] doped 5 mol% Sr^{2+} of $Li_{1/2}La_{1/2}TiO_3$ and obtained higher ionic conductivity of the bulk part ($\sigma = 1.5 \cdot 10^{-3}$ S/cm^{-1} at 300 K) than the pure lanthanum lithium titanate. But anyway the difference of conductivities is not huge.

Inada et al. [168, 180] prepared $Li_{3/8}Sr_{7/16}Ta_{3/4}Zr_{1/4}O_3$ (LSTZ) (in which A and B cations of $SrZrO_3$ are partially substituted by Li and Ta) by "powder-bed sintering method", which is commonly used for preparation of dense garnet-structured lithium-ion conductor $Li_7La_3Zr_2O_{12}$ (LLZ). During the sintering process, the LSTZ pellet was covered with the same mother powder to suppress the excess Li loss during high temperature treatment and decrease the formation of secondary phases. For LSTZ sintered with covering LSTZ mother powder, secondary phases ($SrTa_2O_6$ and $Sr_2Ta_2O_7$) were significantly reduced and contact between LSTZ grains in the pellet was proper. The compound was found to be more stable against the lithiated negative electrode than LLTO and showed the total ionic conductivity value of $2.7 \cdot 10^{-4}$ S/cm at 27 °C [180]. Huang et al. [181] replaced Zr with Hf and prepared $Li_{3/8}Sr_{7/16}Hf_{1/4}Ta_{3/4}O_3$ (LSTH) by solid-state reaction. The achieved ionic conductivity ($3.8 \cdot 10^{-4}$ S/cm at 25 °C) was higher than LSTZ and electrochemical stability window was from 1.4 V to 4.5 V vs. Li/Li^+. It exhibits both high stability and small interfacial resistance with organic liquid electrolytes, which makes it very attractive candidate as a separator in Li-ion batteries [181].

1.2.4 Lisicon structure electrolytes

LISICON is an abbreviation of lithium super ionic conductor. This name was mentioned for the first time in 1978 by Hong et al. [182]. They investigated the structure and conductivity of $Li_{14}Zn(GeO_4)_4$ and reported the value of conductivity $1.25 \cdot 10^{-1}$ S/cm at 300 °C. By using the X-ray analysis (XRD) they found the rigid 3D network of $Li_{11}Zn(GeO_4)_4$ while the remaining Li^+ ions have occupancies at 4c and 4a interstitial positions where

each 4c position was found to be connected to two 4a positions. An average diameter of the bottleneck between these positions is larger than the double sum of the Li^+ and O^{2-} ionic radii, thus capacitating the fast Li^+ ion transport in the network [182]. In more detailed studies Mazumdar et al. [183] reported the $Li_{14}Zn(GeO_4)_4$ ionic conductivity of $1.3 \cdot 10^{-6}$ S/cm at 33 °C. However the latter value of conductivity was too low for ASSBs and other devices. Recently Song et al. [184] prepared LISICON structure solid electrolyte $Li_{10.42}Ge_{1.5}P_{1.5}Cl_{0.08}O_{11.92}$ (O^{2-} are partially doped with Cl^-) with ionic conductivity of $3.7 \cdot 10^{-5}$ S/m at 27 °C. This compound was stable with metallic lithium up to 9 V vs. Li/Li^+, which is one of the widest electrochemical windows of solid state electrolytes. Since ionic radius of Cl^- is larger than that of O^{2-}, partial substitution of O^{2-} by Cl^- increases the size of bottlenecks for Li-ion diffusion. Additionally Cl^- has smaller electro negativity than O^{2-} and accordingly the bonding between Li^+ and Cl^- is weaker than that between Li^+ and O^{2-} [168, 184]. These both effects enhance the ionic conductivity of the material, but the conductivity is still not high enough for ASSBs.

1.2.5 LIPON electrolytes

LIPON is an abbreviation of lithium phosphorus oxynitride and conversely from the electrolytes described above, LIPON is amorphous solid electrolyte. The conventional preparation technique is radio frequency magnetron sputtering with special target in a pure N_2 atmosphere. There are two types of targets: one is Li_3PO_4 and other is a mixture of Li_3PO_4 and Li_2O [168].

The first LIPON was synthesized by Bates at al. [185] using Li_3PO_4 as a target. The ionic conductivity of the obtained solid electrolyte, as they reported, was found to be $2 \cdot 10^{-6}$ S/cm at 25 °C. Also very good long-term stability in contact with lithium was reported. Recently higher values are achieved using the same target Li_3PO_4. Su et al. [186] reported the value of mean ionic conductivity $4.9 \cdot 10^{-6}$ S/cm at 22 °C. The prepared films on silica glass substrate showed the transmission of visible light higher than 80% what is good for applications in electrochromic devices. Van-Jodin et al. [187] prepared LIPON films by RF sputtering without magnetron (non-standard) and obtained the value of ionic conductivity of $6.7 \cdot 10^{-6}$ S/cm at 24 °C. It is the largest ionic conductivity value ever obtained for LIPONs. X-ray analysis revealed that the compound prepared by non-standard method has more phosphate groups (PO_4^{3-}, PO_3^{2-} and PO_2^- instead of a single PO_4^{3-}) than

in a way when magnetron is used. In the presence of more phosphate groups the structure becomes more disordered and thus the Li-ion mobility is enhanced. Metal-organic chemical vapor deposition (MOCVD) was also used to prepare LIPONs. Fujibayashi et al. [188] reported the value of ionic conductivity of $5.9 \cdot 10^{-6}$ S/cm when MOCVD is used for sample preparation. In their opinion, LIPON films prepared by MOCVD method are promising candidates to realize 3D structured micro batteries in the near future.

When the target is a mixture of Li_3PO_4 and Li_2O the conductivities are enhanced compared to these obtained using only Li_3PO_4 as a target. Suzuki et al. [189] used that target type with molar ratio of 1:2 and obtained the ionic conductivity of $6.4 \cdot 10^{-6}$ S/cm at 25 °C. That is three times of that conventional method when only Li_3PO_4 is used as a target. The enhancement is due to increased amount of Li-ion inside the electrolyte, but controversially the films formed from the target containing only Li_3PO_4 showed better durability in air. This is probably because the amount of Li in the film prepared from Li_3PO_4 target is much lower and consequently, the absorption of CO_2 in air was effectually suppressed [189].

LIPON solid electrolytes are promising for thin film ASSBs, but not for bulk ones because of relatively low ionic conductivities at low temperatures [190, 191].

1.2.6 Lithium-nitride electrolytes

Li_3N is the only one stable alkali metal nitride with a melting point above 800 °C [192]. It consists of hexagonal Li_2N layers which are linked by Li-ions forming Li-N-Li bridges [193]. Thus Li-ions can diffuse through 2D tunnels. The preparation of Li_3N is simple. A tape or thin tablet of pure lithium metal is exposed in a sustained flow of nitrogen gas and afterwards annealed [194]. Huggins et al. [195] prepared Li_3N electrolyte by reaction between pure lithium and nitrogen in a nitrogen atmosphere and annealing it at 750 °C in 1 atm of nitrogen and obtained ionic conductivity of $2.0 \cdot 10^{-4}$ S/cm at 25 °C. Rea et al. [196] prepared Li_3N electrolyte in the same way and annealed it at 800 °C. The obtained ionic conductivity was $4.0 \cdot 10^{-4}$ S/cm at 25 °C. Nevertheless the ionic conductivity is very adequate. Li_3N can react with cathode materials when potential exceeds 1.75 V vs. Li/Li^+.

Lithium nitride halides can be used instead of lithium nitrides to achieve better electrochemical stability while ionic conductivity remains similar to the one of Li_3N electrolyte. Hatake et al. [197] prepared quasi-binary isomorphous systems of $3Li_3N$-MI (M = Li, Na, K, Rb) solid electrolytes by

solid state reaction method between Li_3N and MI at 600 °C. The demonstrated ionic conductivity was in the range of $7.0 \cdot 10^{-5}$ S/cm to $1.1 \cdot 10^{-4}$ S/cm at RT and decomposition voltages 2.5-2.8 V. The grain boundary resistances were very small because of good sinterability. Even the ionic conductivity of powdered compounds was higher than 10^{-5} S/cm at RT. Therefore the ASSBs could be constructed by simply pressing. A cell of $C/3Li_3N$-KI/$LiTiS_2$ was made just simply pressing the powdered electrolyte and electrode materials, however the charge/discharge performance was not good enough because of a severe polarization in the positive electrodes [197]. Zhan et al. [198] prepared lithium borohydride-lithium nitride composite $LiBH_4$-Li_3N and obtained ionic conductivity of $1.1 \cdot 10^{-5}$ S/cm. Cyclic voltammetry (CV) showed that the voltage window of composite can attain 3 V, which is more stable than pristine Li_3N (< 1 V).

Lithium-nitride electrolytes show adequate ionic conductivity, but unfortunately the decomposition voltages are too low for high energy densities ASSBs [168].

1.2.7 Sulphide structure electrolytes

Sulphide structure electrolytes are similar to LISICON electrolyte γ-Li_3PO_4, but O^{2-} is replaced by S^{2-} [199]. Interaction between Li^+ and S^{2-} is weaker than that between Li^+ and O^{2-}. Therefore, the ionic conductivity of sulphide structure electrolytes is higher than of oxide type ones [200]. Sulphide structure solid electrolytes are classified into three types: glasses, glass-ceramics and ceramics [168].

All electrolytes of sulphide structure are very conductive. There are many examples of very good ionic conductivity of sulphides. In 2001, Kanno et al. [199] prepared $Li_{3.25}Ge_{0.25}P_{0.75}S_4$ and achieved the ionic conductivity of $2.17 \cdot 10^{-3}$ S/cm at 25 °C with electrochemical stability up to 5 V vs. Li/Li^+. A decade later Kamaya et al. [201] prepared solid electrolyte $Li_{10}GeP_2S_{12}$ with even higher ionic conductivity of $1.2 \cdot 10^{-2}$ S/cm at 27 °C and electrochemical stability up to 5 V vs. Li/Li^+. The impressive ionic conductivity of $Li_{10}GeP_2S_{12}$ is higher than that of other solid electrolytes and comparable to those of organic liquid electrolytes [168]. In 2016, Kato et al. [202] prepared $Li_{9.54}Si_{1.74}P_{1.44}S_{11.7}Cl_{0.3}$ with ionic conductivity of $2.5 \cdot 10^{-2}$ S/cm at room temperature, what is probably the highest value still reported among the solid electrolytes. Seino et al. [203] synthesized another very conductive material Li_2S-P_2S_5. That is the glass-ceramic with almost no grain boundaries in microstructure. The extremely high ionic conductivity was

achieved of about $1.7 \cdot 10^{-2}$ S/cm at 25 °C. In comparison, cold-pressed glass-ceramic showed distinct grain boundaries and the ionic conductivity was one magnitude lower. Similarly, Chu et al. [204] prepared $Li_7P_3S_{11}$ glass-ceramic by spark-plasma sintering (SPS) and achieved the ionic conductivity of about $1.2 \cdot 10^{-2}$ S/cm at 27 °C. It was also one magnitude higher than that of cold pressed electrolyte at the same temperature.

Despite the very high ionic conductivities of sulphide structure electrolytes (similar to organic liquid ones), they were not stable in the ambient atmosphere because of interaction with moisture [168, 205]. In order to apply that in ASSBs, it is required to find very adequate chemical composition and to ensure excellent preservation from the ambient atmosphere.

1.2.8 Argyrodite structure electrolytes

Argyrodites form a class of chalcogenide structures related to the mineral Ag_8GeS_6, which includes various fast Ag^+, Cu^+ or Li^+ ion conductors such as A_7PS_5X ($A = Ag^+$, Cu^+, Li^+) while X are halogens ($X = Cl$, Br, I) [206]. Argyrodite structure electrolytes are usually prepared by mechanical milling followed by annealing of the samples [206, 207].

Argyrodites containing lithium were firstly synthesized by Deiseroth et al. [208] in 2008. The highest conductivity value of argyrodites containing halogen elements (Cl, Br, I) was in the range of 10^{-3}-10^{-2} S/cm for Li_6PS_5Br electrolyte [209]. Rayavarapu et al. [210] explained that besides the disordered lithium distribution in an electrolyte, it is the disorder in the S^{2-}/Cl^- (or S^{2-}/Br^-) distribution that could promote ion mobility, whereas the big size I^- cannot be exchanged for S^{2-} and the resulting more ordered Li_6PS_5I exhibits much less conductivity. The highest conductivity value of argyrodites is reported by Rao et al. [206]. It is $6.8 \cdot 10^{-3}$ S/cm at RT for Li_6PS_5Br electrolyte. It is more than three times greater value than that for chlorine containing Li_6PS_5Cl ($1.9 \cdot 10^{-3}$ S/cm at RT) and four orders greater value than iodine containing Li_6PS_5I ($4.7 \cdot 10^{-7}$ S/cm at RT). The latter two values also are reported by Rao et al. [206]. Li_6PS_5X has good electrochemical stability – up to 7 V vs. Li/Li^+ for all halogens Cl, Br and I [168, 211].

Chen et al. [212] made ASSB Cu-Li_2S/Li_6PS_5Br/In with argyrodite structure electrolyte Li_6PS_5Br. The battery showed high initial charge and discharge capacities (500 mAh/g and 445 mAh/g, respectively), but fast

battery degradation occurred due to fast volume changes of the cathode material and Li^+/Cu^+ mobile ion effect.

Argyrodite structure batteries are very attractive for ASSBs because of their good ionic conductivity, but, similar with sulphide type solid electrolytes, argyrodites are sensitive to air.

1.2.9 Anti perovskite structure electrolytes

Since perovskite structure electrolytes have the structure $A^+B^{2+}X_3^-$, anti perovskites are "electronically inverted", thus based on system $A^-B^{2-}X_3^+$. Here A denotes halogen atom (F, Cl, Br, I) or a mixture of halogens, B denotes oxygen atom and X denotes lithium [213]. Typical antiperovskite structure electrolytes are Li_3OCl, Li_3OBr, while $Li_3OCl_{0.5}Br_{0.5}$ is a compound containing a mixture of halogens and has higher ionic conductivity ($1.94 \cdot 10^{-3}$ S/cm) than two previously mentioned electrolytes with single halogen. However, antiperovskites have significant drawback, it is they are very hygroscopic and an inert atmosphere is required for operating [168].

Braga et al. [214] performed experiments where lithium was partially changed by higher valent metal cation Mg^{2+}, Ca^{2+} and Ba^{2+}. The prepared glass type electrolytes $Li_{3-2x}Ba_xClO$ evolve from an antiperovskite structure and has extremely high ionic conductivity of $2.5 \cdot 10^{-2}$ S/cm for x = 0.005 at 25 °C. According to Braga et al. [214] "these glassy electrolytes for lithium batteries are inexpensive, light, recyclable, non-flammable and non-toxic. Moreover, they present a wide electrochemical window (higher than 8 V) and thermal stability within the application range of temperatures".

1.2.10 Summary

In Table 1.1 the very short summary of electrolyte properties is listed. Although the pyrophosphates in this thesis are characterized in a separate section (due to relevance for this dissertation) than electrolytes of other types, here in the table all structures of electrolytes are listed in the same level without any subdivision or prioritizing.

Table 1.1. Summary of advantages and drawbacks of solid electrolytes (according to [2, 15, 168]).

Electrolyte structure	**Advantages**	**Drawbacks**
NASICON	High ionic conductivities. Good chemical and	Pretty high costs of some precursors.

	electrochemical stability.	
Garnet	High ionic conductivities. Stable with lithium.	Not stable in the ambient atmosphere.
Perovskite	Pretty good ionic conductivities.	Harsh preparation conditions.
LISICON	Good chemical and electrochemical stability.	Only moderate ionic conductivities.
LIPON	Good chemical and electrochemical stability.	Low ionic conductivities.
Li-nitride	Pretty good ionic conductivities.	Too low decomposition voltages.
Sulfide	Very high ionic conductivities.	Not stable in the ambient atmosphere. Immature deposition technologies.
Argyrodite	High ionic conductivities.	Not stable in the ambient atmosphere.
Anti-perovskite	High ionic conductivities.	Very hygroscopic.
Pyrophosphates	Good chemical and electrochemical stability. Easy and cheap synthesis.	Only moderate ionic conductivities. Pretty hygroscopic.

1.3 Pyrophospates

The importance and progress of developing of solid state batteries largely comprehend the quest of new cathode materials. Alkali metal pyrophosphates are promising group of cathode materials both for lithium and sodium rechargeable batteries. The pyrophosphates are the entirety of (P_2O_7) based compounds. These P_2O_7 units are connected with transition metal octahedral (MO_6) forming a robust framework. The alkali ions and transition metal atoms can be inter-site mixed and MO_6 octahedra can be distorted (because of the elongated M–O bonds), consequently leading to polymorphism [215]. Favourably, this three dimensional $(P_2O_7)^{-4}$ framework has multiple sites for mobile ions. The attractiveness of the pyrophosphate group is thoroughly related to its rich crystal chemistry and its variation, robust and chemically stable structure, convenience of synthesis and possible multidimensional ionic conduction pathways. In pyrophosphates the unequal metal–O and O–O bond lengths create a characteristic feature of diphosphate

compounds, where P–O bond length with bridging O of P_2O_7 unit is longer than that P–O bond length with terminal O atoms [215].

1.3.1 Lithium metal pyrophosphates

One-Lithium Metal Pyrophosphates ($LiMP_2O_7$)

One well explored lithium pyrophosphate is $LiFeP_2O_7$ reported by Genkina et al. [216] in 1985. It has monoclinic crystal structure with space group $P2_1$ or $P2_1/a$ [216-218]. In $LiFeP_2O_7$ crystal each FeO_6 octahedra is connected to six PO_4 tetrahedra which belong to five different phosphate groups. Each FeO_6 octahedron shares two edges with same P_2O_7 group, thus forming $[FeP_2O_{11}]$ units. Hosting Li atoms are stowed into the tunnels [215, 219, 220]. That sharing pattern is common in plenty of diphosphate systems. Wurm et al. [221] reported that $LiFeP_2O_7$ has theoretical capacity of 113 mAh/g, but the obtained one not being able to exceed 73 mAh/g. Venckute et al. [222] investigated the electrical properties of $LiFeP_2O_7$. The ionic conductivity value of $3.33 \cdot 10^{-7}$ S/m and the activation energy of 1.11 eV at 500 K temperature was reported.

Also $LiFe_{1.5}P_2O_7$ was introduced by Ramana et al. [223] When $LiFe_{1.5}P_2O_7$ was tested as cathode, it showed reversible capacity of 95 mAh/g. That value is larger than that of $LiFeP_2O_7$. Also the redox potential of $LiFe_{1.5}P_2O_7$ was higher than that of $LiFeP_2O_7$ (3.2 V for $LiFe_{1.5}P_2O_7$ vs. 2.9 V for $LiFeP_2O_7$).

Vanadium pyrophosphates have also attracted considerable attention in Li-ion battery research because of the chemical activity of vanadium and the structural stability of phosphate [224]. $LiVP_2O_7$ was described for first time in 1990 by Lii at al. [225]. It is isostructural to $LiFeP_2O_7$ and also has a monoclinic framework. It consists of a distorted VO_6 octahedra and P_2O_7 units. In 2017 Yu et al. [226] prepared $LiVP_2O_7$/C – it is carbon coated $LiVP_2O_7$ synthesized by the sol-gel method. In the electrochemical testing, the sample with carbon content of 6.63 wt% prepared at 800 °C exhibited very good electrochemical capacity, the initial discharge capacity was 102.3 mAh/g, closing to the theoretical capacity of 115.5 mAh/g. After 50 cycles the capacity retention was 96.2%. Meanwhile, the redox potential was found to be 4.2 V. This excellent electrochemical performance is attributed to the carbon coating and the small particle sizes [226].

In 2008 Zatovskii et al [227] discovered $LiTiP_2O_7$. It has monoclinic crystal system identical to $LiFeP_2O_7$ and $LiVP_2O_7$. Moreover, the structural and electrochemical properties of TiP_2O_7 were studied in detail. It was found

that TiP_2O_7 compound has a cubic (a = b = c = 23.632 Å) crystal structure [228-232]. A reversible capacity of 100 mAh/g and redox potential of 2.6 V was reported [233-236] for $LiVP_2O_7$ compound. It was found and reported [237] that TiP_2O_7 undergoes a phase transition from cubic α-phase (a = 32.52 Å) to cubic β-phase (a = 7.80 Å) at 730 °C. Moreover, electrical properties were studied. It was found [238] that TiP_2O_7 is almost pure protonic conductor and that protons migrate through a hoping mechanism. The protonic conductivity at 900 °C under wet atmosphere conditions was found to be $5 \cdot 10^{-4}$ S/cm. The obvious bends around 700 °C probably indicates the phase transition mentioned previously. In 2012 Rai et al. [239] prepared a $TiP_2O_7/Li_{2.6}Co_{0.4}N$ composite (32 wt% and 68 wt%, respectively). That composite demonstrated high initial coulombic efficiency of 98% and huge reversible capacity of 652.57 mAh/g versus lithium. That indicates its use as a promising anode for secondary Li-ion batteries.

Oueslati [240] prepared another lithium pyrophosphate $LiYP_2O_7$ and investigated its structure and conductivity properties. The monoclinic crystal symmetry with space group P2/m was reported. Surprisingly, the conductivity was found to be $4.6 \cdot 10^{-5}$ S/cm at 600 K temperature. It is one order higher value that that of $LiFeP_2O_7$ [241] at the same temperature.

About two times less conductive than $LiYP_2O_7$ was another compound $LiCrP_2O_7$. It also has monoclinic crystal structure with space group $P2_1$ [242-244]. The obtained conductivity was $2.1 \cdot 10^{-5}$ S/cm [245] at 600 K temperature. But the lack of reliable electrochemical investigations still remains speaking considering $LiCrP_2O_7$.

The solid solutions are also negotiable cathode materials. The solid solution $Li_{0.9}Fe_{0.9}Ti_{0.1}P_2O_7$ was prepared be Venckute et al. [222] The ionic conductivity value of $1.5 \cdot 10^{-6}$ S/m and the activation energy of 0.94 eV at 500 K temperature were reported. Surprisingly, this more complex $Li_{0.9}Fe_{0.9}Ti_{0.1}P_2O_7$ compound was found to be more conductive by nearly 5 times compared to that previously mentioned $LiFeP_2O_7$.

Two-Lithium Metal Pyrophosphates ($Li_2MP_2O_7$)

Double lithium iron pyrophosphates are also candidates for cathodes. $Li_2FeP_2O_7$ was synthesized for the first time by Mahesh et al. in 2007. [246] Soon $Li_2FeP_2O_7$ was also synthesized by solid state method by Nishimura et al. [247] Zhang et al. showed that the best lithium source for $Li_2FeP_2O_7$ synthesis is LiH_2PO_4 and the optimum synthesis temperature is 650 °C.

[248] It was revealed that $Li_2FeP_2O_7$ has monoclinic crystal structure and the reported space group is $P2_1/c$ [247, 249]. Its reversible electrode capacity was found to be 100 mAh/g which is close to theoretical value of 110 mAh/g. Actually, 1 μm particles without any special treatment such as nanosizing or carbon coating were used. The redox plateau was centered at about 3.5 V, thus demonstrating the highest value among all Fe containing phosphate cathodes [215, 250]. $Li_2FeP_2O_7$ and its derivatives possibly could provide a new platform for related lithium battery cathode research demonstrating similar or superior characteristics than commercial olivine $LiFePO_4$, which has been recognized as the most convenient positive cathode for a lithium-ion battery system for wholesale applications, such as hybrid-electric or fully-electric vehicles [247, 251]. Few years later the same group of Nishimura synthesized $Li_2FeP_2O_7$ in a so called "splash combustion synthesis" method [252] which is drastically shortened in time compared to conventional solid state synthesis method (1 minute instead of 10 hours). Reversible capacity was found to be 100 mAh/g with a 3.5 V Fe^{3+}/Fe^{2+} redox activity. These values are very similar to the ones obtained in 2010 by Nishimura et al. [247], but the rate of synthesis is much higher. Anyway, $LiFePO_4$ still remains one of the promising cathode materials for next generation power lithium ion batteries due to its good safety, cyclability, and rate capability [253].

Further considering lithium manganese phosphates are very engrossing and characterful because manganese can exhibit several oxidation states (Mn^{II}, Mn^{III} and Mn^{IV}) and can provide high redox potentials vs Li [254]. $Li_2MnP_2O_7$ was first proposed by Adam et al. [254] in 2008. In this structure, the manganese polyhedral and phosphate tetrahedral form a 3D $[MnP_2O_7]_\infty$ framework consisting of MnO_5 trigonal bipyramids (Mn1), MnO_6 octahedra (Mn2) and typical diphosphate groups P_2O_7. Several years later Nishimura et al. [255] discovered a new metastable monoclinic polymorph β-$Li_2MnP_2O_7$ (sintered at 400-500 °C). Differently from the structure reported by Adam, in β-$Li_2MnP_2O_7$ crystal, both the Mn sites Mn1 and Mn2 are octahedral corner sharing MnO_6 units (no edge sharing Mn_2O_9 ones) whereas Li sites are tetrahedral LiO_4 units. The reversible electrochemical activity at around 4 V was demonstrated by electrochemical measurements with a Li cell while a reversible capacity was of about 30 mAh/g. The Mn^{3+}/Mn^{2+} redox potential is centered at 4.45 V vs. Li [256]. It is the highest voltage ever obtained for the Mn^{3+}/Mn^{2+} redox couple in any manganese-based cathode material.

One of $Li_2FeP_2O_7$ homologues is $Li_2CoP_2O_7$. It also has a monoclinic crystal structure and $P2_1/c$ symmetry [257]. The electrochemical activity of $Li_2CoP_2O_7$ was found from galvanostatic voltage profile. The discharge capacity was 85 mAh/g with redox plateau at 4.9 V [257].

Another homologue is $Li_2CuP_2O_7$. It was first described by Spirlet et al. [258] in 1993. Since then it has been investigated only on several occasions [259-261]. Reversible phase transition at 622 K has been evidenced by DSC (differential scanning calorimetry) and confirmed by the analysis of dielectric and electric properties. The electrical conductivity of $1.75 \cdot 10^{-3}$ S/cm at 400 °C was obtained [260]. The electrochemical capacity was reported up to 180 mAh/g [261].

Kishore et al. [262] synthesized $Li_2VP_2O_7$ compound as cathode material by ion exchange route method. XRD measurements showed it having a monoclinic structure in space group $P2_1/c$. The V^{4+}/V^{5+} redox activity at around 4.1 V was found, but unfortunately $Li_2VP_2O_7$ demonstrated poor Li insertion reversibility with a 30 mAh/g capacity parameters.

The successful research of isostructural pyrophosphates $Li_2MP_2O_7$ (M = Fe, Mn, Co) was an encouragement to form and explore their solid-solution phases [219, 263-265]. Zhou et al. [263] analysed various $Li_2Mn_{1-y}Fe_yP_2O_7$ ($0 < y < 1$) compounds. The electrochemical capacity improves as the Fe concentration increases, as do the intensities of the redox peaks of the cyclic voltammogram. That observation indicates the higher lithium-ion diffusivity in the iron-containing phase. The two Li ions in the three-dimensional tunnel structure of the solid solution allows for the cycling of more than one Li-ion per redox center. The second oxidation peak at ~5 V and ~5.3 V is found from the cyclic voltammograms, thereby indicating the extraction of the second lithium ion [263]. Hence, if a stable electrolyte is found, the electrochemical capacities over 200 mAh/g can be achieved. Slightly less promising was $Li_{2-x}CoP_2O_7$: redox potential was of 4.9 V and electrode capacity was of 85 mAh/g on discharge at C/20 [257].

1.3.2 Sodium metal pyrophosphates

One-Sodium Metal Pyrophosphates ($NaMP_2O_7$)

Pyrophosphates with only one sodium metal have not been widely investigated. The first sodium metal pyrophosphate was $NaFeP_2O_7$ introduced by F. d'Yvoire et al. in 1969 [215]. Unfortunately, it was thermally unstable and therefore was transformed to a high temperature polymorph $NaFeP_2O_7$-II (over 750 °C). Some groups analyzed that

polymorph in more detail [266-269], but only considering the structure – no electrochemical or electrical properties were investigated for a long time. In 2015 Nasri et al. [270] analyzed the electrical properties of $NaFeP_2O_7$-II. The obtained conductivity was of $1.16 \cdot 10^{-6}$ S/cm with the activation energy of 0.84 eV at 300 °C. However, the obtained conductivity value is about one order lower than that of $AgFeP_2O_7$ at the same temperature [267].

The group of Leclaire synthesized $NaTiP_2O_7$ [271] and $NaMoP_2O_7$ [272] in 1988. One year later Wang et al. [273] synthesized $NaVP_2O_7$. It was investigated also by other groups [274, 275]. All of them were found to be isostructural to $NaFeP_2O_7$-II. However, similarly to $NaFeP_2O_7$ no electrochemical or electrical properties were investigated for decades probably due to poor parameters and characteristics expected [215]. Recently some investigations were performed but the obtained results are not remarkable. $NaVP_2O_7$ showed an initial discharge capacity of 38.4 mA/g at 1/20C in the voltage range of 2.5-4.0 V. It was suggested that part of the sodium ions in the lattice structure exist as structural stabilizers and cause lattice distortion upon desodiation and high intrinsic internal resistance limiting the phase transition kinetics between pristine $NaVP_2O_7$ and desodiated $Na_{1-x}VP_2O_7$ [276]. The electrochemical characteristics of $NaMoP_2O_7$ were found to be lower than adequate and not suitable for using as cathode material [277]. The structure, electrochemical and electrical characteristics of $NaYP_2O_7$ were described. $NaYP_2O_7$ crystallizes in the noncentrosymetric space group $P2_1$ [278] and exhibits the ionic conductivity of about 10^{-7} S/cm at 400 K with constant activation energy of 0.65 eV in the temperature range 400-560 K [279]. Taher et al. [280] prepared $NaAlP_2O_7$ in 2017. The monoclinic crystal system with space group $P2_1/c$ was reported. The impedance measurements revealed the conductivity value of 1.16×10^{-5} S/cm^{-1} at 613 K and activation energy of 0.95 eV.

Two-Sodium Metal Pyrophosphates ($Na_2MP_2O_7$)

$Na_2CoP_2O_7$ started the era of two-sodium containing pyrophosphates when it was described by Erragh et al. [281] in 1991. Three different crystal phases can be attributed to $Na_2CoP_2O_7$: orthorhombic $Na_2CoP_2O_7$-I ($P2_1/cn$), triclinic $Na_2CoP_2O_7$-II (P-1) and tetragonal $Na_2CoP_2O_7$-III ($P4_2/mmm$) [281, 282]. In the structure of the triclinic phase 1D tunnels exist while 3D tunnels are attributed to the tetragonal and orthorhombic phases. $Na_2CoP_2O_7$ showed the maximum reversible capacity of 80 mAh/g with redox potential of 3 V [283].

In 1992 Raveau et al. [284] synthesized layered $Na_2VP_2O_7$. The monoclinic crystal structure and $P2_1/c$ space group was reported. Later Daidouh et al. [285] investigated $Na_2VP_2O_7$ in more detail and found that it has two phases: tetragonal below 600 °C and monoclinic above 600 °C. The ionic conductivity of $3.05 \cdot 10^{-5}$ S/cm was reported for tetragonal $Na_2VP_2O_7$-II at 310 °C with an activation energy of 0.49 eV.

In 1995 Etheredge et al. [286] synthesized monoclinic (space group C2/c) $Na_2CuP_2O_7$. Simultaneously Erragh et al. [287] found out that $Na_2CuP_2O_7$ undergo an irreversible phase transition to β- $Na_2CuP_2O_7$ at 570 °C. The space group changes from $P2_1/n$ to C2/c, but still remains monoclinic. $Na_2CuP_2O_7$ is moderate pure ionic conductor with the conductivity value of $1.1 \cdot 10^{-7}$ S/m at 210 °C temperature [288]. $Na_2CuP_2O_7$ being 2D conductor isostructural to $Li_2CuP_2O_7$ allows ion exchange forming solid solutions of $Na_{2-x}Li_xCuP_2O_7$, [215] but no investigations are done so far.

$Na_2ZnP_2O_7$ was also investigated as a cathode material. The structure of $Na_2ZnP_2O_7$ was described in detail by some research groups [289-294]. It has a tetragonal crystal system with space group $P4_2/n$. As showed by DTA (differential thermal analysis) measurements, $Na_2ZnP_2O_7$ compound is thermally fairly stable [292]. It can be prepared by solid state synthesis method and through crystallization from a glass [295]. Unfortunately, the ionic conductivity of $Na_2ZnP_2O_7$ is low: Chouaib et al. [296] reported the ionic value of $3.4 \cdot 10^{-7}$ S/m at 330 °C with activation energy of 0.95 eV.

Only at the beginning of this decade $Na_2FeP_2O_7$ was introduced which has triclinic P-1 crystal structure. Several publications were prepared in latter years about the synthesis [297-301] and both electrical and electrochemical properties [302-310]. The obtained redox potential Fe^{3+}/Fe^{2+} of $Na_2FeP_2O_7$ is about of 2.9 V (vs. Na/Na^+) and the reported electrochemical capacity varies in the range from 82 mAh/g to 93 mAh/g. $Na_2FeP_2O_7$ when tested as a positive electrode demonstrated excellent cyclability, exceeding 300 cycles. These characteristics include both capacity retention and coulombic efficiency [303]. The capacity retention exceeds 90% over 1000 cycles [306]. Various techniques were used for synthesis: solid state method, glucose-assisted solid state method, glass-ceramics method, solution-combustion synthesis method, Pechini-based wet chemistry approach method. $Na_2FeP_2O_7$ demonstrated particularly good thermal stability up to 500 °C, even in the partially desodiated state $NaFeP_2O_7$, which presuppose its safe nature, a property that is extremely important for large-scale battery applications [308].

Another very perspective compound $Na_2MnP_2O_7$ was discovered in 1998 by two researchers Huang and Hwu [311]. The samples were prepared by solid state synthesis method using oxide precursors Na_2O, MnO_2 and P_2O_5. The maximum temperature reached during the synthesis was about 750 °C. Two years later another polymorph $Na_2MnP_2O_7$-II was discovered by Lokanath et al. [312]. Both polymorphs (see Fig. 1.2) adopt triclinic crystal system with space group P-1.

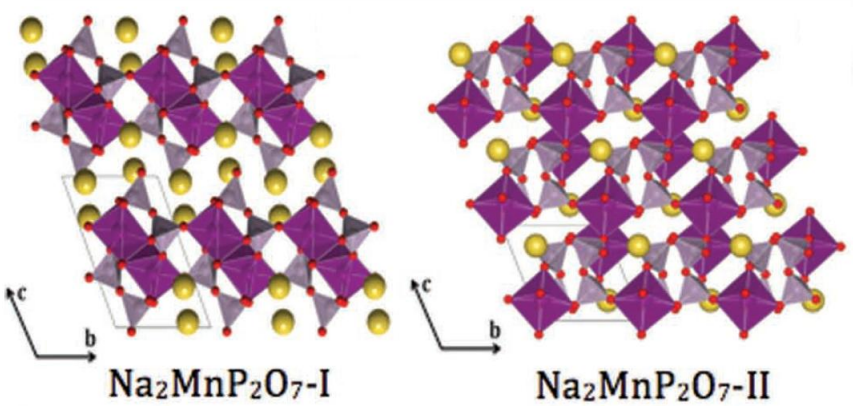

Fig. 1.2. The crystal structures of $Na_2MnP_2O_7$-I with connected edge sharing MnO_6 units and $Na_2MnP_2O_7$-II with disconnected corner-sharing MnO_6 units [215].

$Na_2MnP_2O_7$-I adopts a very unique structure type consisting of $Mn_4P_4O_{26}$ cage. This 3D framework consists of parallel, 2D (Mn-P-O) slabs with Na^+ ions located between them. The (Mn-P-O) slab is made of Mn_2O_{10} dimmers (building units made by two adjacent, edge sharing MnO_6 octahedra) and P_2O_7 groups. Two Mn_2O_{10} dimmers and two P_2O_7 groups are alternately arranged forming the $Mn_4P_4O_{26}$ cage. All the Mn atoms are octahedrally coordinated with oxygen atoms from four P_2O_7 groups, thus forming distorted octahedra [215, 311, 313].

The structure of $Na_2MnP_2O_7$-II is similar to $Na_2MnP_2O_7$-I one, but the lattice parameters are different and the bond angles (Mn-O-Mn and P-O-P) are prominently different. $Na_2MnP_2O_7$-II was found to be electrochemical active with a potential of 3.6-3.8 V vs. Na/Na^+ and the reversible capacity of 80-90 mAh/g at room temperature [314, 315]. That redox potential value is the highest among all manganese based cathodes ever reported. $Na_2MnP_2O_7$-II is predicted to exhibit curved diffusion pathways into 3D structure with the migration energy of 0.58 eV [316].

Also the $Na_2Fe_{0.5}Mn_{0.5}P_2O_7$ solid solution was prepared by conventional solid state method [317]. It adopts triclinic crystal structure with (P-1) space

group. It demonstrated a reversible capacity of about 80 mAh/g at a C/20 rate with an average redox potential of 3.2 V vs. Na/Na^+. The rate capability of $Na_2Fe_{0.5}Mn_{0.5}P_2O_7$ is slightly better than that of $Na_2MnP_2O_7$. It was demonstrated by CV analyses that $Na_2Fe_{0.5}Mn_{0.5}P_2O_7$ undergoes a single phase reaction rather than a biphasic reaction. It can be attributed to different sodium atoms coordination environment and different Na site occupancy in comparison to other pyrophosphate materials ($Na_2MnP_2O_7$ and $Na_2FeP_2O_7$) [317].

Owing to its simple synthesis, usage of low cost abundant elements, well-established reversibility, $Na_2MnP_2O_7$ is attractive cathode material for ASSBs [314, 316].

Solid sodium based solutions are also in view of interest. Sodium is partially changed by caesium and copper [311], zinc [318], manganese [319] and especially iron-manganese [317, 320-322]. $Na_2Fe_{0.5}Mn_{0.5}P_2O_7$ (refined in a monoclinic framework with space group $P2_1/c$) is electrochemically active and exhibits a reversible capacity of 80 mAh/g at a C/20 rate with an average redox potential of 3.2 V. (vs. Na/Na^+). It is also noticed that the rate capability of $Na_2Fe_{0.5}Mn_{0.5}P_2O_7$ is better than $Na_2MnP_2O_7$. The thermal stability of $Na_2Fe_{0.5}Mn_{0.5}P_2O_7$ as a cathode material was found to be good enough [317]. Also the multicomponent transition metals pyrophosphate $Na_2Fe_{0.33}Mn_{0.33}Co_{0.33}P_2O_7$ cathode was investigated [323]. That compound demonstrated suitable thermal stability even in the desodiated state. Despite of the analyzed structures of some sodium based solutions the lack of conductivity measurements still remains.

1.4 Peculiarities of Li^+/Na^+ ions transport and proton conductivity

The Li^+ and Na^+ ions transport within the solid electrolyte is a fundamental process for the treatment and operation of ASSBs. The charge transport mechanisms within the inorganic, solid superionic conductors can be analyzed in terms of these two factors: charge carrier type (or diffusive defects) and diffusion pathway [324]. Also, the peculiarities of conductivity changes in point of temperature and the phenomenon of the proton conductivity will be discussed in this chapter.

1.4.1 Point defects

The types of charge carriers are based on defect chemistry and particularly on point defect chemistry. Charged point defects can also form

clusters, which are bigger than detached point defects and can be a trigger for considerable conductivity changes. The point defects are these ones: vacancies (missing atom in a site of a crystal lattice), dopants (intentionally added foreign atoms), impurities (unintentionally added foreign atoms), Frenkel defects (pairs of vacancies and interstitials), Schotky defects, interstitial defects (an atom occupying an interstitial site where no one could be originally found in a perfect crystal), electronic defects (conduction electrons, holes) [325, 326]. The overall defect structure in a crystal is resulted by energy minimization in terms of enthalpy and entropy of formation and migration, charge and mass balance, and preservation of the structure (known as "site ratio balance") [327]. The dopants added to the solid electrolyte can change the crystal parameters, increase [328] or decrease [329] the transport of cations within it.

A vacancy is a common defect for all inorganic solid electrolytes. For example, in perovskite $Li_{3x}La_{2/3-x}TiO_3$ (LLTO), actually one-third of A sites are unoccupied by lanthanum ions. In garnet $Li_7La_3Zr_2O_{12}$ (LLO), there is 20% unoccupied (by lithium) tetrahedral (24d) sites and 60% unoccupied (by lithium) octahedral (48g) sites.

The Kröger-Vink notation can be used to describe the point defects and their reactions. We can describe simple intrinsic point defects, such as Schotky and Frenkel ones. For example, the reaction of a Schottky-type defect in sodium chloride follows the form:

$$Na_{Na}^{\times} + Cl_{Cl}^{\times} \rightarrow V_{Na}^{\prime} + V_{Cl}^{\bullet} + NaCl. \quad (1.1)$$

Similarly, the reaction of a Frenkel-type defect in cadmium follows the form:

$$Cd_{Cd}^{\times} \rightarrow V_{Cd}^{\prime\prime} + Cd_{i}^{\bullet\bullet}. \quad (1.2)$$

In these equations the body corresponds the species involved (chemical element or a vacancy denoted by the letter "V"), the subscripts represent either a lattice or an interstitial site (denoted by the letter "i"), the superscripts indicate the effective electric charge (neutral, $^{\times}$; positive, $^{\bullet}$; or negative, $^{\prime}$) of the particular site with respect to idealized pure crystal. [325, 327, 330].

The point defects can be generated by doping or substitution (extrinsic defects). This effect can cause the changes in electrochemical and (or) electrical parameters and characteristics. For example, doping Mn^{3+} at Ti^{4+} sites in perovskite-type $BaTiO_3$, the defect reaction follows the form:

$$Mn_2O_3 + BaO_2 \xrightarrow{BaTiO_3} Ba_{Ba}^{\times} + 2Mn_{Ti}^{\prime} + 5O_O^{\times} + V_O^{\bullet\bullet}. \quad (1.3)$$

Therefore, we can find here negatively charged substitutional Mn'_{Ti}, positively charged vacancy $V_O^{\bullet\bullet}$ and both neutral $Ba_{Ba}^{\times}$ and $O_O^{\times}$.

The point defects in an inorganic electrolyte can emerge under certain extreme conditions (for instance low oxygen partial pressure), applied electrode potential and Li or Na chemical potential [324]. Shi et al. [331, 332] analyzed diffusion mechanisms in crystalline Li_2CO_3. They found that the dominant diffusion carriers in Li_2CO_3 are Li-ion interstitials when the applied voltage is below 0.98 V and Li-ion vacancies become the dominant charge carrier type when the applied voltage exceeds 3.98 V. Li^+ vacancies were reported to diffuse via a typical direct hoping mechanism, but the excess interstitial Li^+ were found to diffuse via iterant knock-off mechanism by steadily displacing Li-ions in neighbouring sites. The Li^+ interstitial conductivity was found to be 5 orders of magnitude faster than that of a vacancy.

Three diffusion types are known in ionic conduction phenomenon of solid electrolytes: directly hopping interstitial, interstitial knock-off and directly hopping vacancy [324]. Li or Na ions diffuse mainly by an interstitial mechanism (related to Frenkel disorder) due to their small radius [6].

1.4.2 Diffusion pathway

Diffusion pathway is mostly determined by the topology of the anion arrangement. The fundamental phenomenon of mobile species diffusion is the transference of the ion among stable sites (local minima) through an environment having higher energy (periodic bottleneck points) and the highest value of that energy is the activation energy for migration of ions [333, 334].

One point is the size of a mobile specie. An ion should be of favourable size [335]. When the migrating cation is too small, it “sinks” into a deep electrostatic well containing closer near neighbouring counteriors, the diffusivity becomes reduced and the activation energy enhanced. On the other hand, when the migrating cation is too large it experiences high forces migrating between the bottlenecks in a lattice, thus the diffusivity also becomes reduced and the activation energy enhanced [335, 336].

While aliovalent substitution changes the amount of charge carriers, the conductivity often passes though a maximum in terms of mobile species added into the crystal lattice. That mobility dependency of charge carriers’ concentration is related to the interaction of mobile ions and to the distortion

of a local structure [337, 338]. When the concentration of substitutional species becomes critical, the activation energy increases due the distortion of a lattice and the latter effect surpasses that one of increasing the concentration of charge carriers which leads to the decrease of the ionic conductivity. [336] For example, it is well known that in $Li_{3x}La_{2/3-x}\beta_{1/3-2x}TiO_3$ perovskites of LLTO type the Li-ion conductivity curve has a shape of a dome as a function of a Li substitution [339, 340]. The maximum ionic conductivity value is for $x \approx 0.10$ and that corresponds an A-site vacancy concentration of about 10%. Li ions migrate through A-site vacancies and the bottleneck for lithium ion migration is constituted by four oxygen anions separating adjacent A sites [339]. The analogous effect is observed also in some electrolytes of other type, for example, in NASICONs [113]. Similarly, enlarging the bottlenecks by using greater M ion sizes in $LiMM'(PO_4)_3$, where M and M′ are Ge, Ti, Sn, and Hf, the ionic conductivity can be increased up to four order of magnitude [341].

Ion valency also heavily influences the diffusivity of mobile species. Ionic conductivity decreases with the increased valency. That phenomenon is related to enhanced electrostatic interaction between the mobile species and immobile ions of a crystal skeleton. Tarneberg et al. [342] demonstrated that the cationic diffusion coefficient in lithium sulphate Li_2SO_4 can differ by 3 orders of magnitude and activation energy by 3.5 times of magnitude when comparing monovalent, divalent and trivalent ions. Thus it is no wonder that the monovalent cations (Ag^+, Li^+, Na^+) are dominant in solid electrolytes and have the highest values of the ionic conductivity.

The stable sites in ionic materials are usually tetrahedral or octahedral linked to other polyhedral sites through shared anion triangles. A superb task investigating the favourable anion arrangement was recently done by Wang et al. [343] They analyzed crystal structure, calculated Li-ion migration barriers and probability densities. It was reported that “an underlying body-centered cubic-like (bcc) anion framework, which allows direct Li hops between adjacent tetrahedral sites, is most desirable for achieving high ionic conductivity” [343]. While bcc arrangement remains optimal across all volumes of a lattice, in fcc (face centered cubic) and hcp (hexagonal close packed) ones the transference mechanism of ions varies with the value of volume. The higher values of the activation energy of ions migration are attributed for fcc and hcp lattices and this is particularly evident in specifically small volume values when ions pass through an extremely small 3D bottlenecks. That relation among the ionic conductivity and the lattice

volume per lithium atom within a crystal lattice with isovalent substitution is mostly demonstrated in LISICONs [344-347], NASICONs [135, 341] and perovskites [348].

The better conductivity values of cubic phase vs. tetragonal phase were recently noted by Meier et al. [349] in LLZO type materials. The presence of vacancies in cubic LLZO strongly lowers the activation energy and enhances Li-ion conductivity. Now the latter group intensively investigates the problem of creation additional Li-ion vacancies by doping the crystal with supervalent cations [350-354] while stabilizing the cubic phase at normal ambient temperatures.

It is desirable that all sites within the diffusion range in a network should be energetically close to equivalent, with wide channels between them. These conditions are observable in many sulphide materials, for example $Li_{10}GeP_2S_{12}$ and $Li_7P_3S_{11}$ and sulphur sublatices within them very closely match bcc lattice. The activation energy of a Li^+ cation in the bcc S^{2-} lattice along the path between the bcc (T-T type migration) sites is about three orders of magnitude lower in conductivity than in the presence of the octahedral sites along the path between hcp/fcc (T-O-T type migration) sites. Hence, the high value of the conductivity of above mentioned sulphides is caused by a percolating network composed solely of crystallographically and energetically equivalent tetrahedral sites and no migration through sites with prominently discrepant coordination is necessary.

Apart from sulphides, networks composed of solely tetrahedral sites for the mobile cations exist in argyrodite Li_7PS_6 and its derivatives with halogen atoms Li_6PS_5X (X = Cl, Br, I) [355], also in sodium containing cubic Na_3PS_4 [356, 357]. The mechanisms of cation transference through the face-shared tetrahedral sites are particularly similar to the solid electrolytes of bcc type. The problem is to transfer the above principles to other cations and lattices for designing the solid batteries.

The ion conductivity of a superionic conductor can be expressed as:

$$\sigma = \frac{\sigma_0}{T} e^{-E_A/k_B T}, \qquad (1.4)$$

where T is the absolute temperature in Kelvin, k_B is the Boltzmann constant and E_A is the activation energy for diffusion. Plotting the conductivity in a logarithmic scale versus reciprocal temperature one can calculate the activation energy graphically from a slope.

The interesting influence of the changes of unit cell parametres on conductivity is also observed in lithium lanthanum titanate $Li_{0.5-}$

$_xNa_xLa_{0.5}TiO_3$ (LNLTO) and in lithium lanthanum niobate $Li_{3x}La_{2/3-x}\gamma_{4/3-2x}Nb_2O_6$ (LLNbO), which both have defected perovskite structure and ionic conductivity values of (10^{-3}-10^{-5} S/cm) at room temperatures [176, 358, 359]. In the $Li_{0.5-x}Na_xLa_{0.5}TiO_3$ crystal lithium ions are partially exchanged by sodium, which do not take part in the conduction process due to the difference of ionic radii. Therefore sodium ions block lithium conduction pathways by sharing the same crystallographic sites. In the case of LNLTO (lithium lanthanum titanium oxide doped with sodium) percolation model has been successfully applied to character ionic conductivity [360-362]. It was shown [363, 364] that in LLTO system in the temperature interval from 290 K to 400 K mobile ion activation energy is 0.3 eV and the conductivity changes according to Arrhenius law, but above 400 K non-Arrhenius behaviour of conductivity was observed and Vogel–Fulcher–Tammann (VFT) equation can be used to its' description [365, 366]. The data also show that lithium conductivity is affected by a number of structural vacancies and, furthermore, by bottleneck sizes of lithium pathways. In order to recognize the peculiarities of lithium transport in defected perovskites lithium lanthanum niobate $Li_{3x}La_{2/3-x}\gamma_{4/3-2x}Nb_2O_6$ was also investigated [367-369]. The investigation of Li→Na substitution in this system showed that the ionic conductivity cannot be described by percolation model, because this system contains significantly higher vacancy concentration in lithium-lanthanum sublattice compared to $Li_{3x}La_{2/3-x}\gamma_{1/3-2x}TiO_3$ [370, 371].

The ionic conductivity in the system $Li_{0.5-y}Na_yLa_{0.5}Nb_2O_6$ at room temperature shows a maximum value of $1.3\cdot10^{-5}$ S/m for y = 0.43 [369, 370]. Keeping in mind, that sodium ions do not participate in the conduction process, authors [370] explain this maximum originating from the increase of perovskite unit cell when lithium is exchanged with sodium, and this leads to the increase of Li-ion mobility. However, when y > 0.4 the ionic conductivity significantly decreases because of decrement of charge carriers' concentration of the mobile ions. Jimenez et al. [372] have shown, that La^{3+} ions exceptionally occupy positions in the z = 0 plain of the $Li_{0.5-y}Na_yLa_{0.5}Nb_2O_6$ lattice when $0 \le y \le 0.3$ (see Fig. 1.3) and consequently 2D conductivity takes place. When the amount of sodium is increased (y > 0.3), La^{3+} cations distribute between z = 0 and 1/2 plains and the transition from 2D to 3D conductivity was observed [369].

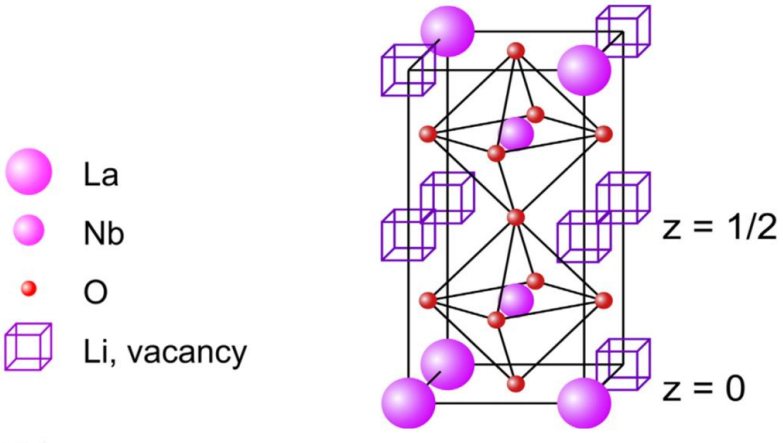

Fig. 1.3. Crystallographic structure of $Li_{3x}La_{2/3-x}\gamma_{4/3-2x}Nb_2O_6$.

The oxide-based LNLTO and LLNbO conductors deserve much attention because of their possible applications as solid electrolytes or electrode materials in various electrochemical devices such as batteries, sensors, supercapacitors etc. [373-377].

1.4.3 Conductivity anomalies in point of temperature

Temperature dependence of electrical conductivity can be analysed to identify different processes going on in ionic conductors. Thermally activated ionic jumps in the lattice are always to be expected in solid electrolytes, which result in ionic conductivity change with temperature according to Arrhenius law: $\sigma = \sigma_0 \exp(-\Delta E/\mathrm{k_B}T)$, where σ_0 is preexponential factor, ΔE – activation energy of conductivity, k_B – Boltzmann constant. In this case plotting the logarithm of conductivity versus inversed temperature leads to linear dependence as shown in Fig. 1.4a. The deviation from the linearity can sometimes be observed. A rapid increase of conductivity at a fixed temperature T_0 like in Fig. 1.4b most likely indicate a phase transition to superionic state. The typical examples of conductivity change when order-disorder phase transition takes place are AgI and related materials [378], $La_2Mo_2O_9$ [379], Bi_2O_3 [380]. The activation energy decreases after a phase transition to superionic state, as the energy barriers for the mobile ions decrease. Smooth phase transitions were also found to affect temperature dependences of conductivity [381]. Such transitions do not include a significant increase in conductivity at a certain temperature T_0, but it leads to lowering of activation energy at higher

temperatures as it is schematically shown in Fig. 1.4c. The nature of such phase transitions is different and may involve environment change for mobile ions or the change of mobile ion occupancies in some particular lattice sites. A good example is NASICON-type lithium solid electrolytes [382, 383]. Both types of phase transitions lead to lowering of conductivity activation energy at high temperature. In some particular cases the increase of the activation energy, as it is shown in Fig. 1.4d, was also observed. The reason for that can be the ion transport mechanism change. For example, $Li_{3x}La_{2/3-x}TiO_3$ has a layered perovskite structure and the conductivity at low temperatures is two-dimensional. Above about 270 K lithium ions can overcome the energy barriers between different conduction layers, and the conductivity of $Li_{3x}La_{2/3-x}TiO_3$ becomes three-dimensional, which leads to the activation energy increase [384]. The situation shown in Fig. 1.4e seems to be very uncommon, but it was also found experimentally [385-387] when the measurements were performed in humidified atmosphere. In the lower temperature range the conductivity decrease is observed, hence the activation energy of conductivity is negative. At low temperatures the overall conductivity is enhanced because of proton contribution, which is related to the absorbed water. The hydration level decreases with increasing temperature, driving the total conductivity through the minimum, and with further temperature increase the conductivity follows Arrhenius law.

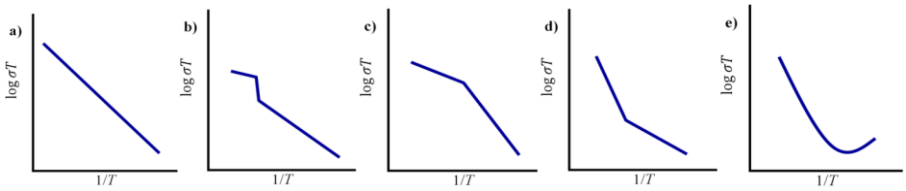

Fig. 1.4. Commonly found temperature dependences of conductivity in solid electrolytes (in Arrhenius representation). a) shows thermal activation, b) indicates first order phase transition, c) – smooth phase transition, d) – ion transport mechanism change, e) – mixed ionic and proton conductivity in humid atmosphere.

1.5 Proton conductivity

Water is known as a typical proton conductor, because of frequent occurrence of hydrogen bonds in water (related to the electrostatic interaction) additionally to covalent bonds $X^{\delta-}$–$H^{\delta+}$, where X denotes the

electronegative atom. The conduction is based on so called “Hop-turn” or just “proton-hoping” mechanism, also known as Grotthuss mechanism [388-390], because Grotthuss was the first who explained the protonic conductivity in water in 1806 [391].

It is known that water normally is slightly ionized [392]. Some of H_2O molecules split into H^+ and OH^- as in the equation below:

$$H_2O \leftrightarrow H^+ + OH^-. \quad (1.5)$$

The formed H^+ is very reactive and immediately binds with intact adjacent water molecule thus forming hydronium (H_3O^+) ion as showed by equation below:

$$H_2O + H^+ \leftrightarrow H_3O^+. \quad (1.6)$$

The process of proton hopping is schematically shown in Fig. 1.5. It is obvious that H^+ ion released by hydronium ion is immediately accepted by adjacent water molecule and another hydronium ion is formed. The latter process is very rapid and the phenomenon of H^+ ions movement towards the cathode is observed.

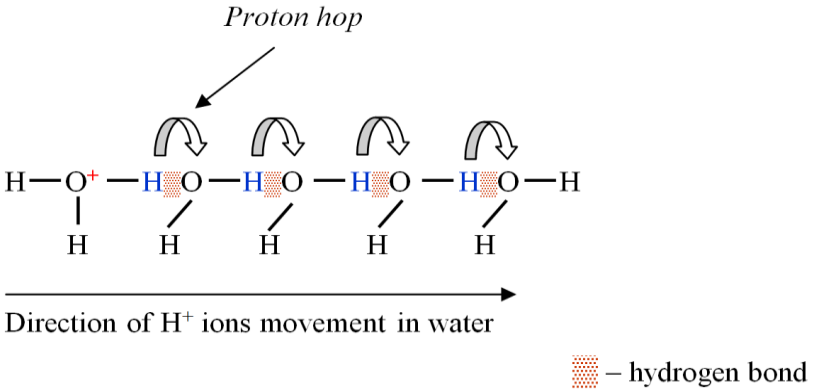

Fig. 1.5. The illustration of proton conductivity phenomenon.

When analyzing the proton conductivity in terms of defect reactions we could say that the excess proton (or proton defect) migrates through hydrogen bond network and each oxygen atom within it receives and consigns a particular hydrogen atom. Each hop (or pass) of proton is consequented upon the reorientation of a water molecule in order to restore the initial structure. That reorientation of a water molecule and proton hoping times are similar – both of about 1-2 ps of magnitude, and the hopping length is of 2.5 Å (similar to glass phase values) [393]. The process of proton hoping is incoherent and the actual proton motion highly exceeds the solvent reorganization rate.

Similarly the OH^- ion can move rapidly by analogous hopping mechanism in water with the same speed as H^+ ions, but in the opposite direction (towards the anode) than that of H^+ ion.

It was calculated that activation energy for proton conductivity is 10.9 kJ/mol [394]. The conduction at the moist surface of an electrolyte can also cause the proton conductivity, but it should be kept in mind that the cross-sectional area for surface conductivity pathway in most cases is much smaller than that of bulk one.

When some water in surrounding atmosphere is present and the sample is not completely exsiccated, the proton conductivity can come through in various metal diphosphates [395]. Shirai et al. [396] compared $A_{0.9}In_{0.1}P_2O_7$ (A=S, Ti) prepared through a solid state reaction route and H_3PO_4-modified $A_{0.9}In_{0.1}P_{2.4}O_7$ (A=S, Ti) synthesized by planetary-ball milling. While the first compound showed very low ionic conductivity of less than 10^{-7} S/cm at 400 °C, the second one showed very high proton conductivity of $2.0 \cdot 10^{-1}$ S/cm at 161 °C. It was demonstrated that H_3PO_4-modification lead to the case when almost insulating materials were transformed into highly proton conducting electrolytes of a non-conductive core-shell structure based on the diphosphate particles (core) and conductive amorphous/crystalline phosphorus oxide-based phase (shell).

2. EXPERIMENTAL METHODOLOGY

2.1 Synthesis of Li^+ and Na^+ solid electrolytes

The powders used for fabricating of samples were prepared by using the solid state reaction method which is known as economic, efficient and easy scale up synthesis way [191]. The starting materials (precursors) used for synthesis were of a solid phase. All the primary materials were mixed with alcohol and the obtained emulsions were milled in a planetary miller. Several milling and heating stages were used in order to obtain as good as possible contact for reaction of materials involved. The technological consecutions of the solid state reaction are represented in Fig. 2.1 – Fig. 2.8 for each group of materials investigated.

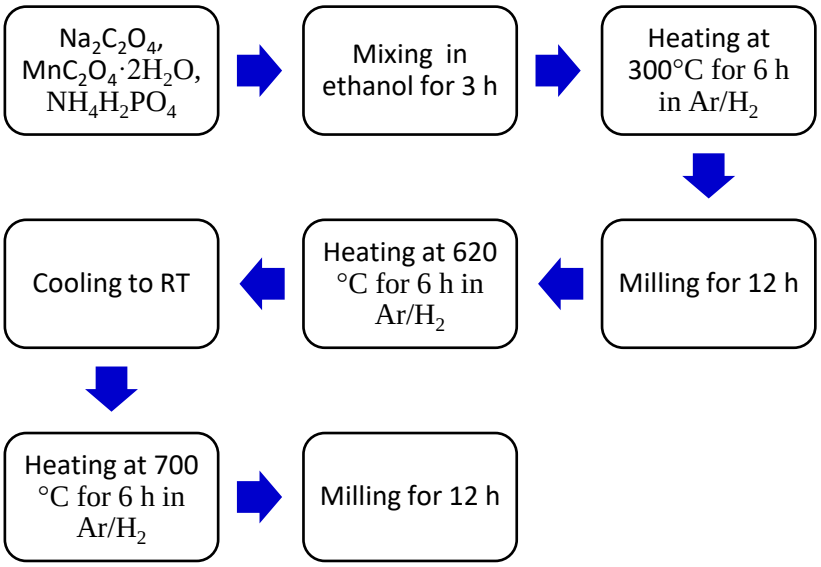

Fig. 2.1. The synthesis schema of $Na_2MnP_2O_7$ compound by solid state reaction method.

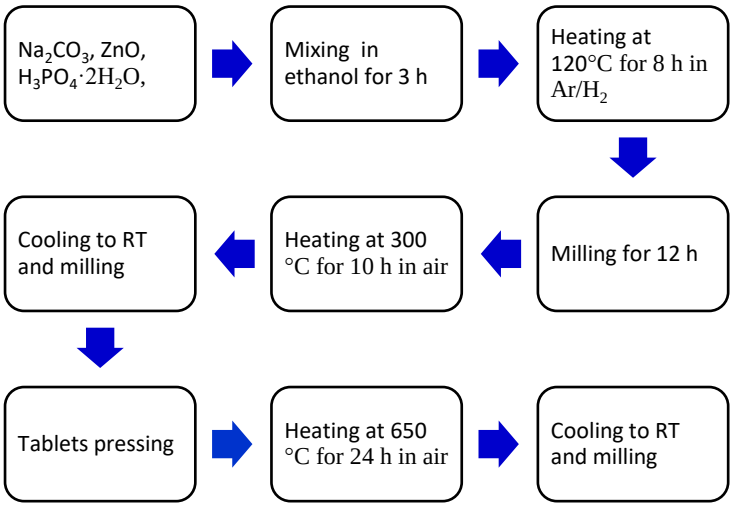

Fig. 2.2. The synthesis schema of $Na_2ZnP_2O_7$ compound by solid state reaction method.

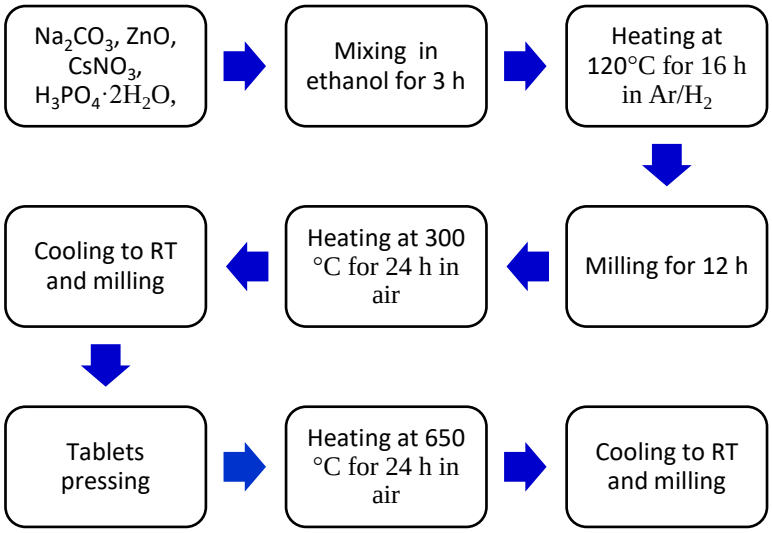

Fig. 2.3. The synthesis schema of $NaCsZnP_2O_7$ compound by solid state reaction method.

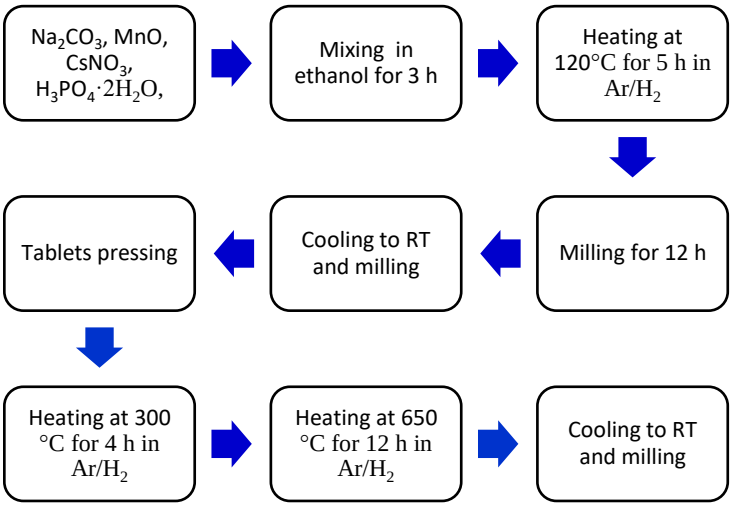

Fig. 2.4. The synthesis schema of $NaCsMnP_2O_7$ compound by solid state reaction method.

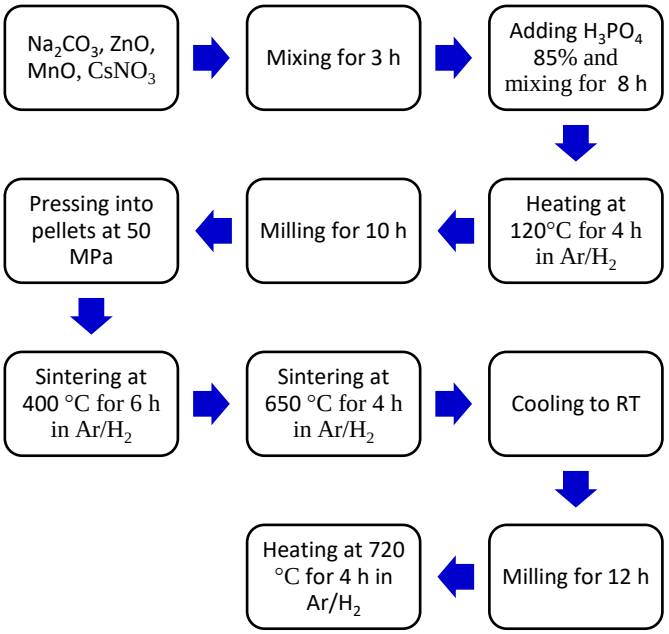

Fig. 2.5. The synthesis schema of $NaCsZn_{0.5}Mn_{0.5}P_2O_7$ compound by solid state reaction method.

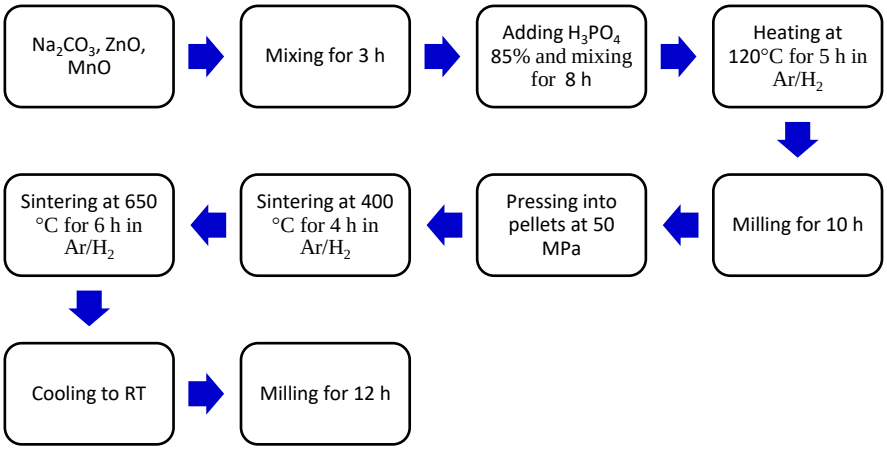

Fig. 2.6. The synthesis schema of $Na_2Zn_{0.5}Mn_{0.5}P_2O_7$ compound by solid state reaction method.

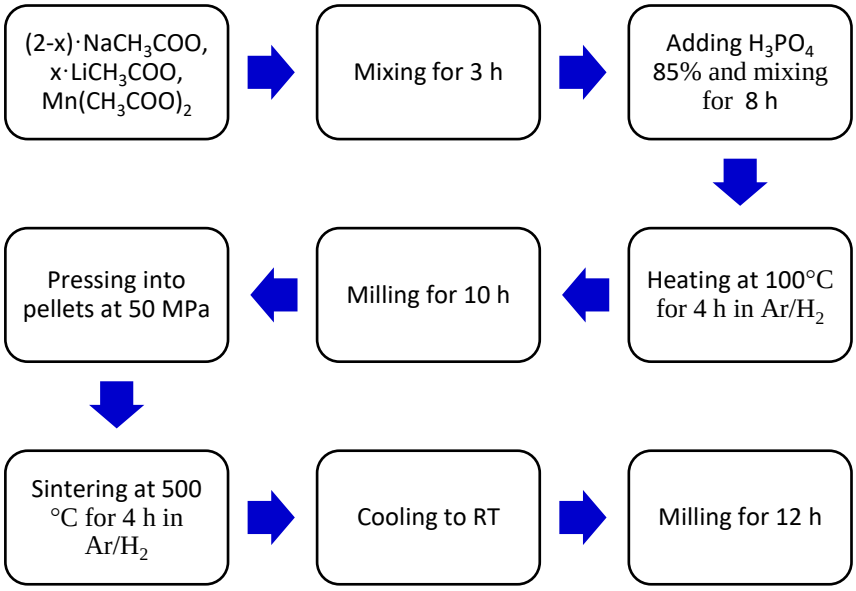

Fig. 2.7. The synthesis schema of other $Na_{2-x}Li_xMnP_2O_7$ compounds by solid state reaction method.

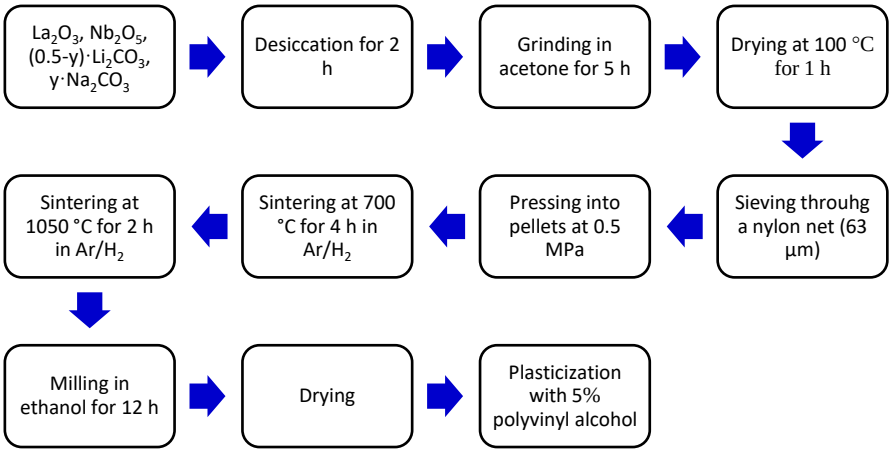

Fig. 2.8. The synthesis schema of $Li_{0.5-y}Na_yLa_{0.5}Nb_2O_6$ compounds by solid state reaction method.

2.2 Fabrication technology of solid electrolyte ceramics

All the ceramic samples were prepared from powder obtained by the solid state reaction method. The procedure of the fabrication of the samples was as follows. The first stage was the uniaxial compression of powder by 200-300 MPa pressure in ambient atmosphere. The manual hydraulic press (see Fig. 2.9a) of the brand *Specac* was used. The press-forms used were of 5 and 8 mm in diameter. The obtained cylindrical pellets were in the range of 2-4 mm of height. The obtained densities were from 60% to 80% of theoretical values. These values are mostly dependent on the nature of a material, while both the applied overpressure and (or) the pressing duration do not significantly influence the density values. The densities of the pellets were evaluated by measuring the mass and the geometrical parameters of each sample. After the synthesis pellets always assume higher density values (from 70% to 95% of theoretical values) and usually become much harder while, for comparison, only just compressed ones are fragile. The synthesis temperature is peculiar for an individual material and generally is obtained from dilatometric measurements. As a rule the most suitable temperature is only fractionally lower than a melting point of a considering material.

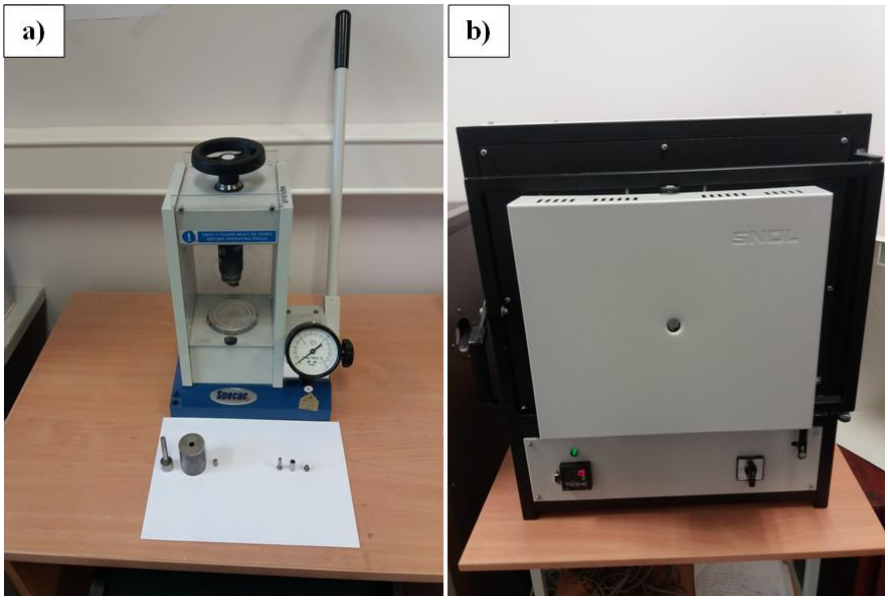

Fig. 2.9. The photographs of devices for ceramics preparation: manual hydraulic press and press-forms a) and the furnace for ceramics sintering b).

The sintering consists of two particular firing stages: heating at 400 °C temperature and heating at higher certain (sintering) temperature, subject to individual material as discussed above. The heating rate of a sample is adjustable via the interface of a programmable furnace *SNOL 7,2/1300* (see Fig. 2.9b) and was set to 3 K/min. The cooling rate is determined by the natural cooling of the furnace at ambient air and is varying. The lower temperature of a sample, the slower the rate of cooling as follows from the Newton's law of cooling. Generally, the cooling rate is noticeably lower than heating one. The schema of ceramics sintering in the furnace is showed in Fig. 2.10.

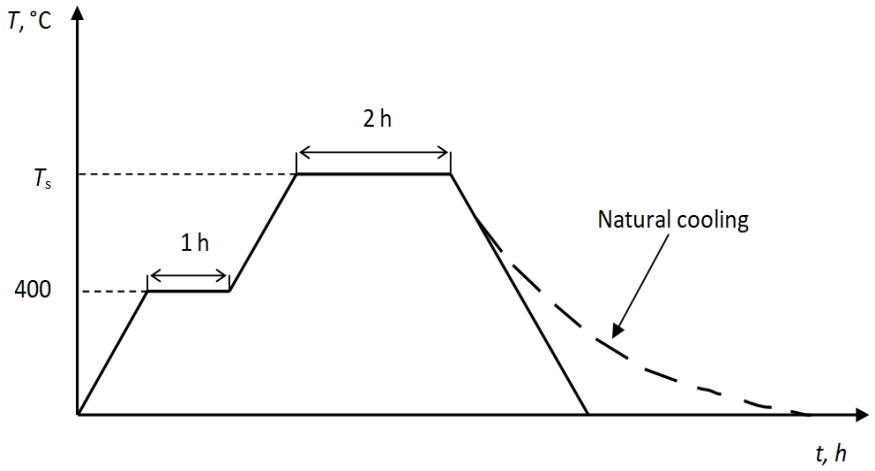

Fig. 2.10. The representation of the sintering process of ceramics.

The samples were prepared manually forming the cylindrical samples by using various knives for cutting and files for abrading and smoothing them. Before applying the electrodes the samples were immersed in a phial with acetone and bathed in a digital ultrasonic cleaner *Velleman VTUSC3* for about 5 minutes. The electrodes were formed by spreading the platinum, gold or silver paste on both sides of the cylindrical samples (see Fig. 2.11a) and successive annealing of the electrodes at 800 °C for Pt and Au type electrodes and at 400 °C for Ag type ones. The annealing duration at the highest temperature point was 15 minutes in all cases. If the four-probe measurements were carried out, the samples were of the rectangular shape (see Fig. 2.11b) and the conductive gold paste was used for the "voltage" contacts. The forming quality of the electrodes was controlled by the microscope *Leica E24D*. The representation of the sintering temperatures and durations is listed in Table 2.1.

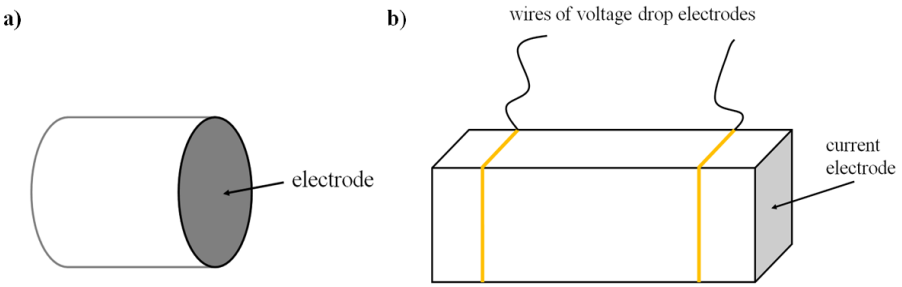

Fig. 2.11. Samples' geometry for impedance spectroscopy measurements: for two-probe method a) and for four-probe method b).

Table 2.1. The representation of the ceramics preparation conditions and the obtained densities.

Compound	Pressure, MPa	Sintering temperature, °C	Melting point, °C	Density, kg/m³	Relative density, %	Electrodes
$Na_2MnP_2O_7$	250	650	700	2180	75	Pt, Au
$Na_{1.5}Li_{0.5}MnP_2O_7$	300	560	590	1720	-	Ag + Ni
$NaLiMnP_2O_7$	300	590	620	1855	78	Ag + Ni
$Na_{0.5}Li_{1.5}MnP_2O_7$	300	600	630	2245	-	Ag + Ni
$Li_2MnP_2O_7$	300	710	740	1720	-	Ag + Ni
$Na_2ZnP_2O_7$	250	750	780	2795	90	Pt
$NaCsMnP_2O_7$	250	730	750	2765	86	Pt
$NaCsZnP_2O_7$	200	750	780	3290	92	Pt
$Na_2Zn_{0.5}Mn_{0.5}P_2O_7$	250	680	710	2730	80	Pt
$NaCsZn_{0.5}Mn_{0.5}P_2O_7$	250	680	710	3080	80	Pt, Au
$Li_{0.5-y}Na_yLa_{0.5}Nb_2O_6$	200	1200	>1200	-	≈ 95	Pt, Au

2.3 Material characterization techniques

2.3.1 X-ray diffraction

X-ray diffraction (XRD) is a versatile, non-destructive method to analyze material properties such as structure, texture, phase composition and many more of crystalline and amorphous solid samples, powder samples or even liquid samples. The method can be used both for the characterization of materials at their final stage and for the process control and optimization during the fabrication stage. The identifying of phases is automatically carrying by comparing XRD patterns obtained from an unknown sample with patterns of special reference database [397].

The structure of the solid electrolytes and the crystal lattice parameters were evaluated by using X-ray diffraction of both ceramic powders before sintering and pulverized ceramics after sintering. All XRD patterns presented in this thesis are obtained from pulverized ceramics if not indicated otherwise. Several X-ray difractometers were used for obtaining the diffractograms. All X-ray diffractometers were with Cu anode and $K_{\alpha 1}$ radiation was applied. Some experiments were done in ambient atmosphere while other ones in atmosphere of inert gasses (N_2 or Ar).

Thermal XRD analysis of $Na_2MnP_2O_7$ has been performed with a *Panalytical Xpert MPD* diffractometer equipped with *X'Celerator* detector

and an *Anton Paar HTK 12* furnace. The diagrams were recorded in 2θ range from 7 to 80° with a step of 0.017° and the duration of 100 s for each step.

Bruker D8 X-ray diffractometer equipped with a *MRI Physikalische Geräte GmbH TC-BASIC* heating chamber was used for XRD analysis of $Na_2Zn_{0.5}Mn_{0.5}P_2O_7$ in the range from room temperature to 330 °C. The diagrams were recorded in 2θ range from 10 to 60°. The scan rate for the pattern recording during heating was of 0.175 degrees per minute and during cooling of 0.25 degrees per minute. At room temperature and at the highest one it was 0.1 degrees per minute. XRD patterns were recorded with a 20 °C temperature step with heating and cooling rate of 10 °C/min when changing between two temperature levels. In order to achieve thermal equilibrium and completeness of the processes after reaching each temperature level, samples were kept at selected temperature for 60 or 20 min during heating and cooling respectively.

DRON-4-07 diffractometer was used for the analysis of $Li_{0.5-y}Na_yLa_{0.5}Nb_2O_6$ compounds. In order to study the high temperature-proof perovskite structure and its thermal evolution in detail at the temperature range from RT to 1200 K, high-resolution powder diffraction experiments have been performed at that experimental station in the synchrotron laboratory *HASYLAB* (Hamburg, Germany). The structural parameters at various temperatures were determined by the Rietveld full-profile analysis method by using XRD data.

Thermal X-ray powder diffraction of $NaLiMnP_2O_7$ has been performed at 40 °C, 200 °C, 300 °, 400 °C, 460 °C, 480 °C, 500 °C, 540 °C and 560 °C in Ar atmosphere with Cu Kα radiation on a *Panalytical Xpert MDP* diffractometer equipped with the *X'Celerator* detector and an *Anton Paar HTL 12* furnace. The diagrams were recorded in 2θ range from 10° to 80° with a step of 0.017° and 100 s per step.

All other X-ray diffraction patterns registered at room temperature were obtained by using *Brucker D8 Advance* equipment in the 2θ region from 10° to 70° with step degree 0.01-0.02°, 1-8 s time per step at inert gas atmosphere.

Analysis of the registered diffractograms were done by *TOPAS v.4.1* and *PDF4+* softwares.

2.3.2 X-ray photoelectron spectroscopy

X-ray photoelectron spectroscopy (XPS) is a powerful quantitative technique for the surface analysis of solid materials. By using this method

the information about the surface layer up to 20 nm can be obtained. XPS is useful for the determination of the surface chemical composition, identification of dopants or impurities, defining the chemical or electronic states of the particular elements and evaluation of the surface inhomogenities [398].

All XPS measurements for the ceramic samples were performed on an upgraded Vacuum Generator (VG) *ESCALAB MkII* spectrometer fitted with a new *XR4* twin anode. The non-monochromatised Al Kα X-ray source was operated at $h\nu$ = 1486.6 eV with 300 W power (20 mA/15 kV) and the pressure in the analysis chamber was lower than $5 \cdot 10^{-7}$ Pa during the spectra acquisition. The spectra were acquired with the electron analyzer pass energy of 20 eV for narrow scans and the resolution of 0.05 eV and with pass energy of 100 eV for survey spectra. All spectra were recorded at the 90° take-off angle and calibrated from the hydrocarbon contamination using the C 1s peak at 284.6 eV. Before the XPS measurements the surface was etched by argon in order to observe the surface state of the sample. Ar^+ ion beam sputtering was performed in the preparation chamber using 2 keV Ar^+ ions bombardment with a beam current density of 20 μA cm^{-2} for a duration of 30, 90 and 390 s. Spectra calibration, processing and fitting routines were done using the *AVANTAGE* software (5.962) provided by *Thermo VG Scientific*. Core level peaks were analyzed using a nonlinear Shirley-type background, and the calculation of the elemental composition was performed on the basis of Scofield's relative sensitivity factors.

2.3.3 Scanning electron microscopy and energy dispersive X-ray analysis

Scanning electron microscopy (SEM) and energy dispersive X-ray (EDX) spectroscopy was used for the analysis of the chemical composition of investigated ceramic samples and powder. Both techniques are integrated in *Hitachi TM3000* equipment, which was used for the analysis. An accelerating voltage of 15 kV was set to both SEM and EDX measurements. SEM image was taken by automatic image data acquisition by high sensitivity four elements of *quad BSE* detector. *Silicon Drift* detector of 30 mm^2 detection area and 161 eV energy resolution was used for EDX analysis. The chemical composition of ceramics and SEM images were obtained after the measurements of electrical properties of the samples. Sintered pellets were broken and measurements were carried on the broken edge.

2.3.4 X-ray fluorescence spectroscopy

X-ray fluorescence (XRF) analysis was performed using a *WDXRF* spectrometer *S4 Pioneer* (*Bruker AXS*), equipped with an Rh target X-ray tube (60 kV, 60 mA). The LiF crystal and gas flow (mixture of Ar^+ 10% CH_4) were used. The spectral data were processed with the *Spectra Plus* software of the *S4* device. The element concentrations after the calibration of *S4* equipment were calculated automatically.

2.3.5 Differential thermal, thermogravimetric and differential scanning calorimetry analysis

Differential thermal analysis (DTA) is very useful technique for determining either endothermic or exothermic changes relative to an inert reference. Transformations or any changes in phase transition, melting or sublimation can be detected. The differential temperature is plotted versus the temperature or time [399].

The thermogravimetric analysis (TGA) is a technique of thermal analysis for the measurements of mass of a sample as a function of temperature. This method is relevant for the physical phenomena such as absorption, adsorption, desorption, phase transition and also for the chemical phenomena such as chemisorptions or solid-gas reactions [400]. Nowadays, DTA and TGA analysis apparatus usually are incorporated in the same equipment with DSC – differential scanning calorimetry.

Two different DTA/TGA apparatus were used for the measurements. *SDT Q600* apparatus was employed for the $Na_{2-x}Li_xMnP_2O_7$ compounds investigation on heating and cooling the powder from room temperature to 620 °C with 10 K/min heating/cooling rate for $Na_2MnP_2O_7$ compound and from room temperature to 580 °C with the same rate for $NaLiMnP_2O_7$ compound. *Netzsch STA 409 PC Luxx* setup was employed for the investigation of $NaCsZn_{0.5}Mn_{0.5}P_2O_7$. The analysis was done in Ar gas (99.999%) atmosphere (*Linde Gaz Polska*). The flow rate of argon was 60 cm^3/min.

2.3.6 Impedance spectroscopy

General disquisitions

Impedance spectroscopy (IS) is a powerful technique for the analysis of the frequency dependent electrical properties of electrochemical systems within it several different simultaneous processes can occur. That technique

has been widely used for evaluation of the electrochemical behaviour of electrode and (or) electrolyte materials and the response is analyzed upon an alternating voltage of low value at fixed frequency and that voltage varies over a wide frequency range (up to nine orders). The setup of the IS technique apparatus can be specialized for either two or four probes measurements [401, 402]. The latter method is actual when elimination of the electrode polarization effect is needed.

The impedance or complex electrical resistance from the electrochemical system is related to the ability of the analyzing circuit elements to resist the electrical current and as follows from Ohm's law is defined by the ratio between a sinusoidal alternating voltage $V(t)$ and the output current response $I(t)$ which is also time dependent [403]:

$$\tilde{Z}(t) = \frac{V(t)}{I(t)}, \tag{2.1}$$

where $V(t) = V_0 \sin \omega t$ and $I(t) = I_0 \sin(\omega t + \varphi)$, and φ is the phase angle between the voltage and current vectors. The specific impedance can be given as follows:

$$\tilde{z} = \tilde{\rho} = \tilde{Z}\frac{S}{l}, \tag{2.2}$$

where S is an electrode area and l is sample length.

The complex impedance can be given as follows:

$$\tilde{Z} = Z' - iZ'', \tag{2.3}$$

where Z' represents the real part of the impedance (or simply pure resistance R) and Z'' represents the imaginary part.

Electrical impedance can be simply plotted in a complex plain as a planar vector (see Fig. 2.12).

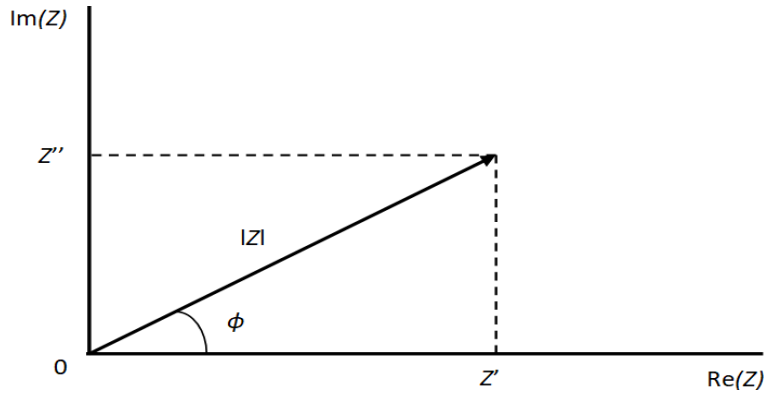

Fig. 2.12. Electrical impedance plotted as a planar vector. Adapted from [401].

While the conductivity σ (or resistivity) and dielectric permittivity ε are two fundamental parameters (which can be measured as a functions of time, temperature and AC radial frequency ω) to characterize the abilities of the analyzed material to store electrical energy and to transfer electric charge, the material polarization density is time dependent and can be written as follows [403]:

$$P(t) = (\varepsilon' - 1)\varepsilon_0 E(t), \tag{2.4}$$

where ε_0 is the electric constant and E is the electrical field.

The polarization of different entities (grains, grain boundaries and interfaces between electrodes and electrolyte) is frequency dependent. The complex permittivity $\tilde{\varepsilon}$, represented by its real and imaginary components, is a function of two parameters. One is real permittivity (either simply "permittivity" or "dielectric constant") and the other is imaginary permittivity related to heat losses within the system. The dielectric loss is nothing short of the heat loss due to dipole rearrangements and possible leakage currents within the material. The complex permittivity can be represented as [403]:

$$\tilde{\varepsilon} = \varepsilon' - i\varepsilon''. \tag{2.5}$$

Analogously, specific complex admittance $\tilde{\sigma}$ and electric modulus $\tilde{m}$ can be expressed:

$$\tilde{\sigma} = \sigma' + i\sigma'' = \frac{1}{\tilde{\rho}}, \tag{2.6}$$

$$\tilde{m} = m' + im'' = \frac{1}{\tilde{\varepsilon}}. \tag{2.7}$$

The complex conductivity and complex dielectric permittivity are related as follows:

$$\tilde{\sigma} = i\omega\varepsilon_0\tilde{\varepsilon}. \tag{2.8}$$

While the broadband IS overcome the frequency range from 10^{-6} Hz to 10^{12} Hz [404], several polarization mechanisms can occur in a material. The mechanism or type of polarization is frequency dependent. At the highest frequencies (over 10^{13} Hz) the electronic polarization in point of atom nucleus can occur; at the frequency range from 10^{9} to 10^{13} Hz the ionic polarization can occur in solid ionic materials (e. g. NaCl). Below 10^{9} Hz the orientational polarization can be observed in materials which consist of dipoles and have a net permanent dipole moment (e. g. H_2O). At grain boundaries or electrode material interfaces an interfacial polarization can occur. This type of polarization is also called space charge or Maxwell-Wagner-Silars polarization. If the polarization occurs between the material and charge carriers blocking electrode it is more specifically called electrode

polarization. Since the grain boundary polarization can actually be evidenced at the frequencies up to 10^7 Hz the electrode polarization comes into play only at frequencies below 10^5 Hz [404].

Solid electrolytes can be represented by equivalent circuits, which were first time proposed for yttrium stabilized ZrO_2 ceramics with Pt electrodes by Bauerle in 1969 [405]. Three processes (electrode polarization, polarization in grain boundaries and grains) were evidenced from complex admittance schema and represented by the equivalent circuit (see Fig. 2.13) which is typical for most solid electrolytes [401].

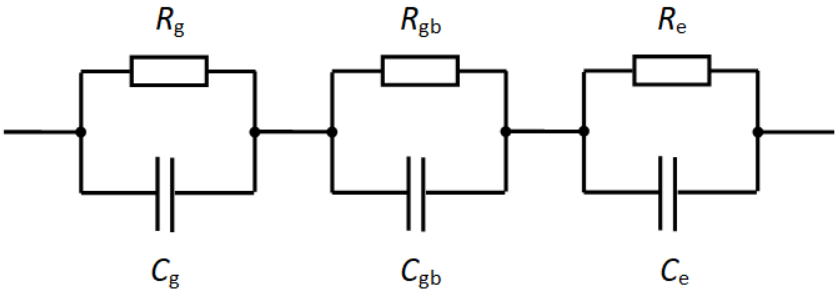

Fig. 2.13. Bauerle representation of an equivalent circuit of a solid electrolyte.

The equivalent circuit of an ideal electrochemical system consists of resistors and capacitors as showed in Fig. 2.13. Each pair of resistor and capacitor represents the certain phenomenon or type of polarization as discussed above. The lower index "g" denotes grains, "gb" – grain boundaries and "e" – electrodes. The capacitance C and resistance R are connected in parallel to each other. The product of both parameters is given as "time constant" $\tau = RC$ and describes the dielectric relaxation time [326]. R and C connected in parallel are represented by semicircles in complex plane (see Fig. 2.14). The centres of these semicircles overlie the Re(Z) axis in complex impedance plane. The increase of an external electric field frequency is denoted by arrows. These two semicircles are evident only if grain conductivity is much higher than that of grain boundaries and the capacitance of the grain boundaries phase is bigger than that of grains $R_g C_g \ll R_{gb} C_{gb}$ [406].

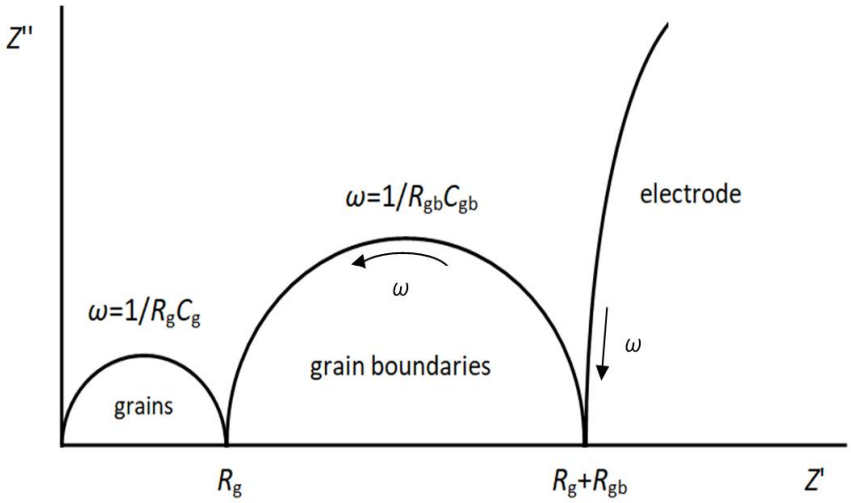

Fig. 2.14. Idealized frequency response of a superionic ceramics with ion blocking electrodes in a complex impedance plane. Adapted from [326].

However, two separate semicircles of an ideal form are very rare in real materials. The depressed or even deformed semicircle is more common for the impedance spectra of solid electrolytes. That depression is due to similar relaxation times of two or more different processes. The criterion of that similarity is the difference of the relaxation times of rival processes less than two orders. When several relaxation times of similar value are given we have the so called "distributed relaxation time" phenomenon and the centre of a semicircle does not lie on a Re(Z') axis in a complex impedance plane, thus the equivalent circuit of that system cannot be simulated by simple R and C elements and more sophisticated distributed elements are introduced such as CPE – constant phase element [401].

Spectrometers used in experiments

Three different impedance spectrometers masterminded and constructed by prof. A. Kezionis group have been used for the measurements: one for high frequency measurements, another for low frequency measurements and the third (combining, covering and surpassing two last-mentioned equipments) for broadband frequency range.

The spectrometer of high frequency range (300 MHz – 3 GHz) is based on *Agilent E5062A* analyzer and essentially is the improved version of a spectrometer reported in an earlier work [407]. The coaxial waveguide line is separated into two rods which are tailored to hold a cylindrical sample inserted between two ends of inner conductor. The scattering S-parameters

matrix of the line is measured versus frequency and temperature. DC power supply and electronic thermometer are used for temperature control. Software developed on *Matlab* environment has a graphical user interface. A coaxial refractory waveguide is made of $3Al_2O_3$-$2SiO_2$ (mullite) ceramics with low thermal expansion ($5 \cdot 10^{-6}$ K^{-1}) and covered with platinum paste [408]. Low thermal expansion of a waveguide capacitates to avoid significant systematic errors related to unequal thermal expansion of the sample and waveguide and therefore the maximum temperature of about 900 °C can be achieved in measurements. The diameter of a sample is limited up to 3 mm, the length is limited up to 1.5 mm [408] and the size of the sample holder is much smaller than that for other impedance spectrometers previously reported in literature by other groups [409-413].

Four-electrode impedance spectrometers are used for low frequency investigation of samples with ion blocking electrodes. In order to avoid the effect at the sample-electrode interface the two voltage measurement electrodes are placed in the bulk of sample. The current measurement electrodes (likewise in the high frequency technique) remain on the terminals of a cylindrical sample. The equipment used in experiments for this dissertation is the third generation of four-electrode impedance spectrometer made by A. Kezionis group [414], two previous spectrometers were introduced in the past [415, 416]. The new four-electrode impedance spectrometer can operate in the frequency range from 10 Hz to 2 MHz by engaging two or four electrodes with the sample temperature range from 300 K to 800 K. The differential amplifier with extremely high input impedance and common mode rejection ratio over a wide frequency range was constructed and implemented for the four-electrode measurement mode [414]. A computer with software developed in *Matlab* environment is used for the controlling the operation of the spectrometer. *TiePie Handyscope HS3-50* instrument is used for signal generation and voltage determination. The current to voltage (I-V) converter is used for measuring the current through a sample. The first channel of the oscilloscope (CH1) is fed by the latter converter. The second channel (CH2) is fed by the amplifier through the switch S. In two-electrode measurements the buffer's output is connected to CH2 input of the oscilloscope. The temperature in the sample holder is controlled by digital thermometer *Amprobe TMD90A* and power supply for the heater is controlled by the computer [414]. While the platinum paste is commonly used for the current electrodes, the gold paste is mostly used for

affixing the voltage drop terminals. The sample under analysis has oblong rectangular shape.

The ultra-broadband impedance spectrometer, constructed and reported in detail by A. Kezionis group [417, 418] is very advantageous for electrical characterization of solid electrolytes. Its principal schema is represented in Fig. 2.15a and its photograph is shown in Fig. 2.15b. That ultra-broadband range comprehends the frequency values from 100 mHz to 10 GHz and is much more accurate than the previous high frequency impedance spectrometer apparatus [408]. The prime advantage of the new spectrometer is the fact that influence of the transmission line's thermal expansion was dramatically reduced, which is crucial at high temperatures, and another major achievement is that the parasitic reflections of the sample holding system were successfully taken into account, which is crucial in the gigahertz frequency range [418]. Furthermore, the distribution of the electromagnetic field in the measuring capacitor is taken into account. The technique of full two-port scattering matrices of the short circuited line (one line with a calibration sample and the second one with the sample to be measured interposed) was used instead of solving very complicated electrodynamics problems [419, 420]. The spectrometer has a telescopic coaxial transmission line and a sample can be placed in the gap of the central conductor. A refractory ceramics coated with Pt layer was used for the waveguide and therefore is oxidation-proof up to 1000 °C. The high-temperature chamber was reduced to few centimetres in length due to low thermal conductivity of ceramics used for the waveguide [418]. The software of the spectrometer is developed in *Matlab* environment and provides a graphical user interface. The extremely broad operating frequency range was achieved alternatively connecting a sample from high frequency to low frequency measurement system [417]. *Agilent E5071A* network analyzer in pair with *N4691B* electronic calibrator is used for high frequency sample circuit, and *Agilent 87222* microwave switches are used to activate the low frequency measurement system consisting of computer oscilloscope, a vector current-voltage converter and a waveform generator *Agilent 33521*. While the low frequency system is responsible for the measurement range from 100 mHz to 2 MHz, the high frequency system is responsible for the measurement range from 2 MHz to 10 GHz. The temperature in the sample holder is controlled by *E3634C* power source and *Amprobe TMD90A* thermometer [417].

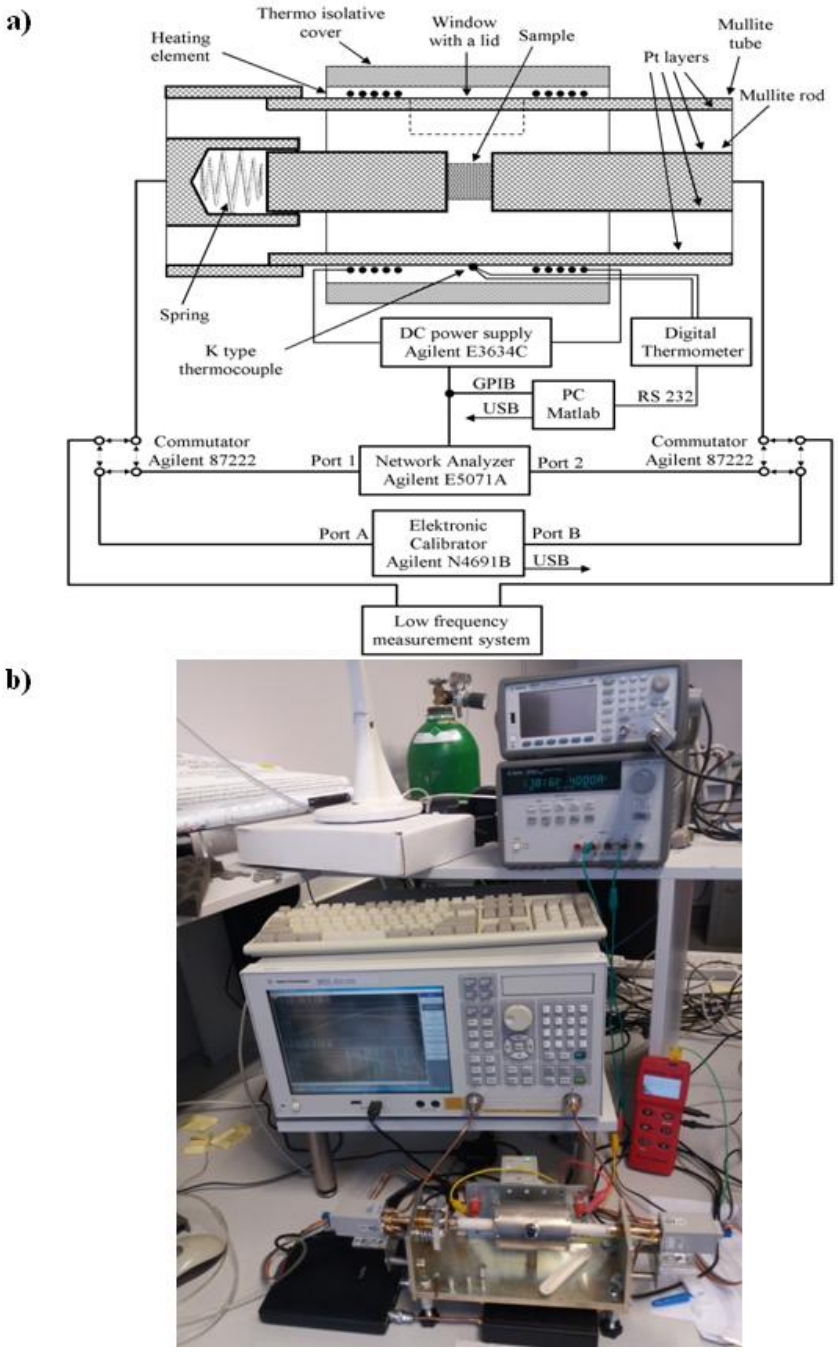

Fig. 2.15. The principal scheme of the ultra-broadband impedance spectrometer [417] a) and its photograph b).

Impedance measuring circumstances

Impedance spectroscopy of the sintered $Na_2MnP_2O_7$, $Na_2ZnP_2O_7$, $NaCsMnP_2O_7$ and $NaCsZnP_2O_7$ ceramics was performed in the frequency range of 10 Hz – 10 GHz and in the temperature range of 300-800 K. Pt paste was applied and fired on the surfaces of cylindrical samples. Most of the impedance measurements were performed in ambient air atmosphere, but in order to clarify the influence of humidity to the electrical properties of $Na_2MnP_2O_7$ ceramics the synthetic air containing < 3 ppm of water was used and impedance was measured from 1 to 10^6 Hz with a Frequency Response Analyzer (*Solartron 1260*) combined with Dielectric Interface (*Solartron 1296*).

The measurements of electrical properties of $Na_2Zn_{0.5}Mn_{0.5}P_2O_7$ ceramic samples in low frequency range (10 Hz – 2 MHz) were carried out by two probe method. The electrodes were fired at 920 K on the sintered cylindrical samples by applying conductive Pt paste (*Gwent Electronics Materials Ltd*.). The measurements in the microwave range ($3\cdot10^5$-$3\cdot10^9$) Hz were performed by *Agilent Network Analyzer E5062A* connected to the coaxial line, the part of inner conductor of coaxial line was replaced by the sample. The impedance of the sample was calculated from scattering parameters of such network as in [408]. The temperature was changed in the range 300-700 K during impedance spectroscopy experiments in the low and high frequency ranges and measured using *Digital Thermometer TMD90A*. The temperature was controlled by a computer connected to a DC power supply.

The measurements of electrical properties of $NaCsZn_{0.5}Mn_{0.5}P_2O_7$ ceramic samples in the low frequency range (10 Hz – 2 MHz) were carried out by the two probe method. The electrodes were fired at 920 K on the sintered cylindrical samples by applying conductive Pt paste (*Gwent Electronics Materials Ltd*.). The measurements in the microwave range ($3\cdot10^5$ – $3\cdot10^9$) Hz were performed by *Agilent Network Analyzer E5062A* connected to the coaxial line, the part of inner conductor of coaxial line was replaced by the sample. The temperature measurements of the ceramics in the low and high frequency ranges were performed in the range 300–700 K using *Digital Thermometer TMD90A*. The temperature was controlled by a computer connected to a DC power supply.

The impedance spectroscopy of $Li_{0.5-y}Na_yLa_{0.5}Nb_2O_6$ was performed on small cylindrical ceramic samples. Platinum paste was used to prepare electrodes. The length of all samples was 1.5 mm and the electrode surface

area was under 1 mm^2. Impedances (~Z) were measured in the frequency range of 10 Hz to 10 GHz and temperature range from 300 to 800 K with 20 K step. In order to avoid any affects due to processes on the interface of the Pt electrode and $Li_{0.5-y}Na_yLa_{0.5}Nb_2O_6$ electrolyte additional measurements by four electrode method were performed. We further used intrinsic materials parameters to describe our ceramics. The impedance data were fitted using equivalent circuit models by *ZView* software.

For the electrical investigations of $Na_{1.5}Li_{0.5}MnP_2O_7$, $NaLiMnP_2O_7$, $Na_{0.5}Li_{1.5}MnP_2O_7$ and $Li_2MnP_2O_7$ ceramics the powder were pressed and samples were sintered at various temperatures in interval 560-710 °C for 2 h in air. Impedance spectroscopy of the sintered $NaLiMnP_2O_7$ ceramics was performed in the frequency range from 10 Hz to10 GHz and in the temperature range from 300 K to 800 K or 825 K in ambient air atmosphere. Ni plates were affixed with Ag paste on both sides of the cylindrical sample and that sample with the electrodes was gradually heated up to 400 °C and fired at that temperature for 15 min. The paste types used for the samples are pointed out in Table 2.1 together with the sintering parameters.

3. RESULTS AND DISCUSSIONS

3.1 Investigation of various pyrophosphates

3.1.1 Phase transition in $Na_2MnP_2O_7$

The detail investigation of $Na_2MnP_2O_7$ conductivity parameters was performed. The impedances of $Na_2MnP_2O_7$ ceramics measured at different frequencies and at different temperatures are represented in complex plane plots in Fig. 3.1.

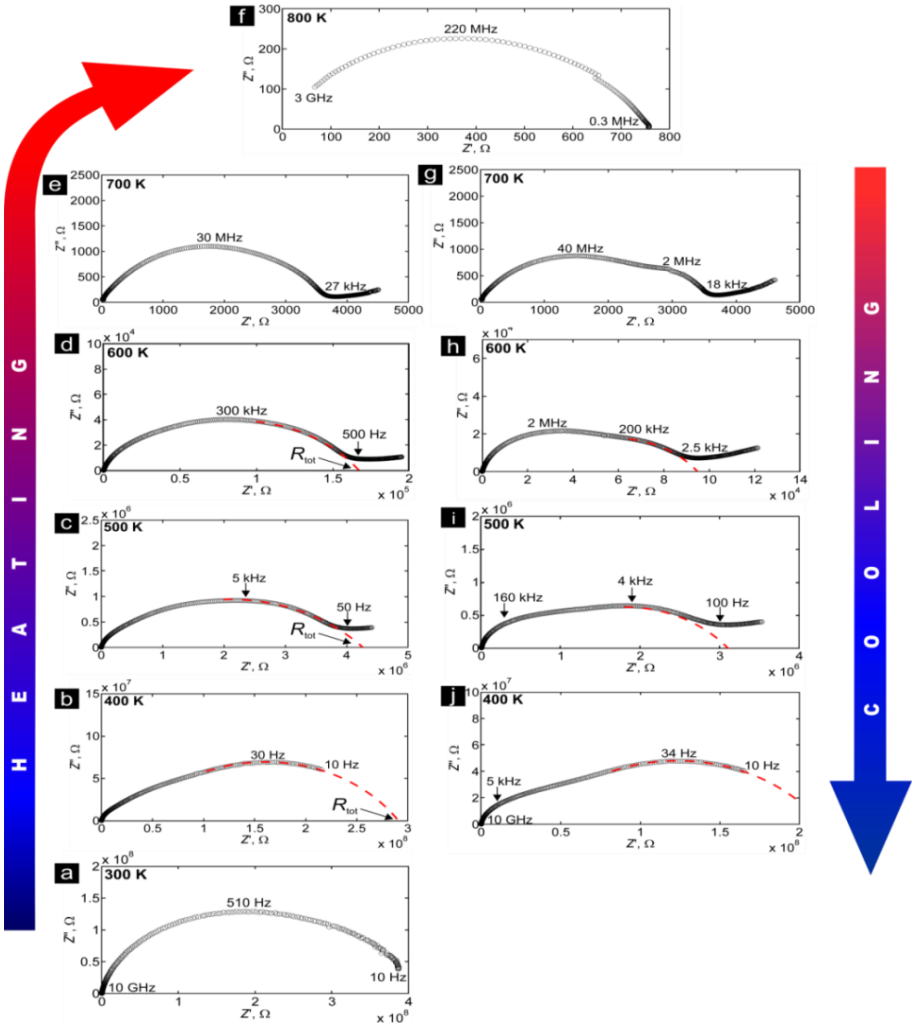

Fig. 3.1. Impedance complex plane plots of $Na_2MnP_2O_7$ ceramics measured during heating and cooling stages. Some characteristic frequencies are indicated, red dashed lines show extrapolation to total resistance.

The extrapolation to total resistance (showed in some graphs by red dashed lines) was performed by *ZView2* program which calculates the value of the real part of impedance from the incomplete (fragmentary) complex impedance graph automatically when the suitable equivalent circuit model is fitted.

In our case only one maximum of the impedance imaginary part can be observed. However, at least two processes contribute to the spectra, which can be related to ion transport in grains and grain boundaries of the ceramic sample. Very close relaxation times of ions in ceramic grains and grain boundaries and unknown distribution of relaxation times makes it too difficult, if at all possible, to separate these two processes from each other. So only the total resistance $R_{\mathrm{tot}} = R_{\mathrm{g}} + R_{\mathrm{gb}}$ has been found from Z″(Z′) plots by extrapolating the lower frequency semicircle to the Z′ axis as it is shown by red dashed lines in Fig. 3.1. Two processes are even more pronounced during the cooling stage (Fig. 3.1f–j), but the total resistance remains in the same order as the one measured during heating (Fig. 3.1a–f). σ_{tot} is plotted versus reciprocal temperature in Fig. 3.2.

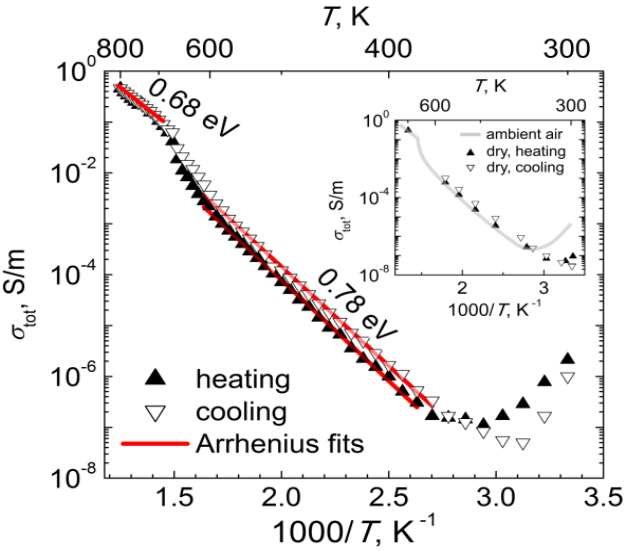

Fig. 3.2. Arrhenius plot of the total conductivity of $Na_2MnP_2O_7$ ceramics measured in ambient atmosphere. Red solid lines are the fittings to the Arrhenius equation. The insert shows the results obtained when impedance was measured in dry synthetic air. The increase of the conductivity at 660-680 K temperature was associated with the phase transition taking place in the ceramics.

For $Na_2MnP_2O_7$ two anomalies can be distinguished from $\sigma_{\mathrm{tot}}(1/T)$ graph (Fig. 3.2). The first one at 660-680 K shows a step-like increase of

conductivity by about 5 times on heating and similar decrease on cooling (type b from Fig. 1.4). Most probably this anomaly indicates a phase transition taking place in this material. The activation energy of the conductivity before this transition is 0.78 eV and decreases to 0.68 eV at temperature > 680 K.

From the temperature dependences of the real part of conductivity and the real part of dielectric permittivity (Fig. 3.3a and Fig. 3.3b) one can see the step-like increase/decrease of both quantities at 660-670 K and the temperature point of these changes is frequency independent. This result supports the phase transition hypothesis.

The differential thermal analysis also showed an endothermic peak at 663 K when heating the sample and the exothermic peak on cooling (Fig. 3.3c), which shows that the phase transition is reversible. The phase transition onset temperature is in very good agreement with electrical conductivity measurements.

Finally, the phase change was proved by thermal XRD. At 30 °C XRD showed the triclinic symmetry of the compound (space group P1), identical to the one obtained by P. Barpanda et al. [5]. Its lattice constants are a = 9.907(1) Å, b = 11.110(1) Å, c = 12.520(1) Å, α = 148.461(3)°, β = 122.024(5)°, γ = 68.337(6)°. The lattice parameters of our synthesised compound are in good agreement with [314]. The profile refinement of the diagram evidenced the presence of some impurities, their identification using *PDF4+* database led to phases MnP_2O_6 and Na_2MnO_2 but other peaks remained unindexed. On thermal diffraction diagrams (Fig. 3.4), the evolution of intensities and positions of the peaks indicates a slow and progressive structural transition occurring between 300 °C and 500 °C. The changes in peak shapes and intensities associated with the structural changes of $Na_2MnP_2O_7$ phase were found at 2θ values of 16.5°, 29.5°, 31.8°, 32.0°, 32.8°, 33.0°, 33.3° and 33.5° and are indicated by arrows in Fig. 3.4. The diagram obtained at 500°C was not successfully indexed with phases referenced in *PDF4+* database while the poor quality of the data at high temperature prevents us from carrying out Rietveld refinement. However, the phase transition is evidenced from the raw XRD data (Fig. 3.4). This structural transition is reversible as the data recorded at room temperature after the thermal diffraction measurements are also indexed with the starting triclinic cell.

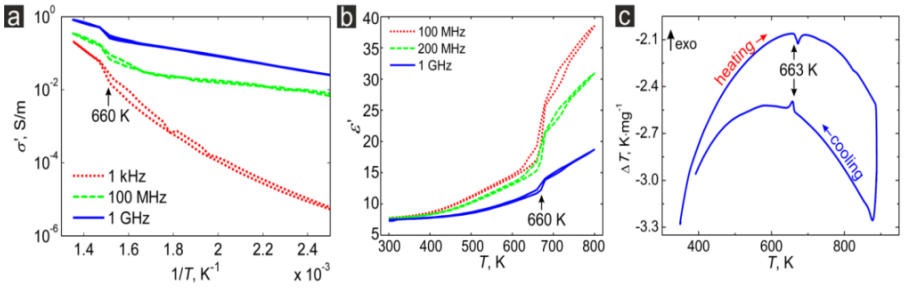

Fig. 3.3. Temperature dependences of the real part of conductivity in Arrhenius representation (a), the real part of dielectric permittivity (b) and differential thermal analysis (c), – all indicating phase transition in $Na_2MnP_2O_7$.

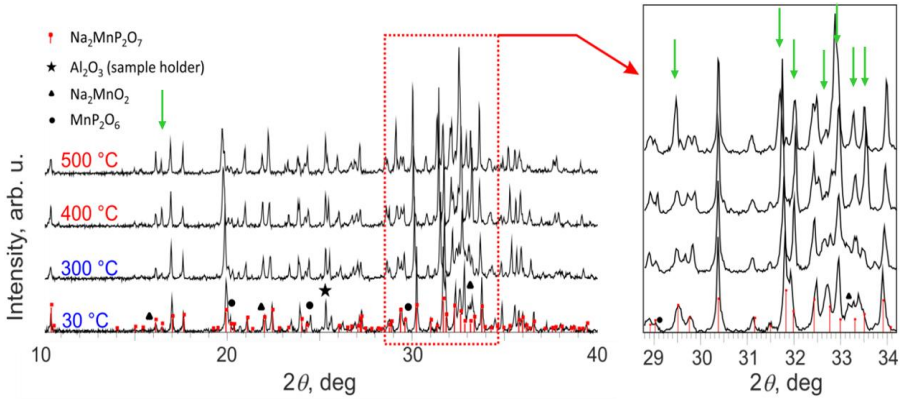

Fig. 3.4. Thermal X-ray diffraction patterns of $Na_2MnP_2O_7$ powder. Structural transition takes place in $Na_2MnP_2O_7$ phase. Magnified area at the right hand side shows a phase change above 390 °C. Arrows indicate the peaks which show phase transition of $Na_2MnP_2O_7$. Both Na_2MnO_2 and MnP_2O_6 are impurities. Alumina which was used as sample holder can also be seen in the diffractgram.

3.1.2 Mixed sodium-ion and proton conductivity in $Na_2MnP_2O_7$ compound

The second anomaly observed in Fig. 3.2 is of type e (see Fig. 1.4 for different types of electrical conductivity behaviour in ionic compounds). It shows an unexpected decrease of conductivity with increasing temperature from 300 K to about 370 K. Further heating leads to Arrhenius type change of electrical conductivity (ordinary type in Fig. 1.4) in the temperature range from 370 K to 660 K. On the cooling stage the conductivity does not follow the Arrhenius law from 370 K anymore and from 330 K it starts to increase when at 300 K it almost reaches the initial conductivity value.

Thermogravimetric analysis result is presented in Fig. 3.3c. A mass loss is observed when heating the sample which was associated to water

evaporation. The $Na_2MnP_2O_7$ powder was shown to contain only about 0.5 wt.% of water. Such a tiny amount of water seems to be sufficient to increase the room temperature total conductivity of $Na_2MnP_2O_7$ ceramics by almost two orders of magnitude.

The impedance measurements in dry synthetic air shows significantly reduced water influence on the total conductivity of $Na_2MnP_2O_7$ ceramics (insert of Fig. 3.2). After one hour of flushing dry air the total conductivity was significantly decreased at room temperature. Still on heating there is a minor decrease of the total conductivity and at temperatures above 350 K the conductivities obtained in ambient and dry air overlap. Moreover, on cooling we do not observe the increase of total conductivity in dry atmosphere even at room temperature. The measurements of impedance in dry air give us the evidence of the room temperature proton conductivity in $Na_2MnP_2O_7$.

The shape of impedance spectrum at 300 K measured in ambient air is different compared to the spectra obtained at higher temperatures (> 400 K). In the complex plain plot (Fig. 3.1a) we can hardly notice two relaxations for 300 K graph. The two processes still do exist, but they are connected in parallel to the low proton resistance. Consequently only one deformed semicircle can be distinguished and the relaxation frequency is shifted towards higher frequency range (510 Hz at 300 K as shown in Fig. 3.1a, compared to 30 Hz at 400 K – Fig. 3.1b. With the evaporation of water the proton conductivity disappears as well and Na^+-ion relaxation in grains and in grain boundaries of the ceramics is evidenced from impedance complex plane plots.

The temperature and frequency dependences of σ' are presented in Fig. 3.5a and Fig. 3.5b, respectively. The curves representing frequencies of 10 Hz, 10 kHz and 0.3 MHz are blending together at temperatures higher than 500 K. This shows that the frequency plateau is reached, and their separation at lower temperatures is showing the dispersion region. The low frequency conductivity plateau was associated with ionic conductivity in the grain boundaries of ceramics. The second plateau cannot be observed in any frequency range, because it is hidden by the grain boundary dispersion region.

In the frequency dependences of σ' curve crossing at about 0.3 MHz can be observed (Fig. 3.5b). At low frequencies the conductivity decreases with the temperature increase up to 370 K. At 0.3 MHz σ' is temperature independent up to 400 K. Such a behaviour is caused by two competing

processes, the one being relaxation dispersion, which increase the real part of conductivity with frequency and the other – water leaving the ceramic sample, which decrease the total conductivity. Besides, above 0.3 MHz we do not observe the decrease of conductivity with increasing temperature. This suggests that the temperature behaviour of $Na_2MnP_2O_7$ ceramics total conductivity is mostly affected by the ionic (sodium and proton) transport in grain boundaries, while the conductivity of the bulk is caused by sodium-ion transport only.

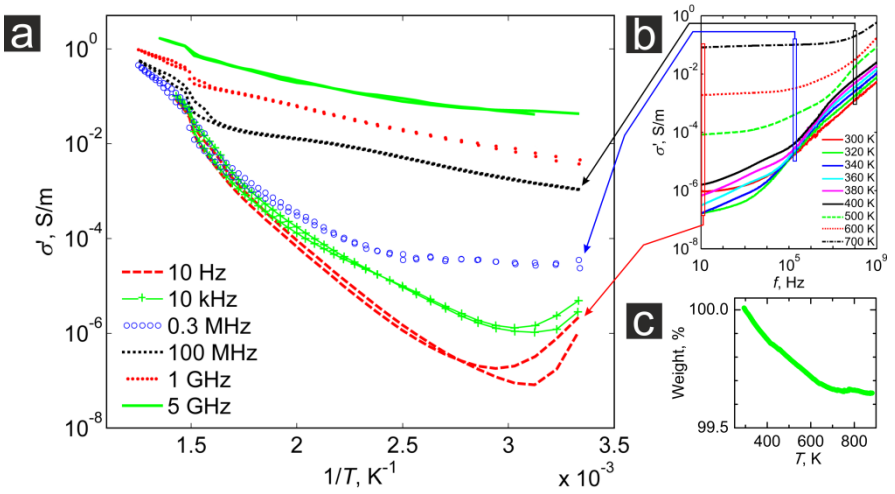

Fig. 3.5. Temperature dependences of the real part of conductivity at different frequencies (a), frequency dependences of the real part of conductivity at different temperatures of $Na_2MnP_2O_7$ ceramics (b) and thermogravimetry signal when heating $Na_2MnP_2O_7$ powder (c).

The conductivity of the high temperature phase was found to be stable, while for the low temperature phase (below phase transition, $T < 660$ K) we are measuring higher conductivity on cooling the sample compared to the one found on heating. We would exclude the water influence on the higher conductivity obtained during cooling stage, because the same effect was found both in humid ambient atmosphere and in dry synthetic air. The higher conductivity found during the cooling stage may be related to partially frozen high-temperature more conductive phase.

3.1.3 Structural changes of $Na_2Mn_3(P_2O_7)_2$ phase in $NaLiMnP_2O_7$ mixed phase compound

Crystalline structure

XRD measurements revealed that the investigated $NaLiMnP_2O_7$ compound consists of two phases: $Na_2Mn_3(P_2O_7)_2$ and $LiMnPO_4$. The first phase belongs to di-pyrophosphate compounds' family $Ag_2M_3(P_2O_7)_2$ (M = Co, Mn) and $Na_2Cd_3(P_2O_7)_2$. The latter two compounds were first reported by Bennazha et al. [421]. Liu et al. [422] investigated $Na_2Mn_{3-x}Fe_x(P_2O_7)_2$ ($0 \leq x \leq 2$) with the structure the same as one of $Ag_2M_3(P_2O_7)_2$ [421]. It was revealed that $Na_2Mn_3(P_2O_7)_2$ exhibits an electrochemical activity of 1.5-4.5 V vs. Na^+/Na and 3.8 V charge/discharge voltage plateau was demonstrated when employed as cathode material. Additionally, it was found that Fe substitution of Mn in $Na_2Mn_{3-x}Fe_x(P_2O_7)_2$ compounds can enhance the Na-ion diffusion by about two orders of magnitude with Fe doping content exceeding x = 0.5 [422].

We found that at 40 °C $Na_2Mn_3(P_2O_7)_2$ XRD showed the triclinic (or anorthic) symmetry of the compound (space group P-1), identical to the one obtained by Slobodianik et al. [423]. Its lattice constants are a = 5.3590 Å, b = 6.5630 Å, c = 16.2990 Å, α = 81.28°, β = 82.69°, γ = 72.43°.

At the same temperature $LiMnPO_4$ phase showed the ortorhombic crystal symmetry (space group Pnma), identical to the one obtained by Geller et al. [424]. Its lattice constants are a = 10.4600 Å, b = 6.1000 Å, c = 4.7440 Å, α = 90.00°, β = 90.00°, γ = 90.00°. The profile refinement of the diagram evidenced the presence of some impurities, their identification using *PDF4+* database led to the obvious phase of Al_2O_3 (presumptive from a crucible) but some other smaller peaks remained unindexed.

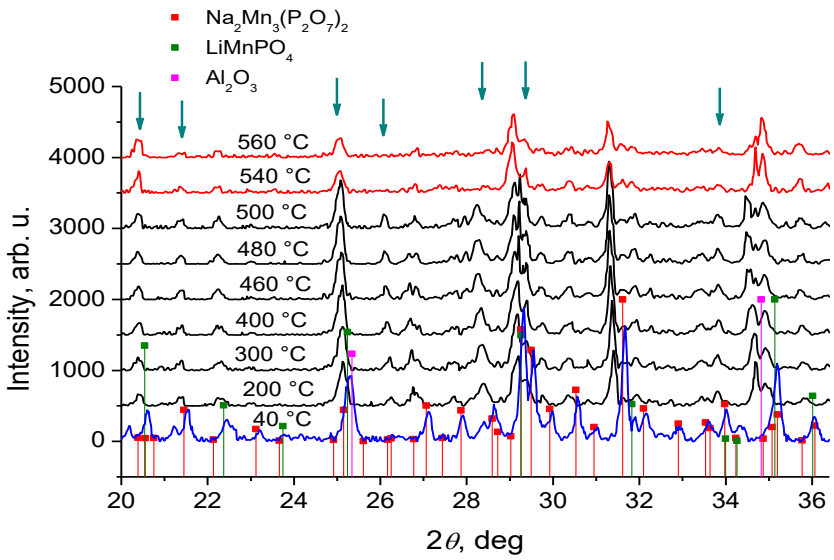

Fig. 3.6. The thermal XRD spectra of the $NaLiMnP_2O_7$ mixed phase compound. Positions of Bragg's diffraction lines are presented by colored squares. Arrows indicate the peaks which show phase transition of $Na_2Mn_3(P_2O_7)_2$. Alumina which was used as sample holder can also be seen in the diffractgram.

The phase change was proved by thermal XRD. At elevated temperatures on thermal diffraction diagrams (see Fig. 3.6) the evolution of intensities and positions of the peaks indicates a slow and progressive structural transition occurring between 500 °C and 540 °C. The reduction of peaks which can be associated with structural changes of $Na_2Mn_3(P_2O_7)_2$ phase are observable at 2θ values of about 21.4°, 25.2°, 26.3°, 26.8°, 28.7°, 29.5°, and 34.0°, while the amplification at value is visible at 20.3° and shape changes of the peaks at values around 29.0° and 35.0°. However, the multi-phase effect and impurities prevents us from carrying out Rietveld refinement, but the phase transition is evidenced from the raw thermal XRD data (Fig. 3.6). No evident changes of peak intensities in thermal XRD were observed for $LiMnPO_4$ phase.

Electrical measurements

The impedances of $NaLiMnP_2O_7$ ceramics measured at different temperatures are represented in Fig. 3.7. The ionic conductivity of the compound was found to be of $5.26 \cdot 10^{-9}$ S/m at 400 K temperature on heating stage and only vanishingly higher on cooling stage (probably due to partially frozen more conductive phase). The step-like phase transition determined the

conductivity increase of about 3 orders of magnitude in a narrow range of temperature.

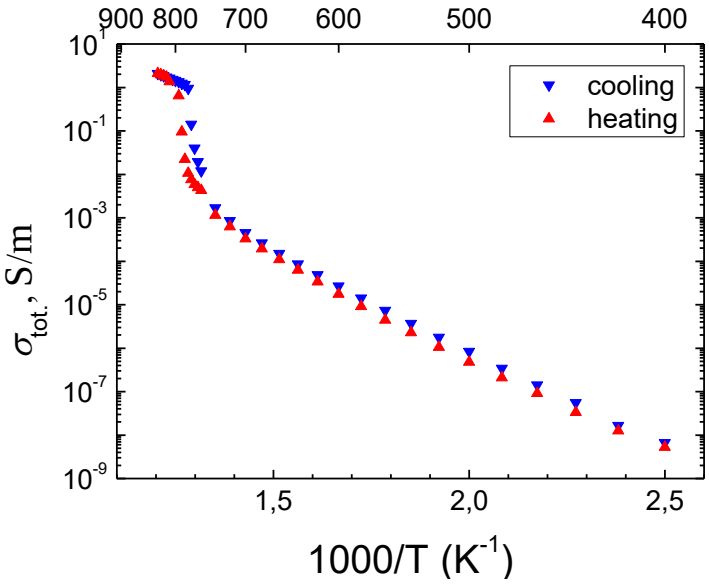

Fig. 3.7. The plot of the total conductivity of $NaLiMnP_2O_7$ ceramics measured in ambient air on both heating and cooling stages. The increase of the conductivity at 760-810 K temperature was associated with the phase transition taking place in the ceramics.

From the temperature dependences of the real part of conductivity (Fig. 3.8) and the real part of dielectric permittivity (Fig. 3.9) we can see the step-like increase/decrease of both quantities at 760-810 K and it is frequency independent. The activation energy decreases after a phase transition to superionic state, as the energy barriers for the mobile ions decrease. This result supports the phase transition hypothesis.

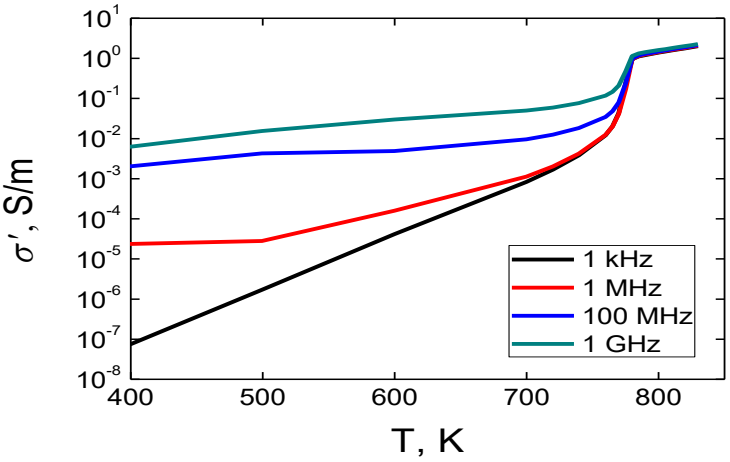

Fig. 3.8. Temperature dependences of the real part of conductivity measured at different frequencies. The frequency independent increase of the real part of conductivity at 760-810 K temperature was associated with the phase transition taking place in the ceramics.

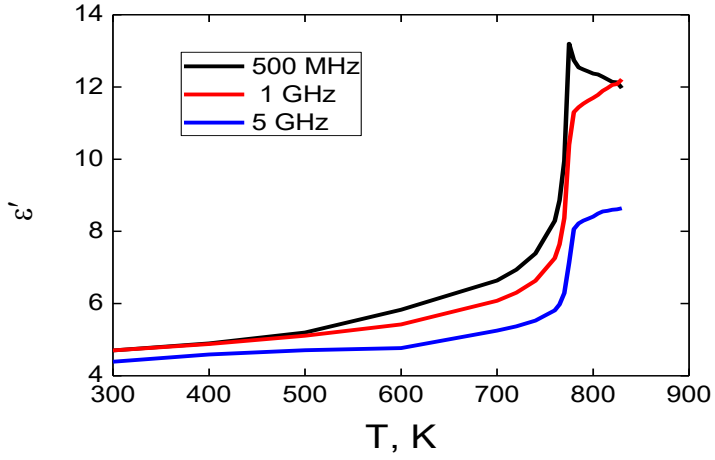

Fig. 3.9. Temperature dependence of the real part of dielectric permittivity. The frequency independent increase of the real part of dielectric permittivity at 760-810 K temperature was associated with the phase transition taking place in the ceramics.

The differential thermal analysis also showed an endothermic peak at 803 K when heating the sample and the exothermic peak at 743 K on cooling (Fig. 3.10), which shows that the phase transition is reversible. The phase transition onset temperature is in very good agreement with electrical conductivity measurements. The temperatures approaching the melting point of the sample investigated usually leads to shifts of absolute values of DTA curve values at the highest temperatures when comparing heating and cooling ranges like one can see in Fig. 3.10.

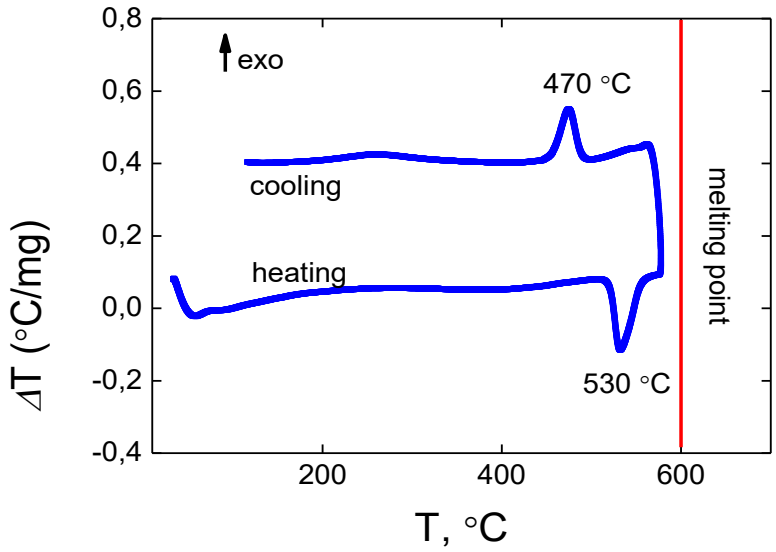

Fig. 3.10. The differential thermal analysis of $NaLiMnP_2O_7$ ceramics. Endothermic peak at 530 °C and exothermic one at 470 °C supports the theory of the phase transition taking place in the ceramics.

3.1.4 Other mixed phase compounds of $Na_{2-x}Li_xMnP_2O_7$ system

A group of $Na_{2-x}Li_xMnP_2O_7$ (x = 0.0, 0.5, 1.0, 1.5, 2.0) compounds were investigated by structural analysis and electrical methods.

XRD analysis of $Li_2MnP_2O_7$ compound revealed that it is two-phase material and consists of $Mn_2P_2O_7$ and $Li_4P_2O_7$ phases.

XRD analysis of $Na_{0.5}Li_{1.5}MnP_2O_7$ compound revealed that it is based on $Li_2MnP_2O_7$ phase with slight amount of $Mn_2P_4O_{12}$ phase and unindexed sodium containing phase.

XRD analysis of $Na_{1.5}Li_{0.5}MnP_2O_7$ compound revealed that it is two-phase material and consists of $Mn_2P_2O_7$ and $Li_4P_2O_7$ phases with minutely

smaller fraction of the latter phase than in $Li_2MnP_2O_7$ compound. The almost identical XRD patterns of $Li_2MnP_2O_7$ and $Na_{1.5}Li_{0.5}MnP_2O_7$ compounds are evident from Fig. 3.11.

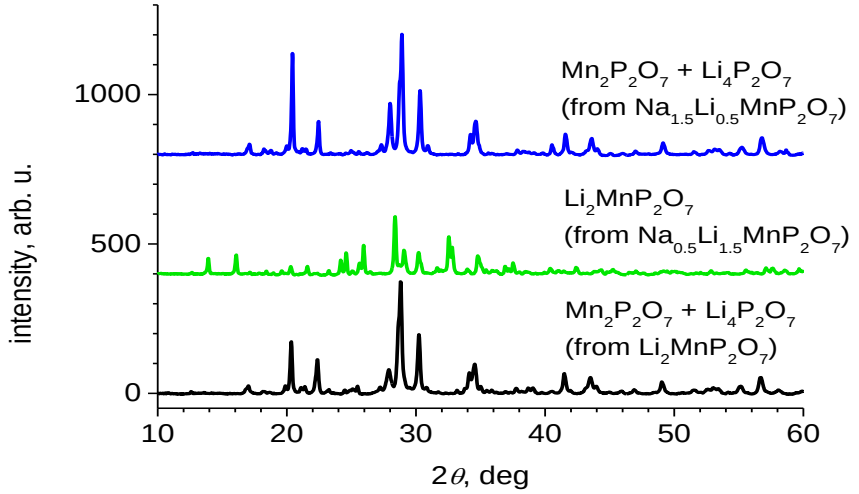

Fig. 3.11. X-ray diffraction patterns of various $Na_{2-x}Li_xMnP_2O_7$ ceramics. It is evident from diffractogramms that both $Li_2MnP_2O_7$ and $Na_{1.5}Li_{0.5}MnP_2O_7$ consist of two identical phases $Mn_2P_2O_7$ and $Li_4P_2O_7$.

Impedance spectroscopy analysis revealed the tendency of the conductivity increasing when the sodium fraction is higher in $Na_{2-x}Li_xMnP_2O_7$ system (see Fig. 3.12). $Li_2MnP_2O_7$ compound obeys Arrhenius law pretty well in all temperature range. Only negligible deviations of activation energy can be observed at 580 and 700 K temperature points. In the conductivity graphs of both $Na_{0.5}Li_{1.5}MnP_2O_7$ and $Na_{1.5}Li_{0.5}MnP_2O_7$ compounds slight change of the activation energies can be observed but no thermal X-ray diffraction analysis were done for the determining the nature of that variations.

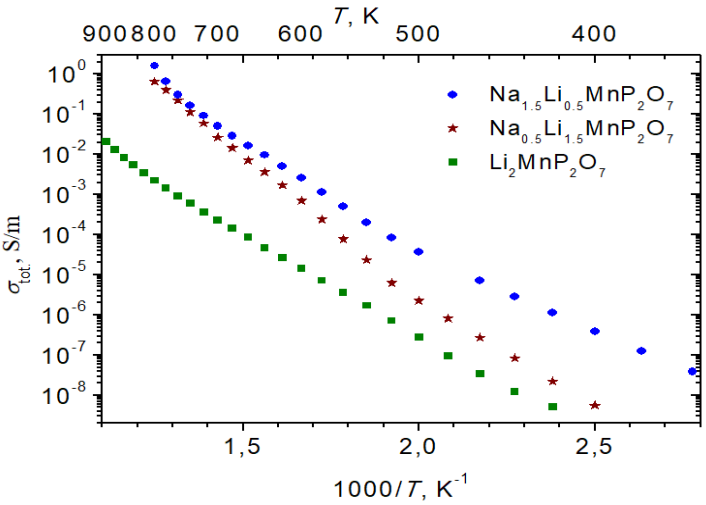

Fig. 3.12. Temperature dependencies of the total ionic conductivities of various $Na_{2-x}Li_xMnP_2O_7$ compounds.

3.1.5 Conductivity characteristics of $Na_2ZnP_2O_7$, $NaCsMnP_2O_7$ and $NaCsZnP_2O_7$ pyrophosphates in comparison with $Na_2MnP_2O_7$ compound

As X-ray diffraction indicates, almost single phase $Na_2ZnP_2O_7$ compounds have been obtained (Fig. 3.13). Very small amount of $Zn_2P_2O_7$ impurities were detected.

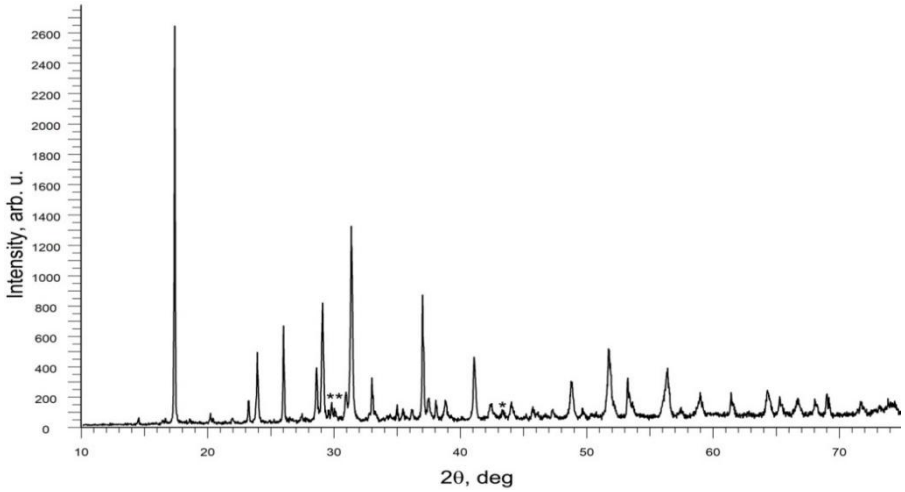

Fig. 3.13. X-ray diffraction pattern of $Na_2ZnP_2O_7$. $Zn_2P_2O_7$ impurities are marked by stars.

It was demonstrated that phase transition takes place in $Na_2MnP_2O_7$ compound when the sample is heating. In Fig. 3.14 the conductivities of some closely related pyrophosphates are depicted. One can observe that $Na_2ZnP_2O_7$ has similar conductivity values to those of $Na_2MnP_2O_7$ compound at intermediate temperatures, but it is less conductive at lower and higher temperatures. The lower conductivity of $Na_2ZnP_2O_7$ compared to $Na_2MnP_2O_7$ at the temperature range 550-800 K is related to phase transition which takes place only in manganese containing sodium pyrophosphates, but not in zinc ones. The lower conductivity of $Na_2ZnP_2O_7$ at 300-400 K temperature interval probably is caused by the fact that the latter material is less hydrophilic than $Na_2MnP_2O_7$. The proton conductivity in $Na_2ZnP_2O_7$ disappears at 340 K while in $Na_2MnP_2O_7$ only at 370 K.

As we can see from Fig. 3.14 both $NaCsMnP_2O_7$ and $NaCsZnP_2O_7$ are very hydrophilic materials and the conductivity deviation from Arrhenius law is evident actually up to 420 K temperature. At intermediate temperatures $NaCsZnP_2O_7$ compound is much less conductive than $NaCsMnP_2O_7$ one and missing points come at the temperature range from 330 K to 480 K – the impedance spectrometer was not capable to register the electrical parameters at these temperature values for $NaCsZnP_2O_7$ compound. Surprisingly, despite conductivity variations at low and intermediate temperature ranges, at 800 K temperature the values of conductivity for the materials $Na_2ZnP_2O_7$, $NaCsMnP_2O_7$ and $NaCsZnP_2O_7$ were almost identical to each other and were of about $1.5 \cdot 10^{-2}$ S/m.

Due to these interesting conductivity peculiarities more detailed studies of more complex pyrophosphates will be presented in next two chapters. $Na_2MnP_2O_7$ and $Na_2ZnP_2O_7$ will be combined and obtained mixed phase compound $Na_2Zn_{0.5}Mn_{0.5}P_2O_7$ will be investigated. Similarly, $NaCsMnP_2O_7$ and $NaCsZnP_2O_7$ will be combined and the mixed phase compound $NaCsZn_{0.5}Mn_{0.5}P_2O_7$ will be analyzed in detail.

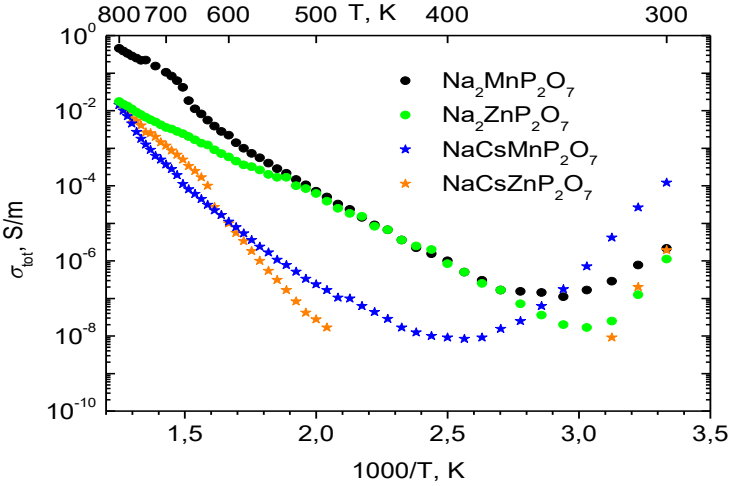

Fig. 3.14. Representation of total ionic conductivities of $Na_2MnP_2O_7$, $Na_2ZnP_2O_7$, $NaCsMnP_2O_7$ and $NaCsZnP_2O_7$ pyrophosphates. Phase transition occurs only in $Na_2MnP_2O_7$ compound at 660-680 K temperature.

3.1.6 Structure and conductivity of $Na_2Zn_{0.5}Mn_{0.5}P_2O_7$ ceramics

Crystalline structure

The analysis of XRD patterns show that $Na_2Zn_{0.5}Mn_{0.5}P_2O_7$ powder prepared by solid state reaction at RT consists of two phases: $Na_2MnP_2O_7$ crystallizes in triclinic space group $P\bar{1}$ (XRD card 074-2586) as it was summarized in [311], and $Na_2ZnP_2O_7$ crystallizes in the tetragonal space group $P4_2/mmm$ (XRD card 01-070-5836) and it is identical to the one obtained in [289]. The lattice parameters, unit cell volume (V), angles (α, β, γ), formula units in the unit cell (Z) and theoretical density (ρ_{th}) of both phases at RT are presented in Table 3.1. The quantitative crystallographic analysis showed that the obtained composite consists of 38.64 wt. % $Na_2MnP_2O_7$ phase and 61.36 wt. % $Na_2ZnP_2O_7$ phase. This composition differs from the one expected from the compound stoichiometry and indicates that a fraction of $Na_2MnP_2O_7$ compound could be present in amorphous phase and/or that Mn partially replaces Zn in tetragonal $Na_2ZnP_2O_7$ crystallites.

Table 3.1. Summary of X-ray diffraction analysis of $Na_2Zn_{0.5}Mn_{0.5}P_2O_7$ powder at room temperature.

Phase	*a*, Å	*b*, Å	*c*, Å	α, deg	β, deg	γ, deg	*V*, Å^3	Z	ρ_{th}, g/cm^3
$Na_2MnP_2O_7$	9.89(4)	11.08(5)	12.46(3)	148.48	121.98	68.35	595.18(15)	4	3.07
$Na_2ZnP_2O_7$	7.72(5)	10.27(4)	-	-	-	-	612.13(15)	4	3.10

XRD patterns recorded during heating and cooling processes do not reveal any appearance or disappearance of the peaks (Fig. 3.15). As the only certain difference between patterns at different temperatures is continuous shift of the peaks towards lower 2θ values during heating and towards higher 2θ values during cooling, it is presumed that there are no changes in the phase composition of the sample and all changes are related to the lattice parameter variation due to the thermal expansion. The temperature dependences of the lattice parameters and theoretical densities of the $Na_2MnP_2O_7$ and $Na_2ZnP_2O_7$ compounds at heating and cooling are presented in Fig. 3.16a and Fig. 3.16b, respectively.

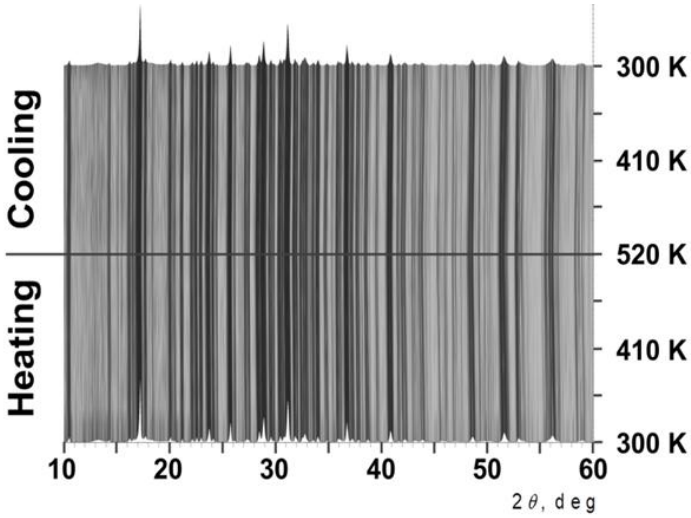

Fig. 3.15. Pseudo 3D montage of XRD patterns of $Na_2Zn_{0.5}Mn_{0.5}P_2O_7$ powder at heating and cooling in 300-520 K temperature range. No structural changes can be observed from the montage.

The lattice parameters of the $Na_2ZnP_2O_7$ phases in the investigated temperature range increase linearly at heating and decrease linearly at cooling. The temperature hysteresis of *a* and *c* lattice parameters at heating and cooling was observed for $Na_2MnP_2O_7$ phase. The available XRD data does not provide any evidence of formation of new phases and can be attributed to evaporation of adsorbed water. Water adsorption at the surface of other similar pyrophosphate ceramics like $Na_2MnP_2O_7$ [425] and $NaCsZn_{0.5}Mn_{0.5}P_2O_7$ [426] has also been observed.

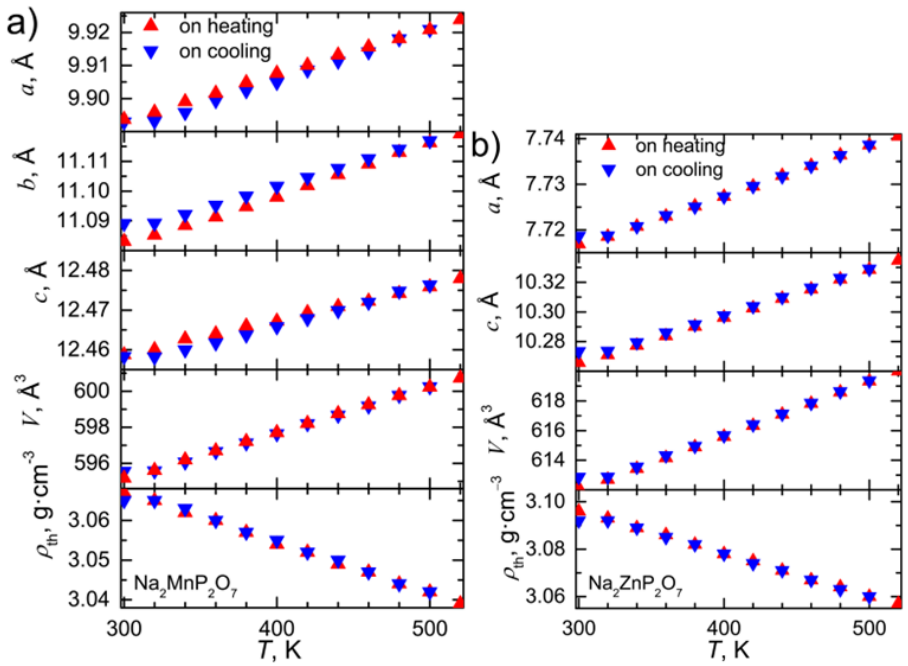

Fig. 3.16. Temperature dependences of the lattice parameters and theoretical densities of $Na_2MnP_2O_7$ a) and $Na_2ZnP_2O_7$ b) compounds on heating and cooling. No anomalies of the lattice parameters can be observed from the picture.

SEM image of the surface of $Na_2Zn_{0.5}Mn_{0.5}P_2O_7$ ceramics is presented in Fig. 3.17. The grain sizes of the ceramics vary in the range from approximately 3 to 21 μm.

The experimental density of the composite was measured by geometrical methods and found to be 2.73 g/cm^3 while the ratio between the density obtained experimentally and calculated theoretically is 88%.

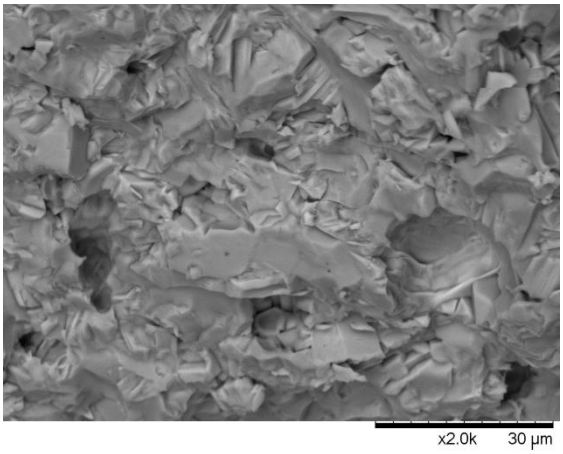

Fig. 3.17. SEM image of $Na_2Zn_{0.5}Mn_{0.5}P_2O_7$ ceramics.

Fig. 3.18 shows EDX spectra of $Na_2Zn_{0.5}Mn_{0.5}P_2O_7$ powder and ceramic samples. The calculated theoretical elemental composition and the results of XFS, EDX and XPS spectra analysis of the $Na_2Zn_{0.5}Mn_{0.5}P_2O_7$ powder and ceramic samples are presented in Table 3.2.

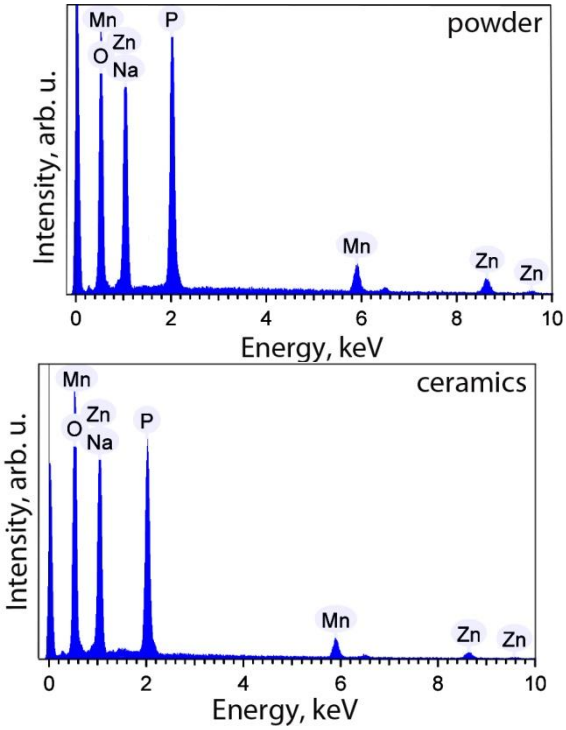

Fig. 3.18. EDX spectra of $Na_2Zn_{0.5}Mn_{0.5}P_2O_7$ powder and ceramics.

Table 3.2. Theoretical and experimental elemental composition of $Na_2Zn_{0.5}Mn_{0.5}P_2O_7$ powder and ceramic samples.

Element	Theoretical, wt. %	From XFS, wt. % Powder	From EDX, wt. % Ceramics	Error, wt.%	From EDX, wt. % Powder	Error, wt.%	From XPS, wt.% ** Ceramics
Na	16.42	18.90	16.90	0.42	18.04	0.37	16.52
Zn	11.67	11.84	11.16	0.72	11.27	0.63	15.79
Mn	9.81	9.72	8.00	0.29	6.21	0.21	13.27
P	22.12	20.60	20.69	0.32	17.82	0.25	22.79
O	39.98	38.94*	43.25	0.56	46.66	0.50	31.63

*calculated value, **after Ar^+ ion beam sputtering for 390 s

The comparison of experimental and theoretical elemental composition of $Na_2Zn_{0.5}Mn_{0.5}P_2O_7$ indicates P and Mn deficiency in the ceramic samples and excess of Na in the powder. However, the analysis of XPS spectra showed the excess of Zn and Mn after the etching of the ceramic surface. The characteristic Mn 2p and O 1s core level XPS spectra for 390 s etched surface of $Na_2Zn_{0.5}Mn_{0.5}P_2O_7$ ceramics are shown in Fig. 3.19a and Fig. 3.19b, respectively.

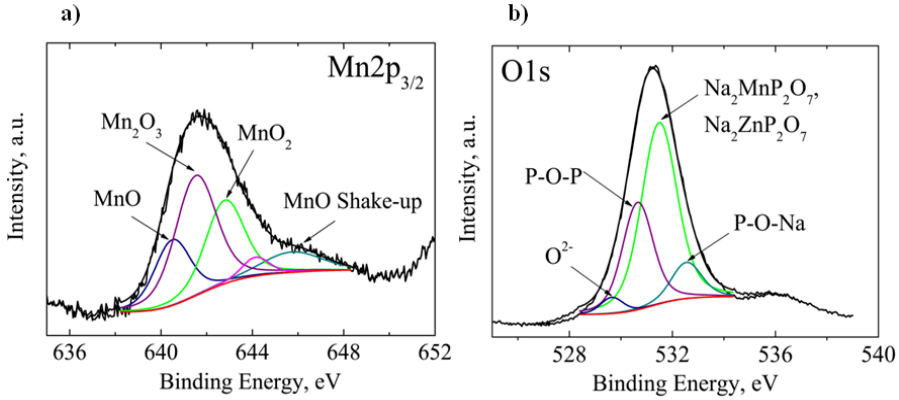

Fig. 3.19. Mn $2p_{3/2}$ a) and O 1s b) core levels XPS spectra for surface of $Na_2Zn_{0.5}Mn_{0.5}P_2O_7$ ceramic.

Mn $2p_{3/2}$ core level XPS spectra were deconvoluted in three multiple peaks with different binding energy. The peak located at the binding energy 640.05 eV is associated with Mn^{2+} valence state as in MnO [427]. The multi peak at binding energy 641.40 eV is related with Mn^{3+} valence state as in Mn_2O_3 previously reported in [428]. Mn $2p_{3/2}$ core level peak at 641.90 eV is associated with Mn^{4+} valence state ion as in MnO_2 [429] and correlated well with results already published in [430]. In the range (644-648) eV diffuse MnO shake – up peak is detected. The amounts of the Mn^{2+}, Mn^{3+} and Mn^{4+}

valence state in the investigated ceramics were 3.6, 5.2 and 4.3 wt.%, respectively. As the band energy states of electrons have crucial impact on the voltage profiles of a material the manganese atoms' multi-valency (Mn^{2+}, Mn^{3+} and Mn^{4+} valence states) effect revealed by XPS analysis in $Na_2Zn_{0.5}Mn_{0.5}P_2O_7$ compound can determine high redox potentials within it suggesting sodium-based manganese pyrophosphates as very favourable cathodic materials for solid state battery applications.

The O 1s spectrum for $Na_2Zn_{0.5}Mn_{0.5}P_2O_7$ ceramics is of asymmetric shape, which could be fitted with an intense component and three lower intensity peaks. The highest intensity peak is centered at binding energy 531.4 eV (amount 16.45 wt. %) and other lower intensity peaks are located at binding energies 530.65 eV (amount 9.47 wt. %), 532.54 eV (amount 3.53 wt. %) and 529.64 eV (amount 1.03 wt. %). The peak with the highest intensity can be attributed to the lattice oxygen O^{2-} in the $Na_2MnP_2O_7$ and $Na_2ZnP_2O_7$ phases. The peak at binding energy 530.6 eV represents structural amount of OH^- group as in the manganite compounds family [429]. The peak at binding energy 532.54 eV can be attributed to the P-O-Na bindings as in [431, 432].

Electrical measurements

The frequency dependences of the real part of complex conductivity (σ') of $Na_2Zn_{0.5}Mn_{0.5}P_2O_7$ ceramics, which was measured at different temperatures, are shown in Fig. 3.20. A dispersion region was found in conductivity spectra of $Na_2Zn_{0.5}Mn_{0.5}P_2O_7$ ceramics.

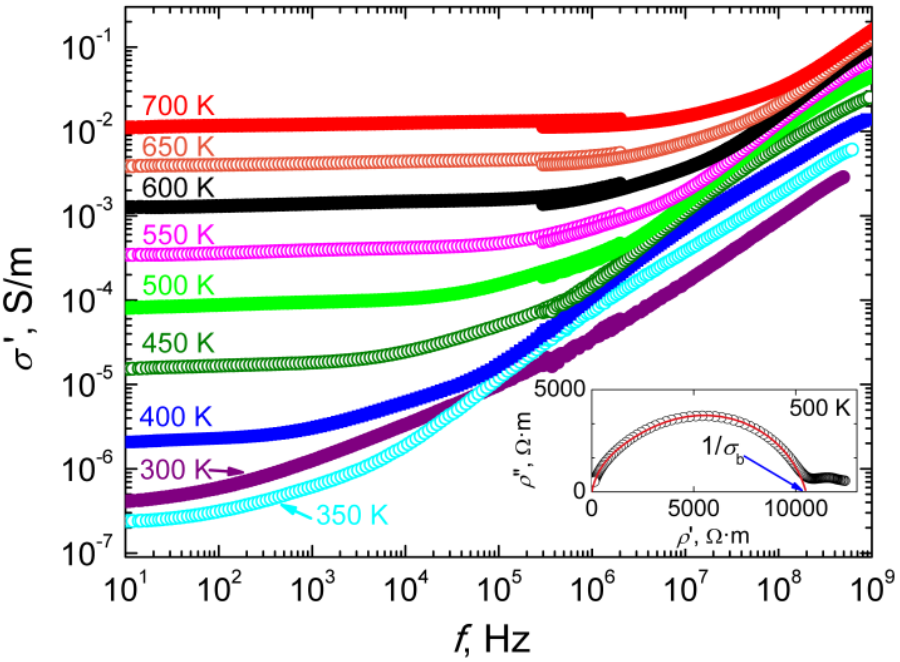

Fig. 3.20. Frequency dependences of σ' for $Na_2Zn_{0.5}Mn_{0.5}P_2O_7$ ceramics at different temperatures. Inset shows Nyquist impedance plot at 500 K.

The process is thermally activated and dispersion region shifts towards higher frequencies as temperature increases in the temperature range 350-700 K. This phenomenon is typical for relaxation type dispersions [433]. The conductivity dispersion above 350 K can be attributed to Na^+ ion migration in the grains of the ceramic samples as in [434-436]. The temperature dependences of bulk electrical conductivity (σ_b) of the ceramics were derived from Nyquist impedance plots (see inset of Fig. 3.20). The temperature dependences of σ_b of $Na_2Zn_{0.5}Mn_{0.5}P_2O_7$ ceramics at heating and cooling are presented in Fig. 3.21.

Non-Arrhenius behavior of $\sigma_b(1000/T)$ was observed in the temperature range from 300 K to 360 K. The decrease of $Na_2Zn_{0.5}Mn_{0.5}P_2O_7$ ceramics conductivity in the above mentioned temperature range on heating can be associated with water loss, besides the conductivity starts to increase rapidly on cooling stage from 330 K down to 300 K. The conductivity increases on cooling because of adsorbed water. This phenomenon was also observed in $Na_2MnP_2O_7$ [425], $NaCsZn_{0.5}Mn_{0.5}P_2O_7$ [426], $A_{0.9}In_{0.1}P_2O_7$ (A= Sn, Ti) [396] and CeP_2O_7 [437]. Big influence of water to the conductivity at temperatures up to ~350 K is also observed for $Na_2MnP_2O_7$ [425] and

$Na_2ZnP_2O_7$ ceramics, their conductivity temperature dependences are presented in Fig. 3.21 for comparison.

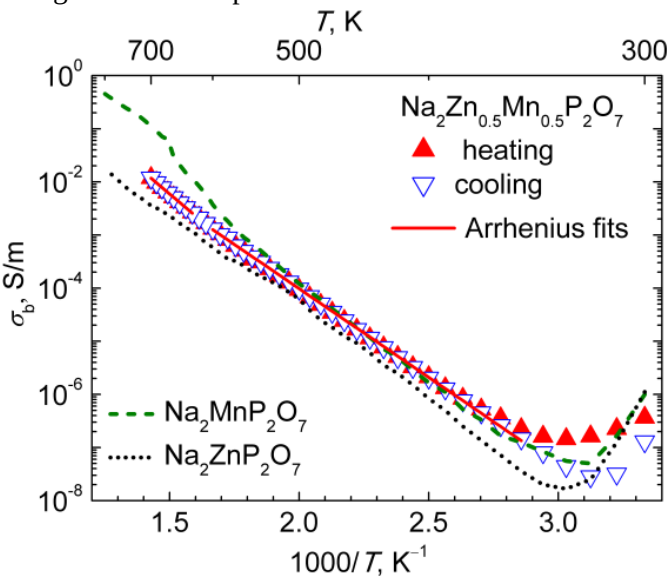

Fig. 3.21. Temperature dependences of bulk electrical conductivity of $Na_2Zn_{0.5}Mn_{0.5}P_2O_7$ ceramics during heating and cooling. Conductivities of $Na_2ZnP_2O_7$ and $Na_2MnP_2O_7$ [425] phases are also presented for comparison.

Further conductivity increase with temperature in the temperature interval (350-700) K was described by Arrhenius law. The data in graphical representation of conductivity in logarithmic scale vs. reciprocal temperature can be fitted by straight line, the slope of which is proportional to the activation energy of σ_b. A change of $Na_2Zn_{0.5}Mn_{0.5}P_2O_7$ bulk conductivity's activation energy (ΔE_b) is observed in the temperature range from 600 to 630 K. ΔE_b = 0.66 eV in the temperature range from 350 K to 600 K, while at temperatures higher than 630 K ΔE_b = 0.83 eV. Knowing that $Na_2Zn_{0.5}Mn_{0.5}P_2O_7$ is mixed phase material, consisting of $Na_2ZnP_2O_7$ and $Na_2MnP_2O_7$, the latter should be responsible for the change of conductivity activation energy. The phase transition in $Na_2MnP_2O_7$ was observed at 660 K, which led to step-like conductivity increase on heating. In $Na_2ZnP_2O_7$ material no phase transitions were found in the whole temperature range of investigation. In the temperature range of 350 K to 600 K the conductivity values of $Na_2Zn_{0.5}Mn_{0.5}P_2O_7$ are close to the ones of $Na_2MnP_2O_7$, while at temperature higher than the phase transition, the value of the conductivity of $Na_2Zn_{0.5}Mn_{0.5}P_2O_7$ is mostly ruled by the lower conductivity of $Na_2ZnP_2O_7$.

However, the change of activation energy in $Na_2Zn_{0.5}Mn_{0.5}P_2O_7$ composite at 630 K is caused by the phase transition taking place in $Na_2MnP_2O_7$ phase.

The temperature dependences of the real part of dielectric permittivity (ε') and dielectric loss was investigated at frequency of 1 GHz. This frequency is higher than Maxwell relaxation frequency ($f_M = \sigma'/2\pi\varepsilon'\varepsilon_0$, where $\varepsilon_0 = 8.85 \times 10^{-12}$ F/m is dielectric constant of the vacuum) at any measurement temperature, as can be seen from Fig. 3.22a. At 630 K the change of activation energy of f_M was found. The relaxation frequency activation energy in the temperature range 350-630 K is 0.69 eV, and at temperatures from 630 to 700 K it is 0.9 eV. The obtained values are close to the activation energies found from temperature dependences of bulk conductivity.

The temperature dependence of ε' of $Na_2Zn_{0.5}Mn_{0.5}P_2O_7$ ceramics measured at heating and cooling is shown in Fig. 3.22b. No difference in ε' values can be observed comparing heating and cooling data points. This observation suggests that all polarization processes taking place in the bulk of ceramics are reversible. Hence dielectric permittivity determined at 1 GHz is not connected with water release which we observe from conductivity temperature behaviour.

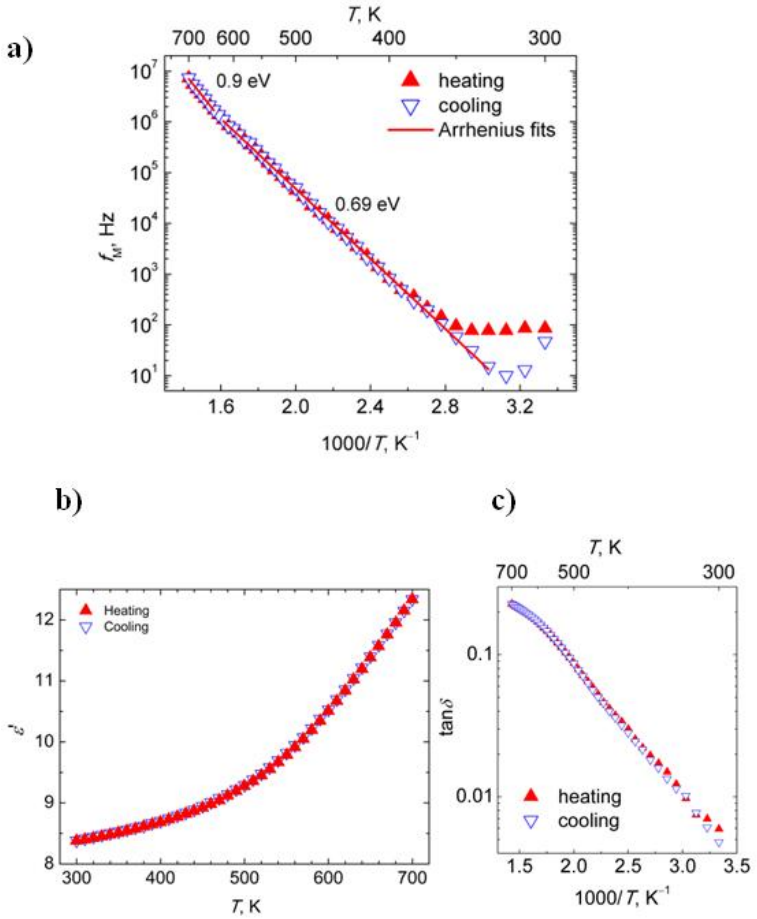

Fig. 3.22. Temperature dependences of Maxwell relaxation frequency a), real part of complex dielectric permittivity b) and dielectric losses c) of $Na_2Zn_{0.5}Mn_{0.5}P_2O_7$ ceramics measured at 1 GHz on heating and cooling.

The increase of value of dielectric permittivity from 8.4 to 12.3 is observed over the whole measured temperature range. The increase of ε' with temperature is caused by contribution of electronic polarization, vibration of the lattice, migration polarization of Na^+ ions in the grains of $Na_2Zn_{0.5}Mn_{0.5}P_2O_7$ ceramics. As the dielectric losses (Fig. 3.22c) represent conductivity ($\tan\delta = \sigma'/\sigma''$), $\tan\delta$ is shown in Arrhenius representation. A change of the slope was found at about 630 K, which corresponds to the change of conductivity activation energy and it was related to the phase transition taking place in $Na_2MnP_2O_7$ constituent of $Na_2Zn_{0.5}Mn_{0.5}P_2O_7$ ceramics. Besides, we can see that at high frequency (1 GHz) water does not

influence ionic transport properties at low temperatures of 300-350 K. So the low temperature conductivity values are caused by surface water diffusion and probably by the contribution of grain boundaries and porosity.

3.1.7 Influence of structural changes in $NaCsZn_{0.5}Mn_{0.5}P_2O_7$ on its electrical properties

Crystalline structure

The results of XRD measurements show that $NaCsZn_{0.5}Mn_{0.5}P_2O_7$ powder prepared by solid state reaction are mixed phase compound. Three different phases were detected in the X-ray diffraction patterns of the powder. $NaCsZnP_2O_7$ (65.61 wt.%), $NaCsMnP_2O_7$ (15.35 wt.%) and $Cs_2MnP_4O_{12}$ (19.04 wt.%) phases were found in the powder at room temperature. The results of analysis of XRD patterns show that $NaCsZnP_2O_7$ compound belongs to monoclinic symmetry (space group P21/n) with four formula units in the unit cell. The analysis of $NaCsMnP_2O_7$ XRD patterns show that this phase crystallizes in the orthorhombic symmetry (space group Cmc21) (No. 36 card 089-5449) and this result is in good correlation with [311]. The $Cs_2MnP_4O_{12}$ crystallizes in monoclinic structure (space group P21/n) as it was reported in [438]. The lattice parameters, unit cell volume (V), angle (β), formula units in the unit cell (Z) and theoretical density (d_t) of the three phases at RT are presented in Table 3.3.

Table 3.3. Summary of X-ray diffraction analysis of $NaCsZn_{0.5}Mn_{0.5}P_2O_7$ powder at room temperature.

Phase	Space group	a, Å	b, Å	c, Å	β	V, Å³	Z	d_t, g/cm³
$NaCsMnP_2O_7$	$Cmc2_1$	5.3203(4)	15.0477(5)	7.9974(3)		784.370	4	3.534
$NaCsZnP_2O_7$	$P2_1/n$	13.0105(2)	7.6912(6)	7.4241(5)	91.030(2)	742.797	4	3.259
$Zn_2MnP_4O_{12}$	$P2_1/n$	7.9809(2)	13.2416(2)	11.5396(2)	101.988(3)	1192.912	4	3.545

Pseudo 3D montage of XRD patterns of $NaCsZn_{0.5}Mn_{0.5}P_2O_7$ powder is recorded during in-situ heating and cooling in 300–700 K temperature range.

XRD patterns recorded during heating and cooling processes do not reveal any appearance or disappearance of the peaks (Fig. 3.23). As the only certain difference between patterns at different temperatures is continuous shift of the peaks towards lower 2θ values during heating and towards higher 2θ values during cooling, it is presumed that there are no changes in the phase composition of the sample and all changes are related to the lattice parameter variation due to the thermal expansion.

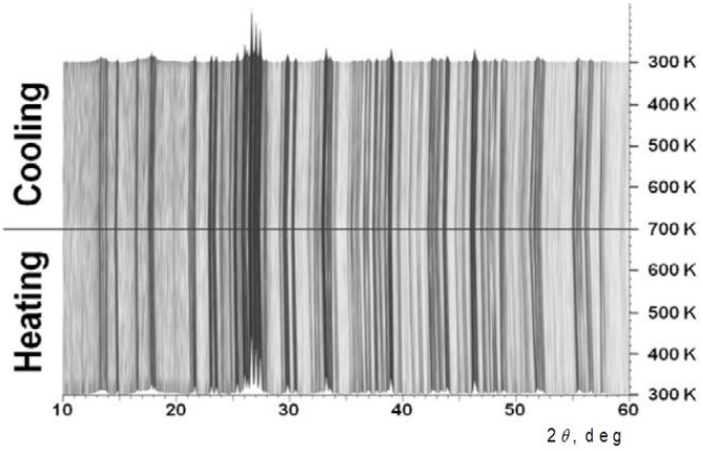

Fig. 3.23. Pseudo 3D montage of XRD patterns of $NaCsZn_{0.5}Mn_{0.5}P_2O_7$ powder at heating and cooling in 300-700 K temperature range. No structural changes can be observed from the montage.

The temperature dependences of the lattice parameters of the $NaCsMnP_2O_7$, $NaCsZnP_2O_7$ and $Cs_2MnP_4O_{12}$ compounds at heating and cooling are presented in Fig. 3.24a, Fig. 3.24b, and Fig. 3.24c, respectively. In the temperature region (400–500) K the anomalies of lattice parameters and cell volume in the $NaCsMnP_2O_7$ XRD patterns were found. The anomalies of a, b, c and V lattice parameters in the $Cs_2MnP_4O_{12}$ phase are detected in the temperature range (500–600) K. These anomalies remain in $NaCsMnP_2O_7$ and $Cs_2MnP_4O_{12}$ phases at cooling of the powder to room temperature. The temperature hysteresis of b, c and V lattice parameters at the heating and cooling was observed for $Cs_2MnP_4O_{12}$ phase. The available XRD data does not provide any evidence of formation of new phases also there are no trustworthy indications of elemental interdiffusion between phases. Therefore, it is assumed that the anomalies of the lattice parameters in temperature range (400–500) K for $NaCsMnP_2O_7$ and in temperature range (500–600) K for $Cs_2MnP_4O_{12}$ can be caused by structural disordering in these phases. On the other hand, in comparison to conventional XRD measurements usage of laboratory scale heating chamber slightly reduces XRD data resolution/quality and in-situ XRD measurements at synchrotron facilities might reveal another cause (for example delicate phase change, cation interdiffusion, etc.) of the observed anomalies. The lattice parameters of the $NaCsZnP_2O_7$ compound in the investigated temperature range increase linearly with temperature.

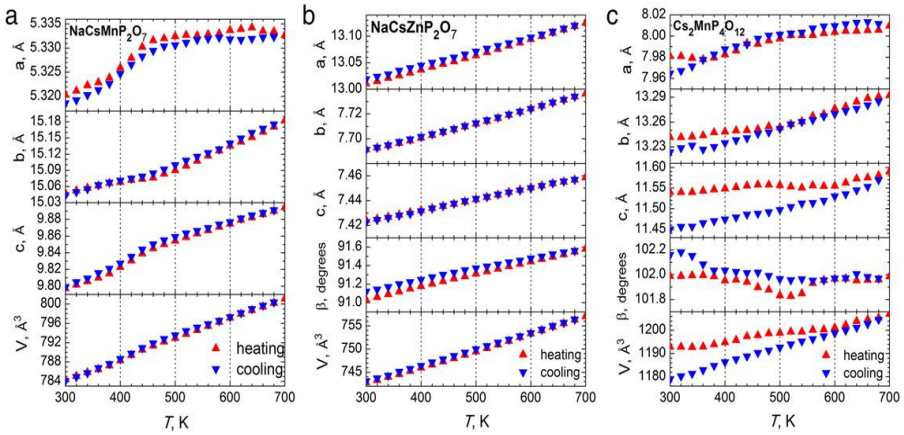

Fig. 3.24. The temperature dependences of lattice parameters of $NaCsMnP_2O_7$ a), $NaCsZnP_2O_7$ b) and $Cs_2MnP_4O_1$ c) phases. Lattice anomalies associated with $NaCsMnP_2O_7$ and $Cs_2Mn_4O_{12}$ phases can be seen from the picture.

The results of the DSC and TG measurements of the $NaCsZn_{0.5}Mn_{0.5}P_2O_7$ powder are displayed in Fig. 3.25. The results of TG investigation show that mass decrease with temperature and at T = 800K the change was found to be 1.4%. This weight loss can be attributed to evaporation of hydrated water as in $A_{0.9}In_{0.1}P_2O_7$ (A=Sn, Ti) pyrophosphates [396]. The diffuse change of DSC graph is detected in the temperature range (500–600) K. This change is associated with the change of structural parameters of $Cs_2MnP_4O_{12}$ phase.

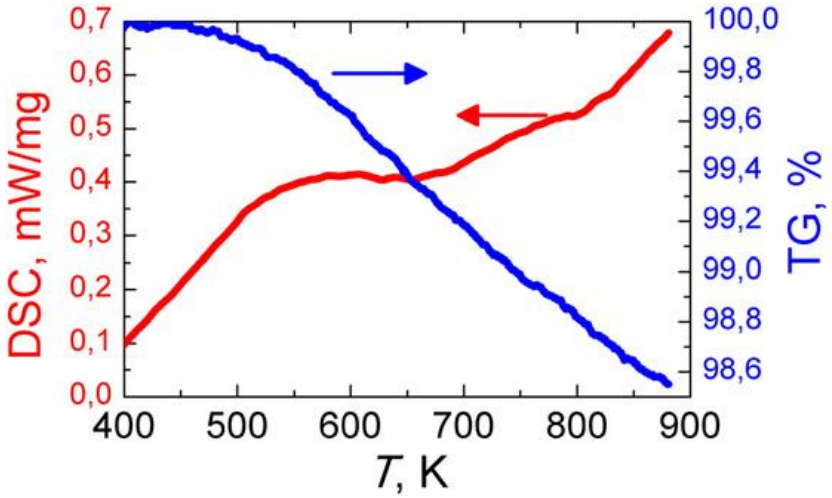

Fig. 3.25. Differential scanning calorimetry (DSC) and thermogravimetric (TG) analysis of $NaCsZn_{0.5}Mn_{0.5}P_2O_7$ powders.

SEM image of the surface of ceramic is presented in Fig. 3.26. The grain sizes of the ceramic vary in the range from approximately 5–16 μm.

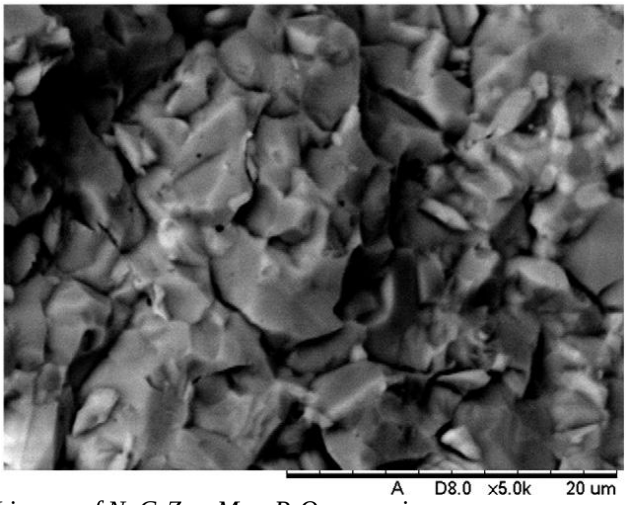

Fig. 3.26. SEM image of $NaCsZn_{0.5}Mn_{0.5}P_2O_7$ ceramic

Fig. 3.27a and Fig. 3.27b show EDX spectra of the investigated $NaCsZn_{0.5}Mn_{0.5}P_2O_7$ powder and ceramics respectively. The analysis of EDX spectra of the $NaCsZn_{0.5}Mn_{0.5}P_2O_7$ powder and ceramic shows that content of sodium practically remains the same after sintering, despite the fact that sodium is an element, which can easily evaporate. The comparison of experimental and theoretical elemental composition of $NaCsZn_{0.5}Mn_{0.5}P_2O_7$ indicates P and O deficiency and excess of Cs.

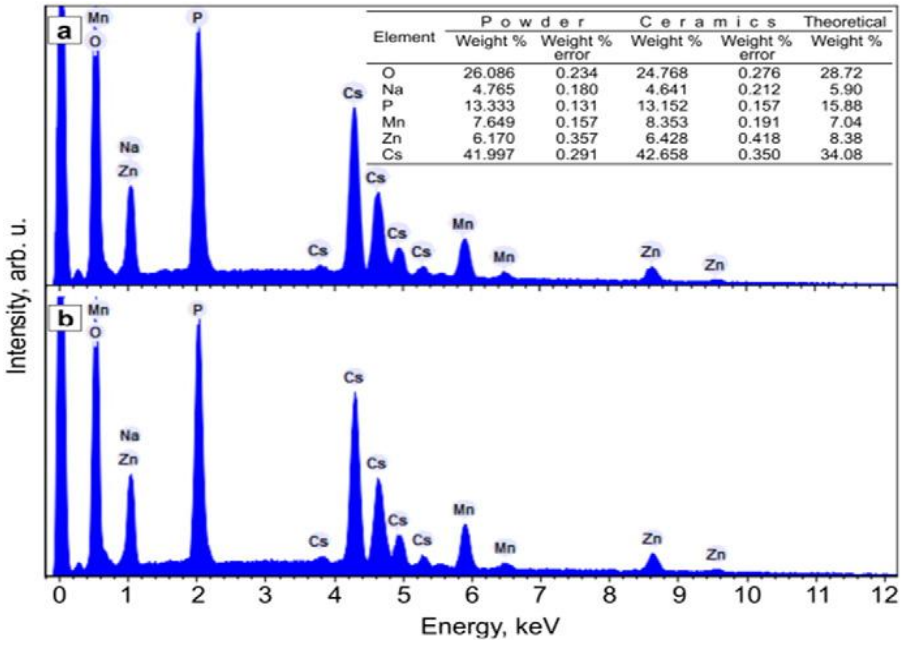

Element	Powder		Ceramics		Theoretical
	Weight %	Weight % error	Weight %	Weight % error	Weight %
O	26.086	0.234	24.768	0.276	28.72
Na	4.765	0.180	4.641	0.212	5.90
P	13.333	0.131	13.152	0.157	15.88
Mn	7.649	0.157	8.353	0.191	7.04
Zn	6.170	0.357	6.428	0.418	8.38
Cs	41.997	0.291	42.658	0.350	34.08

Fig. 3.27. EDX spectra and elemental composition in weight percent's of $NaCsZn_{0.5}Mn_{0.5}P_2O_7$ powder a) and ceramic b).

Electrical measurements

The characteristic frequency dependences of the real part of complex conductivity (σ') of $NaCsZn_{0.5}Mn_{0.5}P_2O_7$ ceramic, which were measured at different temperatures, are shown in Fig. 3.28. A dispersion region was found in conductivity spectra of $NaCsZn_{0.5}Mn_{0.5}P_2O_7$ ceramic. The process in the investigated ceramic is thermally activated and dispersion region shifts towards higher frequencies as temperature increases in the temperature range 420–700 K. This phenomenon is typical for relaxation type dispersions. The conductivity dispersion can be attributed to Na^+ ion migration in the grains of the ceramic samples as in [434-436].

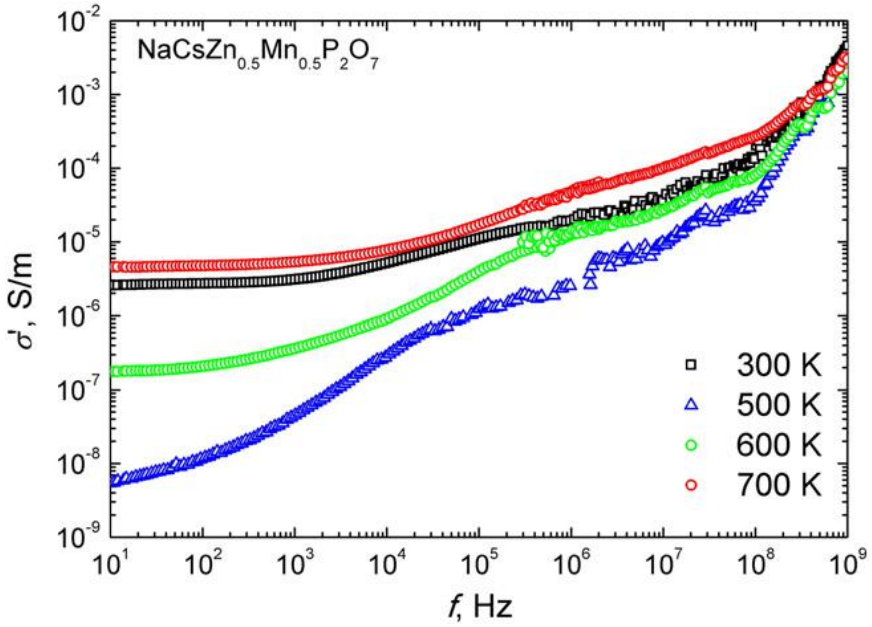

Fig. 3.28. The characteristic frequency dependences of the real part of complex conductivity (σ') of $NaCsZn_{0.5}Mn_{0.5}P_2O_7$ ceramic at various temperatures.

The temperature dependences of total electrical conductivity ($\sigma_{10\ Hz}$) of the ceramics were derived at 10 Hz, where is the plateau of $\sigma'(f)$ dependences. The temperature dependences of $\sigma_{10\ Hz}$ of $NaCsZn_{0.5}Mn_{0.5}P_2O_7$ ceramic at heating and cooling are presented in Fig. 3.29.

Non-Arrhenius behaviour of $\sigma_{10\ Hz}(1/T)$ was observed in the temperature range 300–420 K. The total conductivity of $NaCsZn_{0.5}Mn_{0.5}P_2O_7$ ceramic decreases in this temperature range and this phenomenon can be associated with dehydration of the samples and loss of phosphorus oxide. This phenomenon was also observed in $A_{0.9}In_{0.1}P_2O_7$ (A=Sn,Ti) [396] and CeP_2O_7 [437] pyrophosphates.

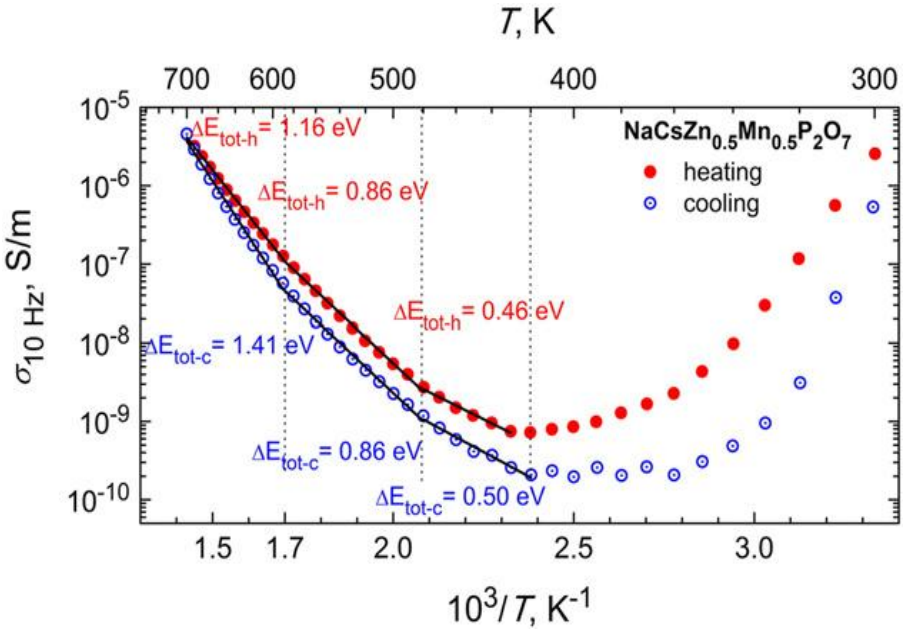

Fig. 3.29. The temperature dependences of total electrical conductivity ($\sigma_{10\ Hz}$) of $NaCsZn_{0.5}Mn_{0.5}P_2O_7$ ceramic during heating and cooling. The activation energies of total electrical conductivity at heating ($\Delta E_{tot\text{-}h}$) and cooling ($\Delta E_{tot\text{-}c}$) are also shown for the particular temperature ranges. Proton conductivity is evident in the temperature range between 300 K and 420 K.

The temperature range 420–700 K can be approximately divided into three temperature intervals, where total electrical conductivity increases with temperature according to Arrhenius law with different activation energies (see Table 3.4). The temperature hysteresis of σ' value was found at heating and cooling of $NaCsZn_{0.5}Mn_{0.5}P_2O_7$ ceramic. The decrease of the temperature from T = 420 K to RT leads to non-Arrhenius change of $\sigma_{10\ Hz}$ values. The results of the measurements of total conductivity at temperatures 450, 550 and 650 K and activation energies of total conductivities are summarized in Table 3.4.

Table 3.4. The values of total electrical conductivity ($\sigma_{10\ Hz}$) of $NaCsZn_{0.5}Mn_{0.5}P_2O_7$ ceramic at various temperatures (T) and its activation energies at heating ($\Delta E_{tot\text{-}h}$) and cooling (ΔEtot-c).

	Heating		Cooling	
T, K	$\sigma_{10\ Hz}$, S/m	$\Delta E_{tot\text{-}h}$, eV	$\sigma_{10\ Hz}$, S/m	$\Delta E_{tot\text{-}c}$, eV
450	1.19×10^{-9}	0.46	4.14×10^{-10}	0.50
550	3.17×10^{-8}	0.86	1.3×10^{-8}	0.86
650	8.88×10^{-7}	1.16	5.42×10^{-7}	1.41

The results of XRD measurements has shown anomalies of the lattice parameters in temperature range (400–500) K in orthorhombic $NaCsMnP_2O_7$ and in temperature range (500–600) K in monoclinic $Cs_2MnP_4O_{12}$, but the symmetry group of above mentioned compounds has not changed. It is possible that detected anomalies of electrical properties are caused by disordering in the $NaCsMnP_2O_7$ and $Cs_2MnP_4O_{12}$ lattices as is observed in other compounds from pyrophosphates family [222, 439]. Structural phase transition is a common phenomenon in many pyrophosphates such as $Na_2FeP_2O_7$ [302], $Na_4P_2O_7$ [440] and $Na_2CoP_2O_7$ [441]. The phase transition from triclinic (β) to monoclinic (α) $Na_2FeP_2O_7$ was indicated above 833 K. Structural phase transitions ε → δ, δ → γ, γ → β and β → α were indicated in $Na_4P_2O_7$ at temperatures 663, 777, 785 and 823 K respectively. These transitions were also observable by electrical measurements as activation energy of conductivity was changing during transitions [440]. The endothermic peak at 653 K, which was obtained by differential thermal analysis (DTA), is due to the phase transition in $Na_4P_2O_7$.

The temperature dependences of relaxation frequency (f_r) were determined from the maximum of the $\rho''(f)$ spectra measured at different temperatures. The characteristic $\rho''(f)$ spectra at different temperatures are presented in Fig. 3.30.

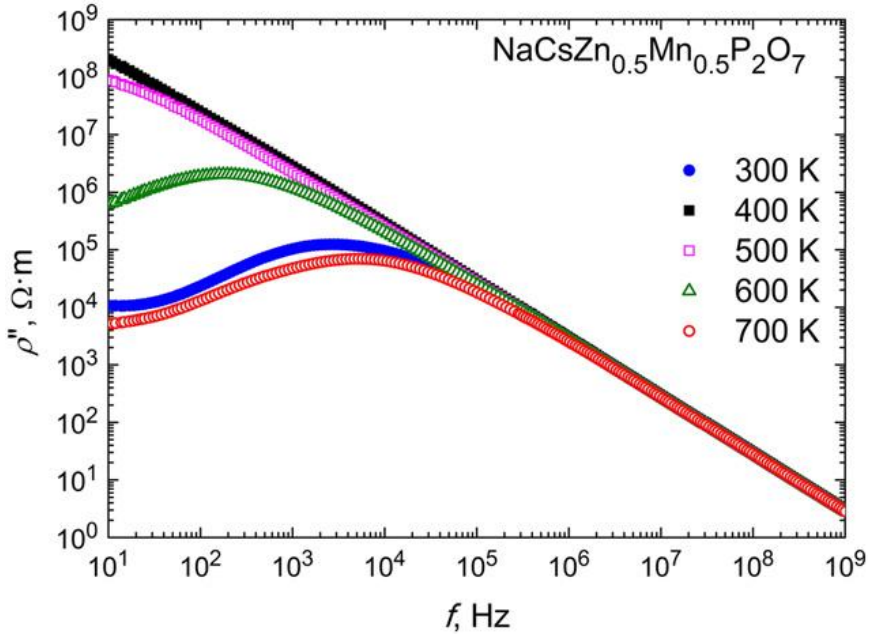

Fig. 3.30. The frequency dependences of imaginary part of complex resistivity at different temperatures for $NaCsZn_{0.5}Mn_{0.5}P_2O_7$ ceramic.

With the increase of temperature from 500 K to 700 K the maximum of $\rho''(f)$ shift towards high frequencies according to Arrhenius law. In the temperature range from RT to 340 K the maximum of ρ'' shifts to lower frequencies and in temperature interval (340–520) K the maximum disappears from the frequency range of measurement. The temperature dependences of f_r at heating and cooling are presented in Fig. 3.31.

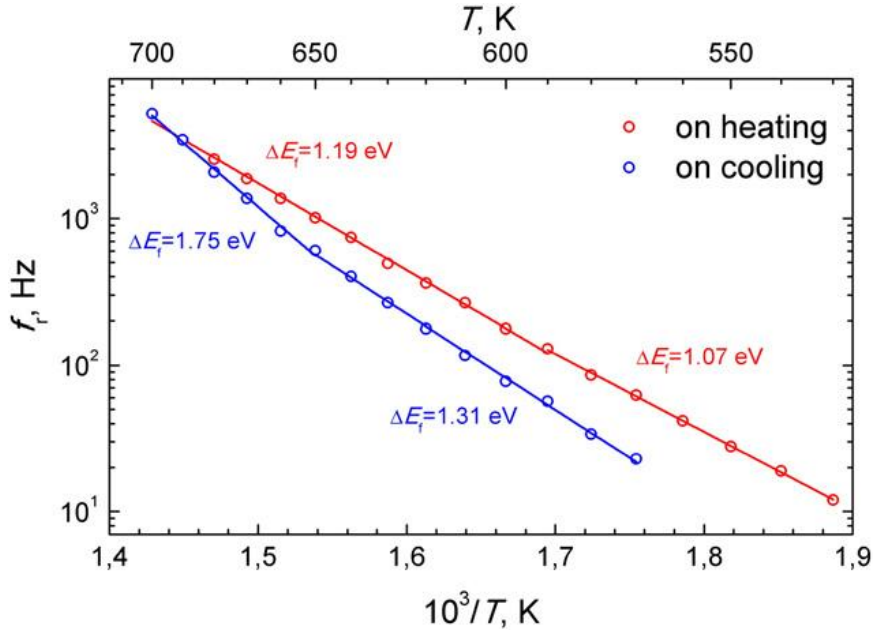

Fig. 3.31. The dependences of relaxation frequency of $NaCsZn_{0.5}Mn_{0.5}P_2O_7$ ceramic on the reciprocal temperature during the heating and cooling of ceramic.

The anomalies of f_r and their activation energies (ΔE_{fr}) were found. The values of ΔE_{fr} are different at heating and cooling (see Table 3.5).

Table 3.5. The activation energies of relaxation frequency for $NaCsZn_{0.5}Mn_{0.5}P_2O_7$ ceramic.

Temperature range, K	ΔE_{fr}, eV (heating)	Temperature range, K	ΔE_{fr}, eV (cooling)
530–590	1.07	570–650	1.31
590–700	1.19	650–700	1.75

The temperature dependences of the real part of dielectric permittivity (ε') and dielectric loss ($\tan\delta$) were investigated in the frequency range from 1 MHz to 1 GHz. The frequencies in this range are higher than Maxwell relaxation frequency at 700 K ($f_M = \sigma'/2\pi\varepsilon'\varepsilon_0$, where $\varepsilon_0 = 8.85\times 10^{-12}$ F/m is dielectric constant of the vacuum). The calculated Maxwell relaxation frequency at 700 K for $NaCsZn_{0.5}Mn_{0.5}P_2O_7$ ceramic is about 0.13 MHz. The characteristic temperature dependences of ε' and $\tan\delta$ of $NaCsZn_{0.5}Mn_{0.5}P_2O_7$ ceramics measured at heating and cooling are shown in Fig. 3.32a.

In the temperature range (400–500) K the anomalies of ε' and tanδ were observed. The anomalies can be associated with structural disordering in $NaCsMnP_2O_7$ lattice. These anomalies can be observed on heating and cooling of the samples. The peak temperature of ε' values is dependent on measurements frequency as shown in Fig. 3.32b. The values of ε' decrease and the peak shifts towards higher temperature side when frequency increases. This phenomenon is typical for order-disorder type second order phase transitions as were reported in [442, 443].

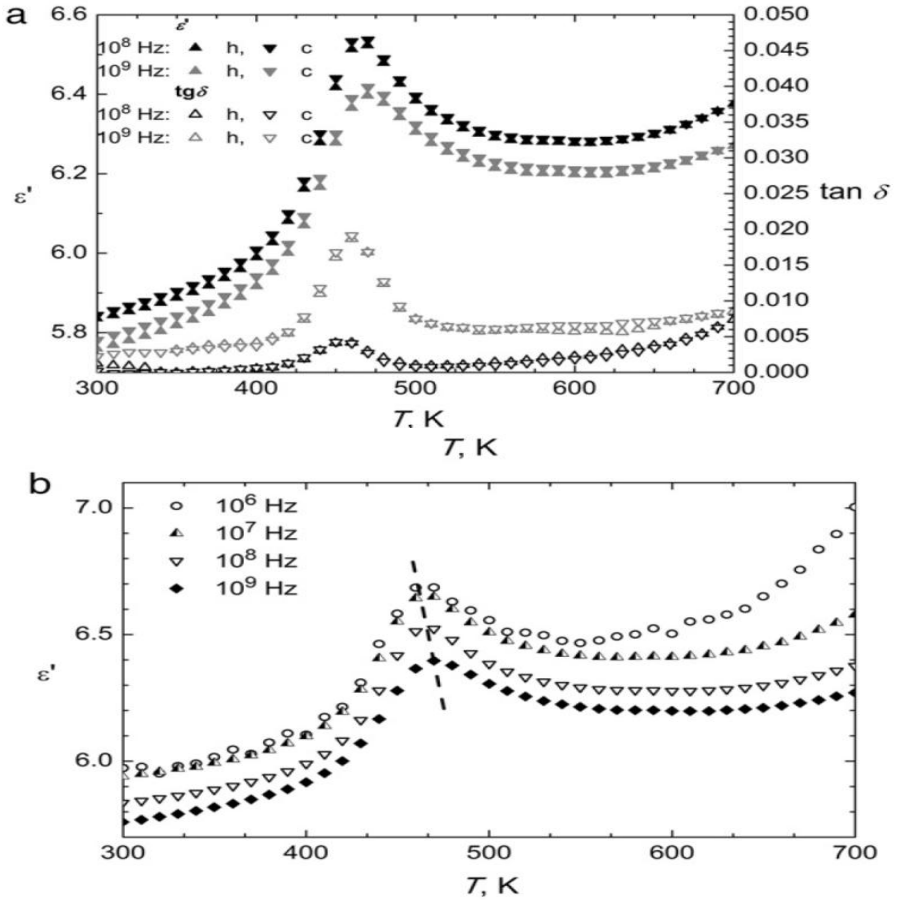

Fig. 3.32. The temperature dependences of the real part of complex dielectric permittivity (ε') and dielectric loss (tanδ) at 10^8 and 10^9 Hz frequencies on heating (h) and cooling (c) a). The temperature dependences of ε' at 10^6, 10^7, 10^8 and 10^9 Hz frequencies b).

3.2 Impact on conductivity of lithium and sodium exchange in $Li_{0.5-y}Na_yLa_{0.5}Nb_2O_6$

Crystalline structure

As can be seen from Table 3.6 and Table 3.7 the lattice parameters and unit cell volume for $Li_{0.5-y}Na_yLa_{0.5}Nb_2O_6$ compounds with y = 0 and 0.5 linearly increase with increasing temperature. Besides the lanthanum site occupancies at z = 0 and z = 1/2 planes do not change in the studied temperature range.

Table 3.6. Structure parameters of $Li_{0.5}La_{0.5}Nb_2O_6$ at different temperatures.

T, °C	20	300	600	900
Unit cell parameters				
a, Å	3.899(1)	3.908(1)	3.923(2)	3.931(3)
b, Å	3.901(1)	3.911(1)	3.925(2)	3.933(3)
c, Å	7.8542(6)	7.8791(8)	7.9090(7)	7.9250(6)
V, Å^3	119.48(5)	120.43(5)	121.72(8)	122.5(1)
Site occupancies, La				
z = 0	0.475(4)	0.475(4)	0.472(4)	0.471(4)
z = 1/2	0.065(4)	0.065(4)	0.068(4)	0.069(4)
Agreement factors				
Rp, %	6.23	6.62	7.02	7.09
Rwp, %	7.94	8.39	9.04	9.19

Table 3.7. Structure parameters of $Na_{0.5}La_{0.5}Nb_2O_6$ at different temperatures.

T, °C	20	300	600	900
Unit cell parameters				
a, Å	3.923(2)	3.936(2)	3.944(1)	3.956(1)
b, Å	3.924(2)	3.935(2)	3.951(1)	3.964(1)
c, Å	7.8512(7)	7.8774(8)	7.9143(5)	7.9368(5)
V, Å^3	120.86(9)	122.01(9)	123.33(4)	124.46(5)
Site occupancies, La				
z = 0	0.256(6)	0.255(8)	0.252(5)	0.257(5)
z = 1/2	0.244(6)	0.245(8)	0.248(5)	0.243(5)
Agreement factors				
Rp, %	7.13	6.73	6.62	6.90
Rwp, %	9.23	8.37	9.15	8.88

Electrical measurements

An example of complex resistivity spectrum for $Li_{0.3}Na_{0.2}La_{0.5}Nb_2O_6$ ceramics is shown in Fig. 3.33. The figure is a usual resistivity representation in the complex plain and it shows two spectra measured at 300 K by two-electrode method and by four-electrode method.

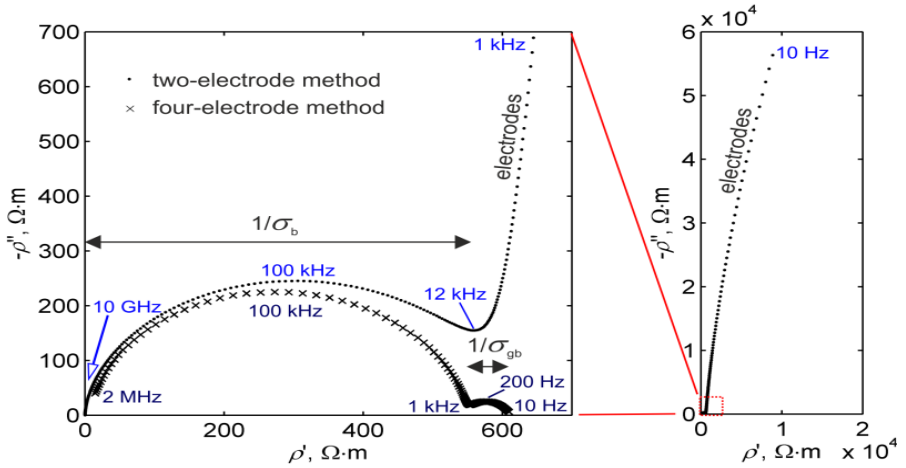

Fig. 3.33. Complex plain resistivity plots of $Li_{0.3}Na_{0.2}La_{0.5}Nb_2O_6$ ceramics measured at 300 K by two- and four-electrode methods. Some frequencies are shown for selected characteristic points.

Two semicircles can clearly be seen from the data obtained by four-electrode method. Such spectrum can easily be modelled by two series processes, each of them were described by resistance (R) connected in parallel with a constant phase element (CPE). The impedance of CPE is expressed as:

$$\tilde{Z}_{CPE} = \frac{1}{Q(j\omega)^n}, \tag{3.1}$$

where $\omega = 2\pi f$ is the angular frequency, and the true capacitance of the process is found from equation:

$$C = \frac{(Q \cdot R)^{1/n}}{R}. \tag{3.2}$$

The spectrum of each R||CPE connection is of depressed semicircle shape in the complex plain plot. The semicircle at lower frequencies between 10 Hz and 1 kHz can be attributed to ionic relaxation in the grain boundaries of the ceramics with the corresponding typical capacitance value of $1.4 \cdot 10^{-8}$ F. From the diameter of the semicircle the grain boundary conductivity (σ_{gb}) can be found. Similarly, the higher frequency semicircle represents

ionic relaxation in the grains (bulk) of ceramics. The grain or bulk conductivity (σ_b) can be found from the diameter of the semicircle and the corresponding capacitance value was $2 \cdot 10^{-12}$ F.

Comparing the spectrum obtained by four-electrode method with the one obtained by two-electrode method, one can see some important differences. The spectrum obtained by two-electrode method has an additional part in the low frequency range (from 12 kHz to 10 Hz), which is attributed to ion blocking at the electrode-electrolyte interface. Therefore the imaginary part of complex resistivity rises with decrease of frequency, which is a clear feature of capacitive electrode nature. The local minimum of ρ'' was found at 12 kHz, which is much higher compared to the four-electrode spectrum (1 kHz). This shows that the grain boundary contribution to the two-electrode spectrum is masked by the processes taking place at the electrode. However, the ionic relaxation frequency in the grains of ceramics (frequency of the grain semicircle maximum) was found to be the same from both measurements: $f = 1/(2\pi RC) = 100$ kHz. So, the grain conductivity σ_b (the diameter of high frequency semicircle) can be found by equivalent circuit modelling from measurements by two-electrode method.

The above analysed example (Fig. 3.33) for the composition with y = 0.2 is the most clear. For other compositions similar impedance spectra were obtained, but in some cases only a trace of low frequency semicircle was observed, so the precise determination of the grain boundary conductivity was very difficult. The conductivity of ceramics grain boundary highly depends on the ceramic quality and microstructure (grain size, density, crack and impurity level, etc.), which may slightly wary among different samples. The Arrhenius plot of grain boundary conductivity with different lithium concentrations is presented in Fig. 3.34. One can observe that higher lithium concentration at the temperature interval 300-470 K does not enhance the grain boundary conductivity of the sample because of the bottleneck size limitations as discussed in [370].

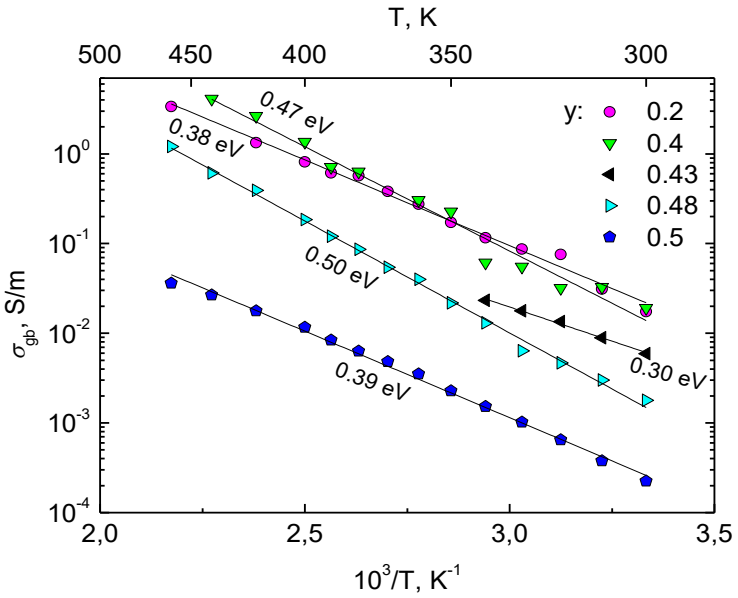

F*ig. 3.34. Grain boundary Arrhenius plot for* $Li_{0.5-y}Na_yLa_{0.5}Nb_2O_6$ *compounds with different sodium concentration y. The activation energies are indicated for different sample compositions.*

Temperature dependences of lithium-ion conductivity in the ceramic grains with different amount of sodium (y) are presented in Fig. 3.35. Arrhenius-type conductivity behaviour with temperature was found only for the sample with y = 0. For all other samples the change of activation energy can be observed at high temperatures (> 500 K). The lowering of activation energy is observed at higher temperatures for the compounds in which the sodium to lithium exchange ratio is higher (red line in Fig. 3.35). In the lower temperature range (300–500 K) the activation energy of ~ 0.4 eV has been found, while at high temperatures it is about 0.2 eV.

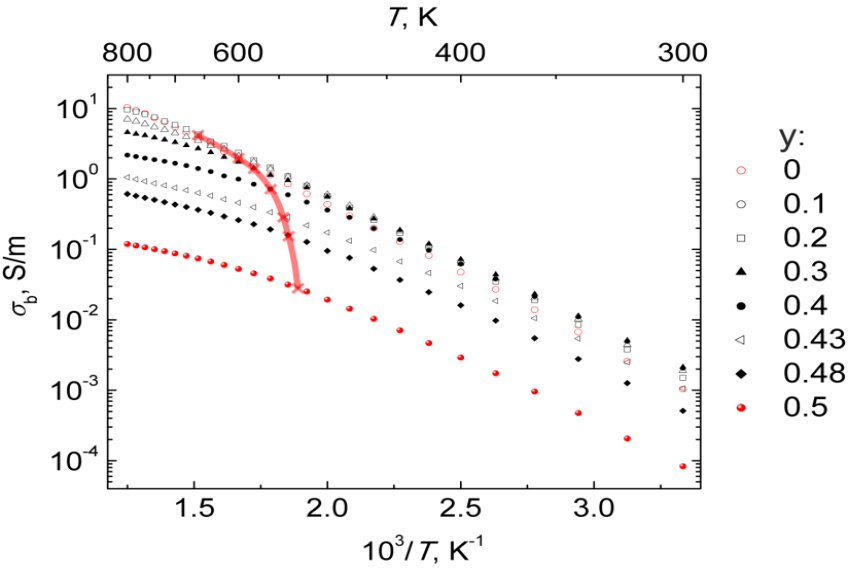

Fig. 3.35. Bulk conductivity Arrhenius plot for $Li_{0.5-y}Na_yLa_{0.5}Nb_2O_6$ compounds with different sodium concentration y. Thick red line approximately shows the change of activation energy.

Concentration dependences of conductivity in the bulk of ceramics grains obtained from impedance spectroscopy data are presented in Fig. 3.36. At 300 K the bulk conductivity increases from $1 \cdot 10^{-3}$ to $2.1 \cdot 10^{-3}$ $S \cdot m^{-1}$ when lithium is substituted with sodium and reaches the maximum value at y = ~ 0.4 (Fig. 3.36a and Fig. 3.36b curve 1). At 400 K the conductivity increases from $4.8 \cdot 10^{-2}$ to maximal value of $7.2 \cdot 10^{-2}$ $S \cdot m^{-1}$ at about y = 0.3 (Fig. 3.36b, curve 2). At higher temperatures the conductivity maximum shifts to the direction of lower sodium concentrations, for example at 500 K the maximum value can be found when y = 0.2 (Fig. 3.36b, curve 3), though at 800 K ionic conductivity lowers continuously with the lithium-ion exchange with sodium (Fig. 3.36b, curve 4).

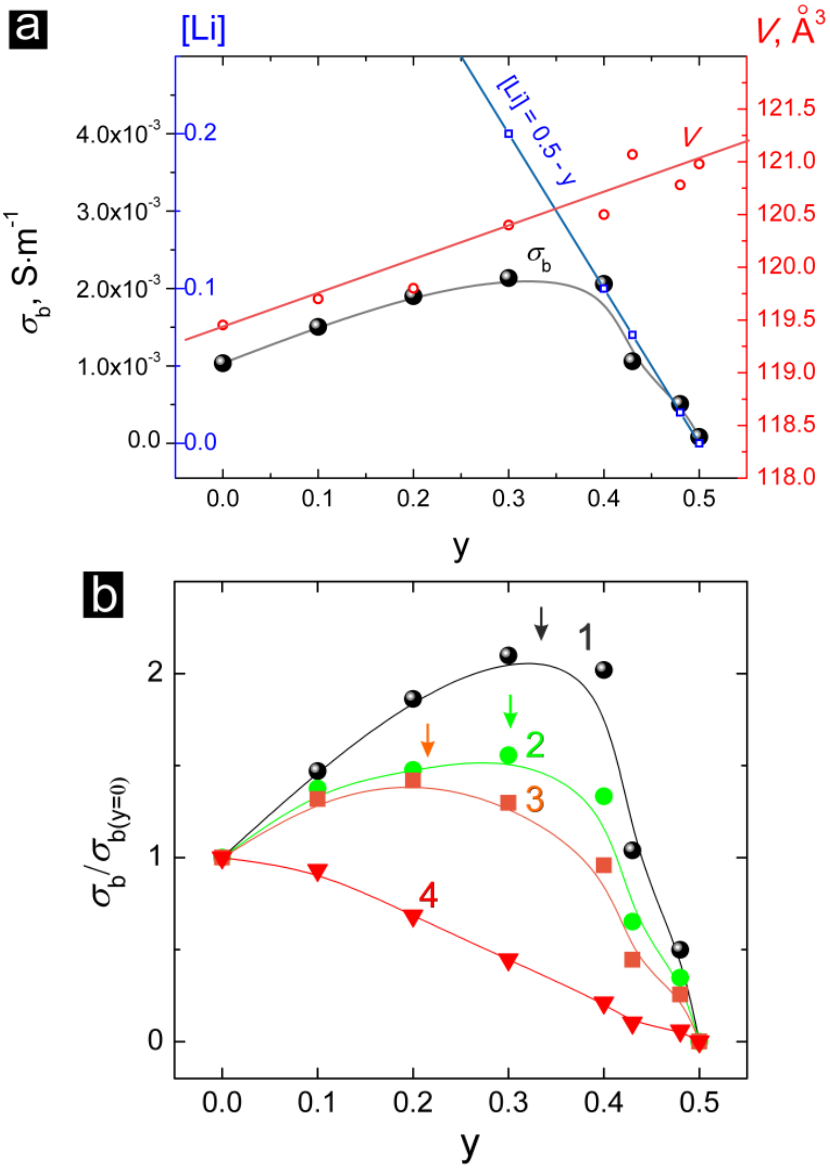

Fig. 3.36. Concentration dependences of $Li_{0.5-y}Na_yLa_{0.5}Nb_2O_6$ ceramics bulk conductivity at 300 K a). Behaviour of the bulk conductivity can be explained by lattice volume increase and charge carrier concentration decrease with increasing stoichiometric factor y b). Dependence of normalized conductivity of $Li_{0.5-y}Na_yLa_{0.5}Nb_2O_6$ ceramics at different temperatures: 300 K (1), 400 K (2), 500 K (3), 800 K (4). Arrows show conductivity maxima, which shifts towards lower y values when temperature increases.

In order to describe non-Arrhenius conductivity behaviour the theory proposed in [444] has been applied. The temperature dependent conductivity in the whole temperature range can be expressed as:

$$\sigma_{\mathrm{b}} \cdot T = \frac{A_{\sigma T}\sqrt{T^2-(\Delta\tilde{E}\Delta\tilde{Z}/\mathrm{R})^2}}{T} \exp\left(-\frac{\tilde{E}_0\tilde{Z}_0/\mathrm{R}}{T-\Delta\tilde{E}\Delta\tilde{Z}/\mathrm{R}}\right), \qquad (3.3)$$

where $\tilde{E}$ is the bond energy between the mobile and the surrounding ion, $\tilde{Z}$ is the coordination number of the mobile ion, R is the gas constant, $\tilde{E}_0$ and $\tilde{Z}_0$ are the mean values of $\tilde{E}$ and $\tilde{Z}$, $\Delta\tilde{E}$ and $\Delta\tilde{Z}$ are their fluctuations and $A_{\sigma T} = g\nu(Ze)^2 l^2\,[\mathrm{Li}^+]/\mathrm{Fk_B}$, where g is geometrical factor, ν - oscillation frequency, l – jump distance and F – correlation factor. By appropriately choosing the parameters provided formula describes temperature dependence of conductivity of both the Arrhenius type and the Vogel–Fulcher–Tammann type. The parameters obtained from the experimental data fitting to formula (3.3) are presented in Table 3.8 and Fig. 3.37 shows the fitting result. One can see from Fig. 3.37 that the tendency of the fitted results is the same as given experimentally and demonstrated in Fig. 3.35: the lowest conductivity value in all temperature range corresponds to the stoichiometric factor y = 0.5, the highest conductivity value at 300 K temperature was found for composition with stoichiometric factor y = 0.3, and the activation energy remains constant in the whole temperature interval only for the stoichiometric factor y = 0.

Table 3.8. Parameters of the model for non-Arrhenius temperature dependence of ion conductivity of $Li_{0.5-y}Na_yLa_{0.5}Nb_2O_6$ determined following [444].

Chemical composition (y)	$\tilde{E}_0\tilde{Z}_0/R$ (K)	$\Delta\tilde{E}\Delta\tilde{Z}/R$ (K)	$\log A_{\sigma T}$ ($\mathrm{S\cdot K\cdot cm^{-1}}$)
0	5885(96)	0	9.96(4)
0.1	5038(113)	8 (4)	9.60(5)
0.2	4204(139)	36(6)	9.09(6)
0.3	3501(120)	60(6)	8.58(6)
0.4	2830(78)	83(5)	7.90(4)
0.43	2814(71)	82(4)	7.55(4)
0.48	2832(73)	84(4)	7.34(4)
0.50	2791(88)	91(5)	6.63(5)

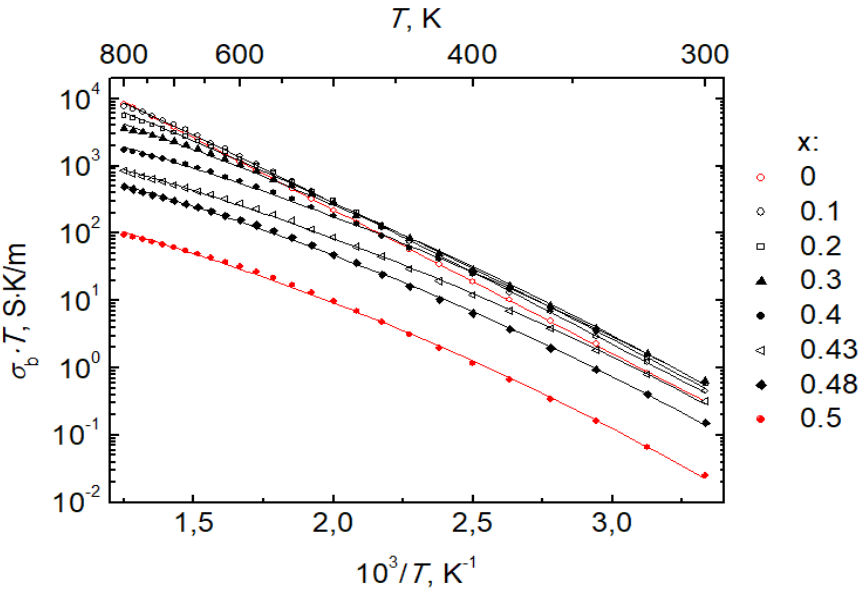

Fig. 3.37. Arrhenius plot of $Li_{0.5-y}Na_yLa_{0.5}Nb_2O_6$ ceramics bulk conductivity. The fits to the equation (3.3) are shown as solid lines. Note that the conductivity is multiplied by temperature in this graph.

Authors [444] have shown, that for the system with low value of the fluctuation $\Delta\tilde{E}\Delta\tilde{Z}/\mathrm{R}$, the model reduces to the Arrhenius-type behaviour. In fact, for the compound with y = 0 the best fitted value of $\Delta\tilde{E}\Delta\tilde{Z}/\mathrm{R}$ was 0 and this shows the pure lithium compound to obey Arrhenius behaviour. It is also worth noting, that in the 2D conduction region ($0 < y \leq 0.3$) the fitting parameters change significantly, while in the 3D conduction region the differences only for the preexponential factor are observed.

Since the conductivity is a product of charge (e), charge carrier concentration (n) and mobility (μ) it can be expressed as:

$$\sigma = en\mu \tag{3.4}$$

As according to the chemical formula lithium concentration in $Li_{0.5-y}Na_yLa_{0.5}Nb_2O_6$ changes proportionally to (0.5–y), dividing bulk conductivity by lithium amount in the formula we will get a quantity, which is proportional to the mobility of lithium ions. Composition dependences of $\sigma_b/(0.5–y)$ are presented in Fig. 3.38.

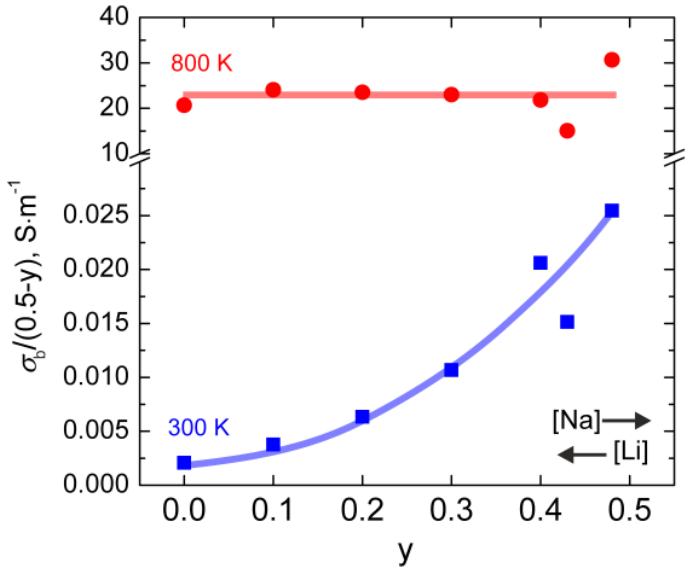

Fig. 3.38. Graph showing lithium mobility (see text) dependence on stoichiometric factor y at different temperatures. Arrows point out the increase of Na^+ and Li^+ concentrations in $Li_{0.5-y}Na_yLa_{0.5}Nb_2O_6$ ceramics, solid lines are guides for the eye.

At high temperature (i.e. 800 K) the mobility of lithium ions is the same for all compositions and the conductivity depends only on lithium concentration. Close to the room temperature the behaviour is different and lithium mobility significantly increases with increasing sodium fraction in the sample, so, as also discussed above, the conductivity at 300 K is determined by the mobility and lithium ion concentration.

At room temperature the maximum of conductivity as a function of sodium concentration in the system $Li_{0.5-y}Na_yLa_{0.5}Nb_2O_6$ can be explained by two competing effects, the one being the unit cell parameter change and the other – the change of mobile charge carriers. The increase of conductivity with increasing y (Fig. 3.36a) is due to the increase of unit cell volume as can be seen from Table 3.6 and Table 3.7. This, in accordance with [336], leads to the increase of bottleneck size and consequently to the conductivity increases and the activation energy decreases. With the further exchange of lithium by sodium ($y > 0.4$) the conductivity decreases because of significant decrease of charge carrier concentration, while charge carriers in this system are lithium-ions.

In order to find out the influence of the above mentioned factors on conductivity at elevated temperatures, the conductivity has been normalized to the value found for $y = 0$ and the normalized conductivity was studied as a

function of lithium concentration (Fig. 3.36b). As can be seen from the figure, with the temperature increase the maximum of conductivity becomes less pronounced and totally disappears at $T \geq 800$ K. However, the unit cell volume increases with temperature linearly (Table 3.6 and Table 3.7). So we can conclude, that at 800 K the bottleneck size increases so much, that it stops limiting lithium mobility. Thus at high temperatures the change of unit cell parameters caused by lithium to sodium substitution does not affect the conductivity. The concentration dependencies of conductivity are affected only by lithium ion concentration, which is lowered when lithium is substituted by sodium. Consequently at 800 K $Li_{0.5-y}Na_yLa_{0.5}Nb_2O_6$ conductivity gradually lowers with the increase of y.

The potential barrier for lithium jumps is determined by the bottleneck size, which originates from structural features of the lattice and it increases with the expansion of unit cell when lithium is partially replaced by sodium. With the temperature increase the energy of thermal oscillations are supposed to increase significantly with regard to potential barrier for lithium-ion jumps. So the temperature dependences of conductivity at higher temperatures are determined by the lithium ion concentration rather than by the structural features of the lattice.

CONCLUSIONS

1. The temperature dependence of $Na_2MnP_2O_7$ ceramics total conductivity suggested the phase transition taking place in this compound at 660 K. This phase transition has been approved by DTA and thermal XRD investigation.
2. The non-Arrhenius decrease of conductivity was observed on heating $Na_2MnP_2O_7$ ceramics up to 370 K, $Na_2ZnP_2O_7$ ceramics up to 340 K, $Na_2Zn_{0.5}Mn_{0.5}P_2O_7$ ceramics up to 360 K, and $NaCsZn_{0.5}Mn_{0.5}P_2O_7$ up to 420 K. The reverse process was found on cooling suggesting the water absorption from ambient air. It was shown, that a very small amount of water in the sodium-based pyrophosphates (about 0.5 wt.%) affects their room temperature conductivity, which must be mixed Na^+ and H^+ (protonic) at the same time.
3. It was revealed by the X-ray diffraction analysis that the $Na_2Zn_{0.5}Mn_{0.5}P_2O_7$ powder synthesized by the solid state reaction is a mixed phase compound, which consists of $Na_2MnP_2O_7$ and $Na_2ZnP_2O_7$ phases. In the temperature interval from 360 to 700 K the total electrical conductivity of $Na_2Zn_{0.5}Mn_{0.5}P_2O_7$ increases with temperature according to the Arrhenius law, but the activation energy change was found at about 630 K. This change was associated with the structural phase transition taking place in the $Na_2MnP_2O_7$ phase.
4. X-ray diffraction analysis showed that $NaCsZn_{0.5}Mn_{0.5}P_2O_7$ powder is a mixed phase compound, which consists of $NaCsZnP_2O_7$, $NaCsMnP_2O_7$ and $Cs_2MnP_4O_{12}$ phases. The anomalous changes of lattice parameters with temperature were observed from XRD spectra in the temperature region 400–500 K for $NaCsMnP_2O_7$ and 500–600 K for $Cs_2MnP_4O_{12}$. Additionally, the impedance spectroscopy analysis showed the changes of activation energy of the total electrical conductivity at temperatures 480 K and 590 K. It was proposed that detected anomalies of electrical properties are caused by structural disordering in the $NaCsMnP_2O_7$ and $Cs_2MnP_4O_{12}$ lattices.
5. The XRD measurements showed that $NaLiMnP_2O_7$ solid solution consists of two phases: $Na_2Mn_3(P_2O_7)_2$ and $LiMnPO_4$. Thermal XRD investigation suggested the phase transition taking place in

$Na_2Mn_3(P_2O_7)_2$ compound at about 800 K. This phase transition has been approved by DTA and the temperature dependence of $NaLiMnP_2O_7$ ceramics total ionic conductivity.

6. Manganese atoms' multi-valency (Mn^{2+}, Mn^{3+} and Mn^{4+} valence states) effect revealed by XPS analysis in $Na_2Zn_{0.5}Mn_{0.5}P_2O_7$ compound can determine high redox potentials within it suggesting sodium-based manganese pyrophosphates as very favourable cathodic materials for solid state battery applications.
7. Non-Arrhenius temperature dependencies of grain conductivity were found for $Li_{0.5-y}Na_yLa_{0.5}Nb_2O_6$ ceramics except for the $Li_{0.5}La_{0.5}Nb_2O_6$ compound. At lower temperatures $Li_{0.2}Na_{0.3}La_{0.5}Nb_2O_6$ compound shows the conductivity maximum, which can be explained by changes of lattice parameters and consequently the bottleneck size for Li^+-ion migration and also by charge carrier concentration. At 800 K lithium mobility in the system was found to be independent on stoichiometric factor y and the conductivity decreases monotonously when Li is replaced by Na.

REFERENCES

[1] M. Wakihara, Recent Developments in Lithium Ion Batteries, Materials Science and Engineering R33, 109-134 (2001).

[2] J. G. Kim, B. Son, S. Mukherjee, N. Schuppert, A. Bates, O. Kwon, M. J. Choi, H. Y. Chung and S. Park, A Review of Lithium and Non-Lithium Based Solid State Batteries, Journal of Power Sources 282, 299-322 (2015).

[3] J. M. Tarascon and M. Armand, Issues and Challenges Facing Rechargeable Lithium Batteries, Nature 414(6861), 359-367 (2001).

[4] K. Xu, Nonaqueous Liquid Electrolytes for Lithium-Based Rechargeable Batteries, Chemical Reviews 104(10), 4303-4417 (2004).

[5] Cymbet Corporation, Rechargeable Energy Storage Device: 5μAh, 3.8V (a booklet), (2012).

[6] M. Park, X. Zhang, M. Chung, G. B. Less and A. M. Sastry, A Review of Conduction Phenomena in Li-ion Batteries, Journal of Power Sources 195(24), 7904-7929 (2010).

[7] M. J. G. Jak, F. G. B. Ooms, E. M. Kelder, W. J. Legerstee, J. Schoonman and A. Weisenburger, Dynamically Compacted All-Ceramic Lithium-Ion Batteries, Journal of Power Sources 80(1-2), 83-89 (1999).

[8] P. G. Bruce, Solid-State Chemistry of Lithium Power Sources, Chemical Communications 19, 1817-1824 (1997).

[9] S. P. Ong, V. L. Chevrier, G. Hautier, A. Jain, C. Moore, S. Kim, X. Ma and G. Ceder, Voltage, Stability and Diffusion Barrier Differences Between Sodium-Ion and Lithium-Ion Intercalation Materials, Energy & Environmental Science 4(9), 3680-3688 (2011).

[10] N. Yabuuchi, K. Kubota, M. Dahbi and S. Komaba, Research Development on Sodium-Ion Batteries, Chemical Reviews 114(23), 11636–11682 (2014).

[11] F. Risacher and B. Fritz, Origin of Salts and Brine Evolution of Bolivinian and Chilean Salars, Aquatic Geochemistry 15(1), 123-157 (2009).

[12] A. Yaksic and J. E. Tilton, Using the Cumulative Availability Curve to Assess the Threat of Mineral Depletion: the Case of Lithium, Resources Policy 34(4), 185-194 (2009).

[13] H. Vikstrom, S. Davidsson and M. Hook, Lithium Availability and Future Production Outlooks, Applied Energy 110, 252-266 (2013).

[14] M. S. Islam and C. A. J. Fisher, Lithium and Sodium Battery Cathode Materials: Computational Insights into Voltage, Diffusion and Nanostructural properties, Chemical Society Reviews 43(1), 185-204 (2014).

[15] Y. Wang, B. Liu, Q. Li, S. Cartmell, S. Ferrara, Z. D. Deng and J. Xiao, Lithium and Lithium Ion Batteries for Applications in Microelectronic Devices: A Review, Journal of Power Sources 286, 330-345 (2015).

[16] N. Nitta, F. Wu, J. T. Lee and G. Yushin, Li-ion Battery Materials: Present and Future, Materials Today 18(5), 252-264 (2015).

[17] K. Ozawa, Lithium-Ion Rechargeable Batteries With $LiCoO_2$ and Carbon

Electrodes: the $LiCoO_2$/C System, Solid state Ionics 69(3-4), 212-221 (1994).

[18] R. Yazami, R. Lebrun, M. Bonneau and M. Molteni, High Performance $LiCoO_2$ Positive Electrode Material, Journal of Power Sources 54(2), 389-392 (1995).

[19] T. Ohzuku, A. Ueda, M. Nagayama, Y. Iwakoshi and H. Komori, Comparative Study of $LiCoO_2$, $LiNi_{12}Co_{12}O_2$ and $LiNiO_2$ for 4 Volt Secondary Lithium Cells, Electrochimica Acta 38(9), 1159-1167 (1993).

[20] J. W. Fergus, Recent Developments in Cathode Materials for Lithium Ion Batteries, Journal of Power Sources 195, 939-954 (2010).

[21] G. G. Armatucci, J. M. Tarascon and L. C. Klein, Cobalt Dissolution in $LiCoO_2$-Based Non-Aqueous Rechargeable Batteries, Solid State Ionics 83(1-2), 167-173 (1996).

[22] J. Molenda, Electronic Aspect of Intercalation in Layered, Spinel and Olivine Type Cathode Materials, Polish Journal of Chemistry 78(9), 1413-1421 (2004).

[23] K. A. Striebel, C. Z. Deng, S. J. Wen and E. J. Cairns, Electrochemical Behavior of $LiMn_2O_4$ and $LiCoO_2$ Thin Films Produced with Pulsed Laser Deposition, Journal of the Electrochemical Society 143(6), 1821-1827 (1996).

[24] J. Xie, N. Imanishi, M. Matsumura, Y. Takeda and O. Yamamoto, Kinetics Investigation of a Preferential (104) Plane Oriented $LiCoO_2$ Thin Film Prepared by RF Magnetron Sputtering, Solid State Ionics 178(19-20), 1218-1224 (2007).

[25] S. R. Das, S. B. Majumder and R. S. Katiyar, Kinetic Analysis of the Li^+ Ion Intercalation Behavior of Solution Derived Nano-Crystalline Lithium Manganate Thin Films, Journal of Power Sources 139(1), 261-268 (2005).

[26] H. Yue, X. K. Huang, D. P. Lv and Y. Yang, Hydrothermal Synthesis of $LiMn_2O_4$/C Composite as a Cathode for Rechargeable Lithium-Ion Battery with Excellent Rate Capability, Electrochimica Acta 54(23), 5363-5367 (2009).

[27] D. Shu, K. Y. Chung, W. I. Cho and K. B. Kim, Electrochemical Investigations on Electrostatic Spray Deposited $LiMn_2O_4$ Films, Journal of Power Sources 114(2), 253-263 (2003).

[28] M. Whittinghan, Lithium Batteries and Cathode Materials, Chemical Reviews 104(10), 4271-4301 (2004).

[29] J. Marzec, K. Swierczek, J. Przewoznik, J. Molenda, D. R. Simon, E. M. Kelder and J. Schoonman, Conduction Mechanism in Operating a $LiMn_2O_4$ Cathode, Solid State Ionics 146(3-4), 225-237 (2002).

[30] J. Molenda and W. Kucza, Transport Properties of $LiMn_2O_4$, Solid State Ionics 117(1-2), 41-46 (1999).

[31] H. Huang, S. C. Yin and L. F. Nazar, Approaching Theoretical Capacity of $LiFePO_4$ at Room Temperature at High Rates, Electrochemical and Solid State Letters 4(10), A170-A172 (2001).

[32] S. Yang, I. Song, K. Ngala, P. I. Zavalij and M. S. Whittingham, Performance

of $LiFePO_4$ as Lithium Battery Cathode and Comparison, Juornal of Power Sources 119-121, 239-246 (2003).

[33] Y. Fang, J. Zhang, L. Xiao, X. Ai, Y. Cao and H. Yang, Phosphate Framework Electrode Materials for Sodium Ion Batteries, Advanced Science 4(5), 1600392 (2017).

[34] S. I. Moon, J. U. Kim, B. O. Jin, Y. E. Hyung, M. S. Yun, H. B. Gu and Y. Ko, Characterization of TiS_2 Composite Cathodes with Solid Polymer Electrolyte, Journal of Power Sources 68(2), 660-663 (1997).

[35] B. Yan, X. Li, Z. Bai, M. Li, L. Dong, D. Xiong and D. Li, Superior Lithium Storage Performance of Hierarchical Porous Vanadium Pentoxide Nanofibers for Lithium Ion Battery Cathodes, Journal of Alloys and Compounds 634, 50-57 (2015.)

[36] A. Ullah, A. Majid and N. Rani, A Review on First Principles Based Studies for Improvement of Cathode Material of Lithium Ion Batteries, Journal of Energy Chemistry 27(1), 219-237 (2018).

[37] A. Patil, V. Patil, D. V. Shin, J. W. Choi, D. S. Paik and S. J. Yoon, Issue and Challenges Facing Rechargeable Thin Film Lithium Batteries, Materials Research Bulletin 43, 1913-1942 (2008).

[38] C. Liu, Z. G. Neale and G. Cao, Understanding Electrochemical Potentials of Cathode Materials in Rechargeable batteries, Materials Today 19(2), 109-123 (2016).

[39] T. Zhang, D. Li, Z. Tao and J. Chen, Understanding Electrode Materials of Rechargeable Lithium Batteries via DFT Calculations, Progress in Natural Science: Materials International 23(3), 256-272 (2013).

[40] A. Unemoto, H. Ogawa, I. Gambe and I. Honma, Development ofLithium Sulfur Batteries Using Room Temperature Ionic Liquid-Based Quasi Solid State Electrolytes, Electrochimica Acta 125, 386-394 (2014).

[41] Z. Takehara, Future Prospects of the Lithium Metal Anode, Journal of Power Sources 68(1), 82-86 (1997).

[42] U. von Sacken, E. Nodwell, A. Sundher and J. R. Dahn, Comparative Thermal Stability of Carbon Intercalation Anodes and Lithium Metal Anodes for Rechargeable Lithium Batteries, Journal of Power Sources 54(2), 240-245 (1995).

[43] D. Fauteux and R. Koksbang, Rechargeable Lithium Battery Anodes: Alternatives to Metallic Lithium, Journal of Applied Electrochemistry 23(1), 1-10 (1993).

[44] P. Hartmann, T. Leichweiss, M. R. Busche, M. Schneider, M. Reich, J. Sann, P. Adelhelm and J. Janek, Degradation of NASICON-Type Materials in Contact with Lithium Metal: Formation of Mixed Conducting Interphases (MCI) on Solid electrolytes, The Journal of Physical Chemistry C 117, 21064-21074 (2013).

[45] N. Takami, K. Hoshina and H. Inagaki, Lithium Diffusion in $Li_{4/3}Ti_{5/3}O_4$ Particles During Insertion and Extraction, Journal of the Electrochemical Society 158(6), A725-A730 (2011).

[46] F. Wunde, F. Berkemeier and H. Schmitz, Lithium Diffusion in Sputter-Deposited $Li_4Ti_5O_{12}$ Thin Films, Journal of Power Sources 215, 109-115 (2012).

[47] T. Hang, D. Mukoyama, H. Nara, N. Takami, T. Momma and T. Osaka, Electrochemical Impedance Spectroscopy Analysis for Lithium-Ion Battery Using $Li_4Ti_5O_{12}$ Anode, Journal of Power Sources 222, 442-447 (2013).

[48] P. P. Prosini, R. Mancini, L. Petrucci, V. Contini and P. Villano, $Li_4Ti_5O_{12}$ as Anode in All-Solid-State, Plastic, Lithium-Ion Batteries for Low-Power Applications, Solid State Ionics 144(1-2), 185-192 (2001).

[49] Y. J. Gu, Z. Guo and H. Q. Liu, Structure and Electrochemical Properties of $Li_4Ti_5O_{12}$ with Li Excess as Anode Electrode Material for Li-Ion Batteries, Electrochymica Acta 123, 576-581 (2014).

[50] M. Wilkening, R. Amade, W. Iwaniak and P. Heitjans, Ultraslow Li Diffusion in Spinel-Type Structured $Li_4Ti_5O_{12}$—A Comparison of Results from Solid State NMR and Impedance Spectroscopy, Physical Chemistry Chemical Physics 9(10), 1239-1246 (2007).

[51] P. Schichtel, M. Geiß, T. Leichtweiß, J. Sann, S. A. Weber and J. Janek, On the Impedance and Phase Transition of Thin Film All-Solid-State Batteries Based on the $Li_4Ti_5O_{12}$ System, Journal of Power Sources 360, 593-604 (2017).

[52] M. Kotobuki, The Current Situation and Problems of Rechargeable Lithium Ion, The Open Electrochemistry Journal 4, 28-35 (2012).

[53] E. Frackowiak and F. Beguin, Electrochemical Storage of Energy in Carbon Nanotubes and Nanostructured Carbons, Carbon 40(10), 1775-1787 (2002).

[54] J. L. Tirado, Inorganic Materials for the Negative Electrode of Lithium-Ion Batteries: State-of-the-Art and Future Prospects, Materials Science and Engineering: Reports 40(3), 103-136 (2004).

[55] N. A. Kaskhedikar and J. Maier, Lithium Storage in Carbon Nanostructures, Advanced Materials 21(25-26), 2664-2680 (2009).

[56] M. M. Doeff, Y. Ma, S. J. Visco and L. C. D. Jonghe, Electrochemical Insertion of Sodium into Carbon, Journal of The Electrochemical Society 140(12), L169–L170 (1993).

[57] D. A. Stevens and J. R. Dahn, The Mechanisms of Lithium and Sodium Insertion in Carbon Materials, Journal of The Electrochemical Society 148(8), A803-A811 (2001).

[58] Y. P. Wu, E. Rahm and R. Holze, Carbon Anode Materials for Lithium Ion Batteries, Journal of Power Sources 114(2), 228-236 (2003).

[59] M. D. Levi and D. Aurbach, Diffusion Coefficients of Lithium Ions during Intercalation into Graphite Derived from the Simultaneous Measurements and Modeling of Electrochemical Impedance and Potentiostatic Intermittent Titration Characteristics of Thin Graphite Electrodes, The Journal of Physical Chemistry B 101(23), 4641–4647 (1997).

[60] E. Markevich, M. D. Levi and D. Aurbach, Comparison Between Potentiostatic and Galvanostatic Intermittent Titration Techniques for

Determination of Chemical Diffusion Coefficients in Ion-Insertion Electrodes, Journal of Electroanalytical Chemistry 580(2), 231-237 (2005).

[61] K. Persson, V. A. Sethuraman, L. J. Hardwick, Y. Hinuma, Y. S. Meng, A. van der Ven, V. Srinivasan, R. Kostecki and G. Ceder, Lithium Diffusion in Graphitic Carbon, The Journal of Physical Chemistry Letters 1(8), 1176–1180 (2010).

[62] Y. Qi, H. Guo, L. G. Hector Jr. and A. Timmons, Threefold Increase in the Young's Modulus of Graphite Negative Electrode during Lithium Intercalation, Journal of the Electrochemical Society 157(5), A558-A566 (2010).

[63] I. A. Udod, H. B. Orman and V. K. Genchel, The Sodium-Graphite System under High-Pressure Conditions: The Comparison with the Lithium-Graphite System, Carbon 32(1), 101-106 (1994).

[64] M. Noel and V. Suryanarayanan, Role of Carbon Host Lattices in Li-Ion Intercalation/De-Intercalation Processes, Journal of Power Sources 111(2), 193-209 (2004).

[65] Y. Baskin and L. Meyer, Lattice Constants of Graphite at Low Temperatures, Physical Review 100(2), 544 (1955).

[66] H. Azuma, H. Imoto, S. Yamada and K. Sekai, Advanced Carbon Anode Materials for Lithium Ion Cells, Journal of Power Sources 81-82, 1-7 (1999).

[67] S. A. Safran and D. R. Hamann, Long-Range Elastic Interactions and Staging in Graphite Intercalation Compounds, Physical Review Letters 42(21), 1410-1413 (1979).

[68] M. D. Levi, D. Aurbach and J. Maier, Electrochemically Driven First-Order Phase Transitions Caused by Elastic Responses of Ion-Insertion Electrodes under External Kinetic Control, Journal of Electroanalytical Chemistry 624(1-2), 251-261 (2008).

[69] M. D. Levi, E. Markevich and D. Aurbach, Comparison between Cottrell Diffusion and Moving Boundary Models for Determination of the Chemical Diffusion Coefficients in Ion-Insertion Electrodes, Electrochimica Acta 51(1), 98-110 (2005).

[70] P. R. Wallace, The Band Theory of Graphite, Physical Review 71(9), 622-634 (1947).

[71] J. Y. Hwang, S. T. Myung and Y. K. Sun, Sodium-Ion Batteries: Present and Future, Chemical Society Reviews 46(12), 3529-3614 (2017).

[72] T. D. Hatchard and J. R. Dahn, In Situ XRD and Electrochemical Study of the Reaction of Lithium with Amorphous Silicon, Journal of the Electrochemical Society 151(6), A838-A842 (2004).

[73] R. Chandrasekaran, A. Magasinski, G. Yushin and T. F. Fuller, Analysis of Lithium Insertion/Deinsertion in a Silicon Electrode Particle at Room Temperature, Journal of the Electrochemical Society 157(10), A1139-A1151 (2010).

[74] N. Ding, J. Xu, Y. X. Yao, G. Wegner, X. Fang, C. H. Chen and I. Lieberwirth, Determination of the Diffusion Coefficient of Lithium Ions in

nano-Si, Solid State Ionics 180(2-3), 222-225 (2009).

[75] J. Xie, N. Imanishi, T. Zhang, A. Hirano, Y. Takeda and Y. Yamamoto, Li-ion Diffusion in Amorphous Si Films Prepared by RF Magnetron Sputtering: A Comparison of Using Liquid and Polymer Electrolytes, Materials Chemistry and Physics 120(2-3), 421-425 (2010).

[76] M. Pharr, K. Zhao, X. Wang, Z. Suo and J. J. Vlassak, Kinetics of Initial Lithiation of Crystalline Silicon Electrodes of Lithium-Ion Batteries, Nano Letters 12(9), 5039–5047 (2012).

[77] J. Chen, Recent Progress in Advanced Materials for Lithium Ion Batteries, Materials 6, 156-183 (2013).

[78] C. S. Wang, G. T. Wu, X. B. Zhang, Z. F. Qi and W. Z. Li, Lithium Insertion in Carbon-Silicon Composite Materials Produced by Mechanical Milling, The Electrochemical Society 145(8), 2751-2758 (1998).

[79] C. K. Chan, R. Ruffo, S. S. Hong, R. A. Huggins and Y. Cui, Structural and Electrochemical Study of the Reaction of Lithium with Silicon Nanowires, Journal of Power Sources 189(1), 34-39 (2009).

[80] L. Baggetto and P. H. L. Nottena, Lithium-Ion (De)Insertion Reaction of Germanium Thin-Film Electrodes: An Electrochemical and In Situ XRD Study, Journal of the Electrochemical Society 156(3), A169-A175 (2009).

[81] B. Laforge, L. L. Jodin, R. Salot and A. Billard, Study of Germanium as Electrode in Thin-Film Battery, Journal of the Electrochemical Society 155(2), A181-A188 (2008).

[82] A. M. Chockla, K. C. Klavetter, C. B. Mullins and B. A. Korgel, Solution-Grown Germanium Nanowire Anodes for Lithium-Ion Batteries, ACS Applied Materials and Interfaces 4(9), 4658-4664 (2012).

[83] V. Thangadurai and W. Weppner, Recent Progress in Solid Oxide and Lithium Ion Conducting Electrolytes Research, Ionics 12(1), 81-92 (2006).

[84] A. Manthiram, X. Yu and S. Wang, Lithium Battery Chemistries Enabled by Solid-State Electrolytes, Nature Reviews Materials 2(16103), 1-16 (2017).

[85] R. C. Agrawal and G. P. Pandey, Solid Polymer Electrolytes: Materials Designing and All-Solid-State Battery Applications: An Overview, Journal of Physics D: Applied Physics 41, 1-18 (2008).

[86] P. Knauth, Inorganic Solid Li Ion Conductors: An Overview, Solid State Ionics 180, 911-916 (2009).

[87] B. L. Ellis and L. F. Nazar, Sodium and Sodium-Ion Energy Storage Batteries, Current Opinion in Solid State and Materials Science 16(4), 168-177 (2012).

[88] M. Gellert, K. I. Gries, C. Yada, F. Rosciano, K. Volz and B. Roling, Grain Boundaries in a Lithium Aluminum Titanium Phosphate-Type Fast Lithium Ion Conducting Glass Ceramic: Microstructure and Nonlinear Ion Transport Properties, Juornal of Physical Chemistry C 116(43), 22675-22678 (2012).

[89] R. Muragan, V. Thangadurai and W. Weppner, Fast Lithium Ion Conduction in Garnet-Type $Li_7La_3Zr_2O_{12}$, Angewandte Chemie International Edition 46(41), 7778-7781 (2007).

[90] R. Murugan, W. Weppner, P. S. Beurnmann and V. Thangadurai, Structure and Lithium Ion Conductivity of Bismuth Containing Lithium Garnets $Li_5La_3Bi_2O_{12}$ and $Li_6SrLa_2Bi_2O_{12}$, Materials Science and Engineering B 143, 14-20 (2007).

[91] H. Xia, H. L. Wang, W. Xiao, M. O. Lai and L. Lu, Thin Film Li Electrolytes for All-Solid-State Micro-batteries, International Journal of Surface Science and Engineering 3, 23-43 (2009).

[92] N. J. Dudney, Thin Film Micro-Batteries, Electrochemical Society Interface 17(3), 44-48 (2008).

[93] P. P. Kumar and S. Yashonath, Ionic Conduction in the Solid State, Journal of Chemical Sciences 118(1), 135-154 (2006).

[94] Z. Jian, Y. S. Hu, X. Ji and W. Chen, NASICON-Structured Materials for Energy Storage, Advanced Materials 29(1601925) 2017.

[95] N. Anantharamulu, K. Koteswara Rao, G. Rambabu, B. Vijaya Kumar, V. Radha and V. Vithal, A Wide-Ranging Review on Nasicon Type Materials, Journal of Material Sciences 46(9), 2121-2837 (2011).

[96] L. O. Hagman and P. Kierkegaard, The Crystal Structure of $NaMe_2^{IV}(PO_4)_3$; Me^{IV} = Ge, Ti, Zr, Acta Chemica Scandinavica 22, 1822-1832 (1968).

[97] H. Y. P. Hong, Crystal Structures and Crystal Chemistry in the System $Na_{1+x}Zr_2Si_xP_{3-x}O_{12}$, Materials Research Bulletin 11(2), 173-182 (1976).

[98] L. Sebastian and J. Gopalakrishnan, Lithium Ion Mobility in Metal Oxides: A Materials Chemistry Perspective, Journal of Materials Chemistry 13(3), 433-441 (2003).

[99] J. W. Fergus, Ion Transport in Sodium Ion Conducting Solid Electrolytes, Solid State Ionics 227, 102-112 (2012).

[100] P. Yadav and M. C. Bhatnagar, Structural Studies of NASICON Material of Different Compositions by Sol-Gel Method, Ceramics International 38, 1731-1735 (2012).

[101] O. Bohnke, R. Ronchetti and D. Mazza, Conductivity Measurements on Nasicon and Nasicon-Modified Materials, Solid State Ionics 122, 127-136 (1999).

[102] E. Traversa, H. Aono, Y. Sadaoka and L. Montanaro, Electrical Properties of Sol–Gel Processed NASICON Having New Compositions, Sensors and Actuators B 65, 204-208 (2000).

[103] F. Lalere, J. B. Leriche, M. Courty, S. Boulineau, V. Viallet, C. Masquelier and V. Seznec, An All-Solid State NASICON Sodium Battery Operating at 200 °C, Journal of Power Sources 247, 975-980 (2014).

[104] W. Hou, X. Guo, X. Shen, K. Amine, H. Yu and J. Lu, Solid Electrolytes and Interfaces in All-Solid-State Sodium Batteries: Progress and Perspective, Nano Energy 52, 279-291 (2018).

[105] F. Sudreau, D. Petit and J. P. Boilot, Dimorphism, Phase Transitions, and Transport Properties in $LiZr_2(PO_4)_3$, Journal of Solid State Chemistry 83(1), 78-90 (1989).

[106] M. Catti, S. Stramare and R. Ibberson, Lithium Location in NASICON-Type Li^+ Conductors by Neutron Diffraction. I. Triclinic α'-$LiZr_2(PO_4)_3$, Solid State Ionics 123(1), 173-180 (1999).

[107] M. Catti and S. Stramare, Lithium Location in NASICON-type Li^+ Conductors by Neutron Diffraction. II. Rhombohedral α-$LiZr_2(PO_4)_3$ at *T*=423 K, Solid State Ionics 136(1-2), 489-494 (2000).

[108] M. A. Subramanian, R. Subramanian and A. Clearfield, Lithium Ion Conductors in the Systems $AB(IV)_2(PO_4)_3$ (B = Ti, Zr and Hf), Solid State Ionics 18-19, 562-569 (1986).

[109] A. B. Bykov, A. P. Chirkin, L. N. Deyanets, S. N. Doronin, E. A. Genkina, A. K. Ivanov-Shits, I. P. Kondratyuk, B. A. Maksimov, O. K. Mel'Nikov, L. N. Muradyan, V. I. Simonov and V. A. Tomofeeva, Superionic Conductors $Li_3M_2(PO_4)_3$ (M = Fe, Sc, Cr): Synthesis, Structure and Electrophysical Propeties, Solid State Ionics 38(1-2), 31-52 (1990).

[110] H. Aono, N. Imanaka and G. Adachi, High Li^+ Conducting Ceramics, Accounts of Chemical Research 27(9), 265-270 (1994).

[111] A. F. Orliukas, O. Bohnke, A. Kezionis, S. Kazlauskas, V. Venckute, D. Petrulionis, T. Zukauskas, T. Salkus, A. Dindune, Z. Kanepe, J. Ronis and V. Kunigelis, Broadband Impedance Spectroscopy of Some Li^+ and V** Conducting Solid Electrolytes, Advanced Electromagnetics 1(1), 70-75 (2012).

[112] H. Aono, E. Sugimoto, Y. Sadaoka, N. Imanaka and G. Adachi, Ionic Conductivity of the Lithium Titanium Phosphate $(Li_{1+X}M_XTi_{2-X}(PO_4)_3$, (M = Al, Sc, Y, and La) Systems, Journal of the Electrochemical Society 136(2), 590-591 (1988).

[113] H. Aono, E. Sugimoto, Y. Sadaoka, N. Imanaka and G. Adachi, Ionic Conductivity of Solid Electrolytes Based on Lithium Titanium Phosphate, Journal of the Electrochemical Society 137(4), 1023-1027 (1990).

[114] H. Aono, E. Sugimoto, Y. Sadaoka, N. Imanaka and G. Adachi, Ionic Conductivity and Sinterability of Lithium Titanium Phosphate System, Solid State Ionics 40(1), 38-42 (1990).

[115] A. Kezionis and A. F. Orliukas, Electrical Properties of $Li_{1.2}Sc_{0.2}Ti_{1.8}(PO_4)_3$ Ceramics in the Frequency Range from 10^6 to $1.2x10^9$ Hz, Lithuanian Journal of Physics 38(3), 298-301 (1998).

[116] R. Sobiestianskas, A. Dindune, Z. Kanape, J. Ronis, A. Kezionis, E. Kazakevicius and A. F. Orliukas, Electrical Properties of $Li_{1+x}Y_yTi_{2-y}(PO_4)_3$ (where x, y = 0.3; 0.4) Ceramics at High Frequencies, Materials Science and Engineering B 76(3), 184-192 (2000).

[117] R. Sobiestianskas, A. Kezionis, E. Kazakevicius and A. F. Orliukas, Synthesis and Transport Properties of $Li_{1.3}M_{0.3}Ti_{1.7}(PO_4)_3$ (where M = Al, Fe) Ceramics, Lithuanian Journal of Physics 40(1-3), 183-188 (2000).

[118] A. Kezionis, E. Kazakevicius and A. Orliukas, The Influence of Substitution Between $Ti^{4+} \rightarrow Sc^{3+}(B^{3+})+Li^+$ on Electric Properties of $Li_{1+x+y}Sc_xB_yTi_{2-x-y}(PO_4)_3$, where (x = 0.3, y = 0; x = 0.2, y = 0.1) Superionic Ceramics,

Lithuanian Journal of Physics 41(4-6), 335-338 (2001).

[119] A. Dindune, E. Kazakevicius, Z. Kanape, J. Ronis, A. Kezionis and A. F. Orliukas, Relationships Between Substitutions $Ti^{4+} \rightarrow Sc^{3+}(B^{3+})+Li^{+}$ and Ionic Conductivity of $Li_{1+x+y}Sc_xB_yTi_{2-x-y}(PO_4)_3$, (where x, y = 0 - 0,3) Ceramics, Phosphorus Research Bulletin 13, 107-110 (2002).

[120] A. Dindune, Z. Kanape, E. Kazakevicius, A. Kezionis, J. Ronis and A. F. Orliukas, Synthesis and Electrical Properties of $Li_{1+x}M_xTi_{2-x}(PO_4)_3$ (where M = Sc, Al, Fe, Y; x = 0.3) Superionic Ceramics, Journal of Solid State Electrochemistry 7(2), 113-117 (2003).

[121] A. F. Orliukas, A. Dindune, Z. Kanape, J. Ronis, E. Kazakevicius and A. Kezionis, Synthesis, Structure and Pecularities of Ionic Transport of $Li_{1.6}Mg_{0.3}Ti_{1.7}(PO_4)_3$ Ceramics, Solid State Ionics 157, 177-181 (2003).

[122] S. C. Li and Z. X. Lin, Phase Relationships and Ionic Conductivity of $Li_{1+x}Ti_{2-x}In_xP_3O_{12}$, Solid State Ionics 9-10(2), 835-838 (1983).

[123] S. Hamdoune and D. T. Qui, Ionic Conductivity and Crystal Structure of $Li_{1+x}Ti_{2-x}In_xP_3O_7$, Solid State Ionics 18-19(1), 587-591 (1986).

[124] Z. X. Lin, H. J. Yu, S. C. Li and S. B. Tian, Phase Relationship and Electrical Conductivity of $Li_{1+x}Ti_{2-x}Ga_xP_3O_{12}$ and $Li_{1+2x}Ti_{2-x}Mg_xP_3O_{12}$, Solid State Ionics 18-19(1), 549-552 (1986).

[125] K. Arbi, M. A. Paris and J. Sanz, Lithium Exchange Processes in the Conduction Network of the Nasicon $LiTi_{2-x}Zr_x(PO_4)_3$ Series ($0 \leq x \leq 2$), The Journal of Physical Chemistry B 110(13), 6454-6457 (2006).

[126] H. Aono, E. Sugimoto, Y. Sadaoka, N. Imanaka and G. Adachi, Electrical Property and Sinterability of $LiTi_2(PO_4)_3$ Mixed with Lithium Salt (Li_3PO_4 or Li_3BO_3), Solid State Ionics 47(3-4), 257-264 (1991).

[127] J. Fu, Fast Li^{+} Ion Conduction in Li_2O-Al_2O_3-TiO_2-SiO_2-P_2O_5 Glass-Ceramics, Journal of the American Ceramic Society 80(7), 1901-1903 (1997).

[128] Y. Meesala, A. Jena, H. Chang and R. S. Liu, Recent Advancements in Li-Ion Conductors for All-Solid-State Li-Ion Batteries, ACS Energy Letters 2(12), 2734−2751 (2017).

[129] M. Forsyth, S. Wong, K. M. Nairn, A. S. Best, P. J. Newman and D. R. Macfarlane, NMR Studies of Modified Nasicon-Like, Lithium Conducting Solid Electrolytes, Solid State Ionics 124(3-4), 213-219 (1999).

[130] A. S. Best, M. Forsyth and D. R. MacFarlane, Stoichiometric Changes in Lithium Conducting Materials Based on $Li_{1+x}Al_xTi_{2-x}(PO_4)_3$: Impedance, X-ray and NMR studies, Solid State Ionics 136-137, 339-344 (2000).

[131] K. Arbi, S. Mandal, J. M. Rojo and J. Sanz, Dependence of Ionic Conductivity on Composition of Fast Ionic Conductors $Li_{1+x}Ti_{2-x}Al_x(PO_4)_3$, $0 \leq x \leq 0.7$. A Parallel NMR and Electric Impedance Study, Chemistry of Materials 14(3), 1091-1097 (2002).

[132] X. M. Wu, X. H. Li, Y. H. Zhang, M. F. Xu and Z. Q. He, Synthesis of $Li_{1.3}Al_{0.3}Ti_{1.7}(PO_4)_3$ by Sol-Gel Technique, Materials Letters 58(7-8), 1227-1230 (2004).

[133] K. Arbi, M. Tabellout, M. G. Lazarraga, J. M. Rojo and J. Sanz, Non-Arrhenius Conductivity in the Fast Lithium Conductor $Li_{1.2}Ti_{1.8}Al_{0.2}(PO_4)_3$: A Li NMR and Electric Impedance Study, Physical Review B 72(9), 094302.1-094302.8 (2005).

[134] C. M. Chang, Y. I. Lee and S. H. Hong, Spark Plasma Sintering of $LiTi_2(PO_4)_3$-Based Solid Electrolytes, Journal of the American Ceramic Society 88(7), 1803-1807 (2005).

[135] K. Arbi, J. M. Rojo and J. Sanz, Lithium Mobility in Titanium Based Nasicon $Li_{1+x}Ti_{2-x}Al_x(PO_4)_3$ and $LiTi_{2-x}Zr_x(PO_4)_3$ Materials Followed by NMR and Impedance Spectroscopy, Journal of the European Ceramic Society 27(13), 4215-4218 (2007).

[136] X. Xu, Z. Wen, J. Wu and X. Yang, Preparation and Electrical Properties of NASICON-Type Structured $Li_{1.4}Al_{0.4}Ti_{1.6}(PO_4)_3$ Glass-Ceramics by the Citric Acid-Assisted Sol–Gel Method, Solid State Ionics 178(1), 29-34 (2007).

[137] M. Pang, R. Suzuki, M. Saito and K. Machida, Fabrication and Crystal Line Pattering of $Li_{1.3}Al_{0.3}Ti_{1.7}(PO_4)_3$ Ion Conductive Glass by Ni Atom Heat Processing Method, Applied Physics Letters 92(4), 041112.1-041112.3 (2008).

[138] X. Wu, R. Li, S. Chen, Z. He and M. Ma, Sol-Gel Preparation and Characterization of $Li_{1.3}Al_{0.3}Ti_{1.7}(PO_4)_3$ Sintered with Flux of $LiBO_2$, Rare Metals 29(5), 515-518 (2010).

[139] X. M. Wu, J. L. Liu, R. X. Li, S. Chen and M. Y. Ma, Preparation and Characterization of $LiMn_2O_4/Li_{1.3}Al_{0.3}Ti_{1.7}(PO_4)_3/LiMn_2O_4$ Thin-Film Battery by Spray Technique, Russian Journal of Electrochemistry 47(8), 917-922 (2011).

[140] A. Dindune, A. Kezionis, Z. Kanape, R. Sobiestianskas, E. Kazakevičius and A. Orliukas, Fabrication and Electric Properties of Solid Electrolyte $Li_{1.3}Al_{0.3-y}Y_yTi_{1.7}(PO_4)_3$ (where y = 0; 0.15) Ceramics, in Materials Engineering-99, Kaunas (1999).

[141] E. Kazakevicius, A. F. Orliukas, A. Kezionis, L. Jucius, A. Dindune, Z. Kanape and J. Ronis, Synthesis and Electrical Properties of $Li_{1+x}Zr_{2-2x}Al_xTi_x(PO_4)_3$ Superionic Ceramics, Materials Science 10(4), 363-365 (2004).

[142] E. Kazakevicius, A. Urcinskas, B. Bagdonas, A. Kezionis, A. F. Orliukas, A. Dindune, Z. Kanape and J. Ronis, Electrical Properties of $Li_{1.3}M_{1.4}Ti_{0.3}Al_{0.3}(PO_4)_3$ (M = Ge, Zr) Superionic Ceramics, Lithuanian Journal of Physics 45(4), 267-272 (2005).

[143] A. F. Orliukas, A. Dindune, Z. Kanape, J. Ronis, B. Bagdonas and A. Kezionis, Synthesis and Peculiarities of Electric Properties of $Li_{1.3}Zr_{1.4}Ti_{0.3}Al_{0.3}(PO_4)_3$ Solid Electrolyte Ceramics, Electrochimica Acta 51(27), 6194-6198 (2006).

[144] E. Kazakevicius, A. Urcinskas, A. Kezionis, A. Dindune, Z. Kanepe and J. Ronis, Electrical Properties of $Li_{1.3}Ge_{1.4}Ti_{0.3}Al_{0.3}(PO_4)_3$ Superionic Ceramics, Electrochimica Acta 51(27), 6199-6202 (2006).

[145] E. Kazakevicius, T. Salkus, A. Selskis, A. Selskiene, A. Dindune, Z. Kanape,

J. Ronis, J. Miskinis, V. Kazlauskiene, V. Venckute, A. Kezionis and A. F. Orliukas, Preparation and Characterization of $Li_{1+x}Al_ySc_{x-y}Ti_{2-x}(PO_4)_3$ (x = 0.3, y = 0.1, 0.15, 0.2) Ceramics, Solid State Ionics 188(1), 73-77 (2011).

[146] A. F. Orliukas, T. Salkus, A. Kezionis, A. Dindune, Z. Kanepe, J. Ronis, V. Venckute, V. Kazlauskiene, J. Miskinis and A. Lukauskas, Structure and Broadband Impedance Spectroscopy of $Li_{1.3}Al_yY_{x-y}Ti_{1.7}(PO_4)_3$ (x = 0.3; y = 0.1, 0.2) Solid Electrolyte Ceramics, Solid State Ionics 225, 620-625 (2012).

[147] S. C. Li, J. Y. Cai and Z. X. Lin, Phase Relationships and Electrical Conductivity of $Li_{1+x}Ge_{2-x}Al_xP_3O_{12}$ and $Li_{1+x}Ge_{2-x}Cr_xP_3O_{12}$ Systems, Solid State Ionics 28-30, 1265-1270 (1988).

[148] M. Cretin and P. Fabry, Comparative Study of Lithium Ion Conductors in the System $Li_{1+x}Al_xA_{2-x}^{IV}(PO_4)_3$ with A^{IV}=Ti or Ge and $0 \leq x \leq 0.7$ for Use as Li^+ Sensitive Membranes, Journal of the European Ceramic Society 19(16), 2931-2940 (1999).

[149] P. Maldonado-Manso, M. C. Martin-Sedeno, S. Bruque, J. Sanz and E. R. Losilla, Unexpected Cationic Distribution in Tetrahedral/Octahedral Sites in Nominal $Li_{1+x}Al_xGe_{2-x}(PO_4)_3$ NASICON series, Solid State Ionics 178(1-2), 43-52 (2007).

[150] A. Dindune, Z. Kanape and J. Ronis, Synthesis, Structure and Electric Properties of Solid Electrolyte $Li_{1.5}Ge_{1.5}Al_{0.5}(PO_4)_3$, $Li_{1.3}Ge_{1.7}Cr_{0.3}(PO_4)_3$, in Materials of the 10th International Baltic Conference, Riga (2001).

[151] J. Fu, Fast Li^+ Ion Conducting Glass-Ceramics in the System $Li_2O–Al_2O_3–GeO_2–P_2O_5$, Solid State Ionics 104(3-4), 191-194 (1997).

[152] X. Xu, Z. Wen, X. Wu, X. Yang and Z. Gu, Lithium Ion-Conducting Glass–Ceramics of $Li_{1.5}Al_{0.5}Ge_{1.5}(PO_4)_{3-x}Li_2O$ (x=0.0–0.20) with Good Electrical and Electrochemical Properties, Journal of the American Ceramic Society 90(9), 2802-2806 (2007).

[153] C. J. Leo, B. V. R. Chowdari, G. V. Subba Rao and J. L. Souquet, Lithium Conducting Glass Ceramic with Nasicon Structure, Materials Research Bulletin 37(8), 1419-1430 (2002).

[154] P. Maldonado-Manso, E. R. Losilla, M. Martinez-Lara, M. A. G. Aranda, S. Bruque, F. E. Mouhid and M. Zahir, High Lithium Ionic Conductivity in the $Li_{1+x}Al_xGe_yTi_{2-x-y}(PO_4)_3$, Chemistry of Materials 15(9), 1879-1885 (2003).

[155] J. S. Thokchom, N. Gupta and B. Kumar, Superionic Conductivity in a Lithium Aluminum Germanium Phosphate Glass–Ceramic, Journal of the Electrochemical Society 155(12), A915-A920 (2008).

[156] X. Xu, Z. Wen, Z. Gu, X. Xu and Z. Lin, Lithium Ion Conductive Glass Ceramics in the System $Li_{1.4}Al_{0.4}(Ge_{1-x}Ti_{x)1.6}(PO_4)_3$ (x=0–1.0), Solid State Ionics 171(3-4), 207-213 (2004).

[157] X. X. Xu, Z. Y. Wen, Z. H. Gu and Z. X. Lin, High Lithium Conductivity in $Li_{1.3}Cr_{0.3}Ge_{1.7}(PO_4)_3$, Materials Letters 58(27-28), 3428-3431 (2004).

[158] M. Illbeigi, A. Fazlali, M. Kazazi and A. H. Mohammadi, Effect of Simultaneous Addition of Aluminum and Chromium on the Lithium Ionic Conductivity of $LiGe_2(PO_4)_3$ NASICON-type Glass–Ceramics, Solid State

Ionics 289, 180-187 (2016).

[159] J. K. Feng, L. Lu and M. O. Lai, Lithium Storage Capability of Lithium Ion Conductor $Li_{1.5}Al_{0.5}Ge_{1.5}(PO_4)_3$, Journal of Alloys and Compounds 501(2), 255-258 (2010).

[160] G. B. Kunshina, I. V. Bocharova and V. I. Ivanenko, Preparation of the $Li_{1.5}Al_{0.5}Ge_{1.5}(PO_4)_3$ Solid Electrolyte with High Ionic Conductivity, Inorganic Materials: Applied Research 8(2), 238-244 (2017).

[161] S. S. Berbano, J. Guo, H. Guo, M. T. Lanagan and C. A. Randall, Cold Sintering Process of $Li_{1.5}Al_{0.5}Ge_{1.5}(PO_4)_3$ Solid Electrolyte, Journal of the American Ceramic Society 100(5), 2123-2135 (2017).

[162] E. Zhao, F. Ma, Y. Guo and Y. Jin, Stable LATP/LAGP Double-Layer Solid Electrolyte Prepared via a Simple Dry-Pressing Method for Solid State Lithium Ion Batteries, RSC Advances 6(95), 92579-92585 (2016).

[163] H. M. Kasper, Series of Rare Earth Garnets $Ln^{3+}{}_3M_2Li^{+}{}_3O_{12}$ (M=Te, W), Inorganic chemistry 8(4), 1000-1002 (1969).

[164] M. Kotobuki, H. Munakata, K. Kanamura, Y. Sato and T. Yoshida, Compatibility of $Li_7La_3Zr_2O_{12}$ Solid Electrolyte to All-Solid-State Battery Using Li Metal Anode, Journal of The electrochemical Society 157(10), A1076-A1079 (2010).

[165] S. Teng, J. Tan and A. Tiwari, Recent Developments in Garnet Based Solid State Electrolytes for Thin Film Batteries, Current Opinion in Solid State and Materials Science 18(1), 29-38 (2014).

[166] A. F. Wells, Structural Inorganic Chemistry, 4th ed., Oxford: Clarendon Press (1975).

[167] V. Thangadurai, S. Narayanan and D. Pinzaru, Garnet-Type Solid-State Fast Li Ion Conductors for Li Batteries: Critical Review, Chemical Society Reviews 43, 4714-4727 (2014).

[168] F. Zheng, M. Kotobuki, S. Song, M. O. Lai and L. Lu, Review on Solid Electrolytes for All Solid State Lithium-Ion Batteries, Journal of Power Sources 389, 198-213 (2018).

[169] C. A. Geiger, E. Alekseev, B. Lazic, M. Fisch, T. Armbruster, R. Langner, M. Fechtelkord, N. Kim, T. Pettke and W. Weppner, Crystal Chemistry and Stability of "$Li_7La_3Zr_2O_{12}$" Garnet: A Fast Lithium-Ion Conductor, Inorganic Chemistry 50(3), 1089-1097 (2011).

[170] S. Ohta, T. Kobayashi and T. Asaoka, High Lithium Ionic Conductivity in the Garnet-Type Oxide $Li_{7-X}La_3(Zr_{2-X}Nb_X)O_{12}$ (x = 0-2), Journal of Power Sources 196(6), 3342-3345 (2011).

[171] Y. Li, J. T. Han, C. A. Wang, H. Xie and J. B. Goodenough, Optimizing Li^+ Conductivity in a Garnet Framework, Journal of Materials Chemistry 22, 15357–15361 (2012).

[172] L. Buannic, B. Orayech, J. M. López Del Amo, J. Carrasco, N. A. Katcho, F. Aguesse, W. Manalastas, W. Zhang, J. Kilner and A. Llordés, Dual Substitution Strategy to Enhance Li^+ Ionic Conductivity in $Li_7La_3Zr_2O_{12}$ Solid Electrolyte, Chemistry of Materials 29(4), 1769–1778 (2017).

[173] G. Larraz, A. Orera and M. L. Sanjuan, Cubic Phases of Garnet-Type $Li_7La_3Zr_2O_{12}$: The Role of Hydration, Journal of Materials Chemistry A 1(37), 11419-11428 (2013).

[174] W. Xia, B. Xu, H. Duan, X. Tang, Y. Guo, H. Kang, H. Li and H. Liu, Reaction Mechanisms of Lithium Garnet Pellets in Ambient Air: The effect of Humidity and CO_2, Journal of the American Ceramic Society 100(7), 2832-2839 (2017).

[175] M. D. Graef and M. E. McHenry, Structure of Materials: An Introduction to Crystallography, Diffraction and Symmetry, 2nd ed., Cambridge University Press (2012).

[176] I. Inaguma, C. Liquan, M. Itoh, T. Nakamura, T. Uchida, H. Ikuta and M. Wakihara, High Ionic Conductivity in Lithium Lanthanum Titanate, Solid State Communications 86(10), 689-693 (1993).

[177] I. Inaguma and M. Nakashima, A Rechargeable Lithium–Air Battery Using a Lithium Ion-Conducting Lanthanum Lithium Titanate Ceramics as an Electrolyte Separator, Journal of Power Sources 228, 250-255 (2013).

[178] A. Mei, X. L. Wang, J. L. Lan, Y. C. Feng, H. X. Geng, Y. H. Lin and C. W. Nan, Role of Amorphous Boundary Layer in Enhancing Ionic Conductivity of Lithium-Lantanum-Titanate Electrolyte, Electrochimica Acta 55(8), 2958-2963 (2010).

[179] Y. Inaguma, L. Chen, M. Itoh and T. Takamura, Candidate Compounds with Perovskite Structure for High Lithium Ionic Conductivity, Solid state Ionics 70-71(1), 196-202 (1996).

[180] R. Inada, K. Kimura, K. Kusakabe, T. Tojo and Y. Sakurai, Synthesis and Lithium-Ion Conductivity for Perovskite-Type $Li_{3/8}Sr_{7/16}Ta_{3/4}Zr_{1/4}O_3$ Solid Electrolyte by Powder-Bed Sintering, Solid State Ionics 261, 95-99 (2014).

[181] B. Huang, B. Xu, Y. Li, W. Zhou, Y. You, S. Shong, C. Wang and J. B. Goodenough, Li-Ion Conduction and Stability of Perovskite $Li_{3/8}Sr_{7/16}Hf_{1/4}Ta_{3/4}O_3$, ACS Applied Materials & Interfaces 8(23), 14552-14557 (2016).

[182] H. P. Hong, Crystal Structure and Ionic Conductivity of $Li_{14}Zn(GeO_4)_4$ and Other New Li^+ Superionic Conductors, Materials Research Bullentin 13(2), 117-124 (1978).

[183] D. Mazumdar, D. N. Bose and M. L. Mukherjee, Transport and Dielectric Properties of Lisicon, Solid State Ionics 14(2), 143-147 (1984).

[184] S. Song, J. Lu, F. Zheng, H. M. Duong and L. Lu, A Facile Strategy to Achieve High Conduction and Excellent Chemical Stability of Lithium Solid Electrolytes, RSC Advances 5(9), 6588-6594 (2015).

[185] J. B. Bates, N. J. Dudney, G. R. Gruzalski, R. A. Zuhr, A. Choudhury, C. F. Luck and J. D. Robertson, Fabrication and Characterization of Amorphous Lithium Electrolyte Thin Films and Rechargeable Thin-Film Batteries, Journal of Power Sources 43(1-3), 103-110 (1993).

[186] Y. Su, J. Falgenhauer, A. Polity, T. Leichtweiß, A. Kronenberger, J. Obel, S. Zhou, D. Schlettwein, J. Janek and B. K. Meyer, LiPON Thin Films with High

Nitrogen Content for Application in Lithium Batteries and Electrochromic Devices Prepared by RF Magnetron Sputtering, Solid State Ionics 282, 63-69 (2015).

[187] L. Van-Yoden, A. Claudel, C. Secouard, F. Sabary, J. P. Barnes and S. Martin, Role of the Chemical Composition and Structure on the Electrical Properties of a Solid State Electrolyte: Case of a Highly Conductive LiPON, Electrochimica Acta 259, 742-751 (2018).

[188] T. Fujibayashi, Y. Kubota, K. Iwabuchi and N. Yoshii, Highly Conformal and High-Ionic Conductivity Thin-Film Electrolyte for 3D-Structured Micro Batteries: Characterization of LiPON Film Deposited by MOCVD Method, AIP Advances 7, 085110 (2017).

[189] N. Suzuki, T. Inaba and T. Shiga, Electrochemical Properties of LiPON Films Made from a Mixed Powder Target of Li_3PO_4 and Li_2O, Thin Solid Films 520(6), 1821-1825 (2012).

[190] D. Kundu, E. Talaie, V. Duffort and L. F. Nazar, The Emerging Chemistry of Sodium Ion Batteries for Electrochemical Energy Storage, Angewandte Chemie Int. Ed., 54, 3431-3448 (2015).

[191] S. P. Guo, J. C. Li, Q. T. Xu, Z. Ma and H. G. Xue, Recent Achievements on Polyanion-Type Compounds for Sodium-Ion Batteries: Syntheses, Crystal Chemistry and Electrochemical Performance, Journal of Power Sources 361, 285-299 (2017).

[192] N. N. Greenwood and A. Earnshaw, Chemistry of the Elements, 2nd ed., Butterworth-Heinemann (1997).

[193] B. A. Boukamp and R. A. Huggins, Lithium Ion Conductivity in Lithium Nitride, Physics Letters A 58(4), 231-233 (1976).

[194] E. Doneges, Handbook of Preparative Inorganic Chemistry, 2nd ed., vol. 1, New York: Academic Press, p. 984 (1963).

[195] R. A. Huggins, Recent Results on Lithium Ion Conductors, Electrochimica Acta 22(7), 773-781 (1977).

[196] J. R. Rea, D. L. Foster, P. L. Mallory and I. Co, High Ionic Conductivity in Densified Polycrystalline Lithium Nitride, Materials Research Bulletin 14(6), 841-846 (1979).

[197] S. Hatake, J. Kuwano, M. Miyamori, Y. Saito and S. Koyama, New Lithium-Ion Conducting Compounds $3Li_3N$-MI (M = Li, Na, K, Rb) and Their Application to Solid-State Lithium-Ion Cells, Journal of Power Sources 68(2), 416-420 (1997).

[198] L. Zhan, Y. Zhang, X. Zhuang, H. Fang, Y. Zhu, X. Guo, J. Chen, Z. Wang and L. Li, Ionic Conductivities of Lithium Borohydride-Lithium Nitride Composites, Solid State Ionics 304, 150-155 (2017).

[199] R. Kanno and M. Murayama, Lithium Ionic Conductor Thio-LISICON: The Li_2S GeS_2 P_2S_5 System, Journal of the Electrochemical Society 148(7), A742-A746 (2001).

[200] M. Tatsumisago and A. Hayashi, Sulfide Glass-Ceramic Electrolytes for All-Solid-StateLithium and Sodium Batteries, International Journal of Applied

Glass Science 5(3), 226-235 (2014).

[201] N. Kamaya, K. Homma, Y. Yamakawa, M. Hirayama, R. Kanno, M. Yonemura, T. Kamiyama, Y. Kato, S. Hama, K. Kawamoto and A. Mitsui, A Lithium Superionic Conductor, Nature Materials 10, 682-686 (2011).

[202] Y. Kato, S. Hori, T. Saito, K. Suzuki, M. Hirayama, A. Mitsui, M. Yonemura, H. Iba and R. Kanno, High-Power All-Solid-State Batteries Using Sulfide Superionic Conductors, Nature Energy 1, 16030 (2016).

[203] Y. Seino, T. Ota, K. Takada, A. Hayashi and M. Tatsumisago, A Sulphide Lithium Super Ion Conductor is Superior to Liquid Ion Conductors for Use in Rechargeable Batteries, Energy and Environmental Science 7, 627-631 (2014).

[204] I. H. Chu, H. Nguyen, S. Hy, Y. C. Lin, Z. Wang, Z. Xu, Z. Deng, Y. S. Meng and S. P. Ong, Insights into the Performance Limits of the $Li_7P_3S_{11}$ Superionic Conductor: A Combined First-Principles and Experimental Study, ACS Applied Materials and Interfaces 8(12), 843–7853 (2016).

[205] C. Cao, Z. B. Li, X. L. Wang, X. B. Zhao and W. Q. Han, Recent Advantages in Inorganic Solid Electrolytes for Lithium Batteries, Frontiers in Energy Research 2(25), 1-10 (2014).

[206] R. P. Rao and S. Adams, Studies of Lithium Argyrodite Solid Electrolytes for All-Solid-State Batteries, Physica Status Solidi A 208(8), 1804-1807 (2011).

[207] C. Yu, L. Eijck, S. Ganapathy and M. Wagemaker, Synthesis, Structure and Electrochemical Performance of the Argyrodite, Electrochimica Acta 215, 93-99 (2016).

[208] H. J. Deiseroth, S. T. Kong, H. Eckert, J. Vannahme, C. Reiner, T. Zaiß and M. Schlosser, Li_6PS_5X: A Class of Crystalline Li-Rich Solids With an Unusually High Li^+ Mobility, A Journal of the German Chemical Society 47(4), 755-758 (2008).

[209] V. Epp, Ö. Gün, H. J. Deiseroth and M. Wilkening, Highly Mobile Ions: Low-Temperature NMR Directly Probes Extremely Fast Li^+ Hopping in Argyrodite-Type Li_6PS_5Br, The Journal of Physical Chemistry Letters 4(13), 2118-2123 (2013).

[210] P. R. Rayavarapu, N. Sharma, V. K. Peterson and S. Adams, Variation in Structure and Li^+-Ion Migration in Argyrodite-Type Li_6PS_5X (X = Cl, Br, I) Solid Electrolytes, Journal of Solid State Electrochemistry 16(5), 1807-1813 (2012).

[211] S. Boulineau, M. Courty, J. M. Tarascon and V. Viallet, Mechanochemical Synthesis of Li-Argyrodite Li_6PS_5X (X = Cl, Br, I) as Sulfur-Based Solid Electrolytes for All Solid State Batteries Application, Solid state Ionics 221, 1-5 (2012).

[212] M. Chen, R. P. Rao and S. Adams, High Capacity All-Solid-State Cu–Li_2S/Li_6PS_5Br/In Batteries, Solid State Ionics 262, 183-187 (2014).

[213] Y. Zhao and L. Daemen, Superionic Conductivity in Lithium-Rich Anti-Perovskites, Journal of the American Chemical Society 134(36), 15042-15047 (2012).

[214] M. H. Braga, J. A. Ferreira, V. Stockhausen, J. E. Oliveira and A. E. Azab, Novel Li_3ClO Based Glasses with Superionic Properties for Lithium Batteries, Journal of Materials Chemistry A 2(15), 5470-5480 (2014).

[215] P. Barpanda, S. Nishimura and A. Yamada, High-Voltage Pyrophosphate Cathodes, Advances Energy Materials 2, 841-859 (2012).

[216] E. A. Genkina, B. A. Maximov, V. A. Tomofeeva, A. B. Bykov and O. K. Melnikov, Sintez i atomnoe stroenie novovo dvoinovo pirofosfata $LiFeP_2O_7$ (in Russian), Doklady Akademii Nauk SSSR 284, 864-867 (1985).

[217] D. Riou, N. Nguyen, R. Benloucif and B. Raveau, $LiFeP_2O_7$: Structure and Magnetic Properties, Materials Research Bulletin 25(11), 1363-1369 (1990).

[218] G. Vitins, Z. Kanepe, A. Vitins, J. Ronis, A. Dindune and A. Lusis, Structural and Conductivity Studies in $LiFeP_2O_7$, $LiScP_2O_7$, and $NaScP_2O_7$, Journal of Solid State Electrochemistry 4(3), 146-152 (2000).

[219] A. K. Padhi, K. S. Nanjundaswamy, C. Masquelier, S. Okada and J. B. Goodenough, Effect of Structure on the Fe^{3+}/Fe^{2+} Redox Couple in Iron Phosphates, Journal of the Electrochemical Society 144(5), 1609-1613 (1997).

[220] C. M. Julien, P. Jozwiak and J. Garbarczyk, Vibrational Spectroscopy of Electrode Materials for Rechargeable Lithium Batteries IV. Lithium Metal Phosphates, Conference: International Workshop on Advanced Techniques for Energy Sources Investigation and Testing, At Sofia, Bulgaria, L4.1-L4.12 (2004).

[221] C. Wurm, M. Morcrette, G. Rousse, L. Dupont and C. Masquelier, Lithium Insertion/Extraction into/from $LiMX_2O_7$ Compositions (M = Fe, V; X = P, As) Prepared via a Solution Method, Chemistry of Materials 14(6), 2701-2710 (2002).

[222] V. Venckute, J. Miskinis, V. Kazlauskiene, T. Salkus, A. Dindune, Z. Kanapec, J. Ronis, A. Maneikis, M. Lelis, A. Kezionis and A. F. Orliukas, XRD, XPS, SEM/EDX and Broadband Impedance Spectroscopy Study of Pyrophosphate ($LiFeP_2O_7$ and $Li_{0.9}Fe_{0.9}Ti_{0.1}P_2O_7$) ceramics, Phase Transitions 87(5), 438-451 (2014).

[223] C. V. Ramana, A. Ait-Salah, S. Utsunomiya, A. Mauger, F. Gendron and C. M. Julien, Novel Lithium Iron Pyrophosphate ($LiFe_{1.5}P_2O_7$) as a Positive Electrode for Li-Ion Batteries, Chemistry of Materials 19(22), 5319–5324 (2007).

[224] J. Zheng, Y. Han, L. Tang and B. Zhang, Investigation of Phase Structure Change and Electrochemical Performance in $LiVP_2O_7$-$Li_3V_2(PO_4)_3$-$LiVPO_4F$ system, Solid State Ionics 198, 195-202 (2016).

[225] K. H. Lii, Y. P. Wang, Y. B. Chen and S. L. Wang, The Crystal Structure of $LiVP_2O_7$, Journal of Solid State Chemistry 86(2), 143-148 (1990).

[226] H. Yu, Z. Su and L. Wang, Synthesis and Electrochemical Properties of $LiVP_2O_7$/C as Novel Cathode Material for Lithium Ion Batteries, Ceramics International 43(18), 17116-17120 (2017).

[227] I. V. Zatovskii, Sintez ta budova podbijnavadifosfatu $LiTiP_2O_7$ (in Ukrainian), Reports of the National Academy of Sciences of Ukraine 11, 129-133 (2008).

[228] Y. Uebou, S. Okada, M. Egashira and J. I. Yamaki, Cathode Properties of Pyrophosphates for Rechargabloe Lithium Batteries, Solid State Ionics 148(3-4), 323-328 (2002).

[229] S. Patoux and C. Masquelier, Lithium Insertion into Titanium Phosphates, Silicates and Sulfates, Chemistry of Materials 14, 5057-5068 (2002).

[230] J. Sanz and J. E. Iglesias, Structural Disorder in the Cubic 3 x 3 x 3 Superstructure of TiP_2O_7. XRD and NMR Study, Chemistry of Materials 9(4), 996-1003 (1997).

[231] C. H. Kim and H. S. Yim, The Effect of Tetravalent Metal on Dielectric Property in ZrP_2O_7 and TiP_2O_7, Solid State Communications 110(3), 137-142 (1999).

[232] S. T. Norberg, G. Svensson and J. Albertsson, A TiP_2O_7 Superstructure, Acta Crystallographica Section C 57(3), 225-227 (2001).

[233] Y. Uebou, S. Okada, M. Egashira and J. Yamaki, Synthesis, Structures, and Electrochemical Characteristics of Pyrophosphates, The Reports of Innstitute of Advanced Material Study, Kyushu University 15(1), 57-61 (2001).

[234] I. C. Marcu, J. M. Millet and J. M. Herrmann, Semiconductive and Redox Properties of Ti and Zr Pyrophosphate Catalysts (TiP_2O_7 and ZrP_2O_7). Consequences for the Oxidative Dehydrogenation of n-Butane, Catalysis Letters 78(1-4), 273-279 (2002).

[235] Z. Shi, Q. Wang, W. Ye, Y. Li and Y. Yang, Synthesis and Characterisation of Mesoporous Titanium Pyrophosphate as Lithium Intercalation Electrode Materials, Microporous and Mesoporous Materials 88(1-3), 232-237 (2006).

[236] H. Wang, K. Huang, Y. Zeng, S. Yang and L. Chen, Electrochemical Properties of TiP_2O_7 and $LiTi_2(PO_4)_3$ as Anode Material for Lithium Ion Battery with Aquaeous Solution Electrolyte, Electrochimica Acta 52(9), 3280-3285 (2007).

[237] V. Nalini, M. H. Sorby, K. Amazawa, R. Haugsrud, H. Fjellvag and T. Norby, Structure, Water Uptake, and Electrical Conductivity of TiP_2O_7, Journal of the American Ceramic Society 94(5), 1514-1522 (2011).

[238] V. Nalini, R. Haugsrud and T. Norby, High-Temperature Proton Conductivity and Defect Structure of TiP_2O_7, Solid State Ionics 181(11-12), 510-516 (2010).

[239] A. K. Rai, J. Lim, V. Mathew, J. Gim, J. Kang, B. J. Paul, D. Kim, S. Ahn, S. Kim, K. Ahn and J. Kim, Highly Reversible Capacity Nanocomposite Anode for Secondary Lithium-Ion Batteries, Electrochemistry Communications 19, 9-12 (2012).

[240] A. Oueslati, Li^+ Ion Conductivity and Transport Properties of $LiYP_2O_7$ Compound, Ionics 23(4), 857-867 (2016).

[241] S. Nasri, M. Megdiche and M. Gargouri, DC Conductivity and Study of AC Electrical Conduction Mechanisms by Non-Overlapping Small Polaron Tunneling Model in $LiFeP_2O_7$ ceramic, Ceramics International 42(1), 943-951 (2016).

[242] L. S. Ivashkevich, K. A. Selevich, A. I. Lesnikovich and A. F. Selevich,

Crystal Structure of $CrLiP_2O_7$ Determined from X-ray Powder Diffraction Data, Acta Crystallographica E 63(3), i70-i72 (2007).

[243] B. Babu, D. Bhuvaneswari and K. Nallathamby, Feasibility Studies on Newly Identified $LiCrP_2O_7$ Compound for Lithium Insertion Behavior, Applied Physics A 96(2), 489-493 (2009).

[244] E. Pachoud, W. Zhang, J. H. Tapp, K. C. Liang, B. Lorenz, P. C. V. Chu and S. Halasyamani, Top-Seeded Single-Crystal Growth, Structure, and Physical Properties of Polar $LiCrP_2O_7$, Crystal Growth Design 13, 5473-5480 (2015).

[245] M. Sassi, A. Bettaibi, A. Oueslati, K. Khirouni and M. Gargouri, Electrical Conduction Mechanism and Transport Properties of $LiCrP_2O_7$ Compound, Journal of Alloys and Compounds 649, 642-648 (2015).

[246] M. J. Mahesh, G. S. Gopalakrishna and K. G. Ashamanjari, Thermal, Magnetic and Impedance Properties of $Li_2M^{2+}P_2O_7$ (M^{2+} = Fe and Ni) Single Crystals, Materials Science in Semiconductor Processing 10, 117-123 (2007).

[247] S. Nishimura, M. Nakamura, R. Natsui and A. Yamada, New Lithium Iron Pyrophosphate as 3.5 V Class Cathode Material for Lithium Ion Battery, Journal of the American Chemical Society 132(39), 13596-13597 (2010).

[248] B. Zhang, X. Ou, J. C. Zheng, C. Shen, L. Ming, Y. D. Han, J. L. Wang and S. E. Qin, Electrochemical Properties of $Li_2FeP_2O_7$ Cathode Material Synthesized by Using Different Lithium Sources, Electrochimica Acta 133, 1-7 (2014).

[249] J. M. Clark, S. Nishimura, A. Yamada and M. S. Islam, High-Voltage Pyrophosphate Cathode: Insights into Local Stucture and Lithium-Diffusion Pathways, Angewandte Chemie Int. Ed., 51(52), 13149-13153 (2012).

[250] T. Ye, P. Barpanda, S. Nishimura, N. Furuta, S. C. Chung and A. Yamada, General Observation of Fe^{3+}/Fe^{2+} Redox Couple Close to 4 V in Partially Substituted $Li_2FeP_2O_7$ Pyrophosphate Solid-Solution Cathodes, Chemistry of Materials 25(18), 3623-3629 (2013).

[251] M. Tamaru, S. C. Chung, D. Shimizu, S. Nishimura and A. Yamada, Pyrophosphate Chemistry toward Safe Rechargeable Chemistry, Chemistry of Materials 25, 2538-2543 (2013).

[252] P. Barpanda, T. Ye, S. C. Chung, Y. Yamada, S. Nishimura and A. Yamada, Eco-Efficient Splash Combustion Synthesis of Nanoscale Pyrophosphate, Journal of Materials Chemistry 22, 13455-13459 (2012).

[253] T. F. Yi, X. Y. Li, H. Liu, J. Shu, Y. R. Zhu and R. S. Zhu, Recent Developments in the Doping and Surface Modification of $LiFePO_4$ as Cathode Material for Power Lithium Ion Battery, Ionics 18(6), 529-539 (2012).

[254] L. Adam, A. Guesdon and B. Raveau, A New Lithium Manganese Phosphate with an Original Tunnel Structure in the $A_2MP_2O_7$ Family, Journal of Solid State Chemistry 181, 3110-3115 (2008).

[255] S. Nishimura, R. Natsui and A. Yamada, A New Polymorph of Lithium Manganese(II) Pyrophosphate β-$Li_2MnP_2O_7$, Dalton transactions 43, 1502-1504 (2014).

[256] M. Tamaru, P. Barpanda, Y. Yamada, S. Nishimura and A. Yamada,

Observation of the Highest Mn^{3+}/Mn^{2+} Redox Potential of 4.45 V in a $Li_2MnP_2O_7$ Pyrophosphate Cathode, Journal of Materials Chemistry 22(47), 24526-24529 (2012).

[257] H. Kim, S. Lee, Y. U. Park, H. Kim, J. Kim, S. Jeon and K. Kang, Neutron and X-ray Diffraction Study of Pyrophosphate-Based $Li_{2-x}MP_2O_7$ (M = Fe, Co) for Lithium Rechargeable Battery Electrodes, Chemistry of Materials 23(17), 3930–3937 (2011).

[258] M. R. Spirlet, J. Rebizant and M. Liegeois-Duyckaerts, Structure of Lithium Copper Pyrophosphate, Acta Crystalographica C49, 209-211 (1993).

[259] G. S. Gopalakrishna, M. J. Mahesh, K. G. Ashamanjari and J. Shashidhara Prasad, Structure, Thermal and Magnetic Characterization of Hydrothermal Synthesized $Li_2CuP_2O_7$ Crystals, Materials Research Bulletin 43(5), 1171-1178 (2008).

[260] M. Krichen, M. Gargouri, K. Guidara and M. Megdiche, Phase Transition and Electrical Investigation in Lithium Copper Pyrophosphate Compound $Li_2CuP_2O_7$ Using Impedance Spectroscopy, Ionics 23(12), 3309-3322 (2017).

[261] D. Ozer, Z. Ertekin, K. Pekmez and N. A. Oztas, Fuel Effects on $Li_2CuP_2O_7$ Synthesized by Solution Combustion Method for Lithium-Ion Batteries, Ceramics International 45(4), 4626-4630 (2019).

[262] M. S. Kishore, V. Pralong, V. Caignaert, U. V. Varadaraju and B. Raveau, A New Lithium Vanadyl Diphosphate $Li_2VOP_2O_7$: Synthesis and Electrochemical Study, Solid State Sciences 10(10), 1285-1291 (2008).

[263] H. Zhou, S. Upreti, N. A. Chernova, G. Hautier, G. Ceder and M. S. Whittingham, Iron and Manganese Pyrophosphates as Cathodes for Lithium-Ion Batteries, Chemistry of Materials 23(2), 293-300 (2011).

[264] N. Furuta, S. Nishimura, P. Barpanda and A. Yamada, Fe^{3+}/Fe^{2+} Redox Couple Approaching 4 V in $Li_{2-x}(Fe_{1-y}Mn_y)P_2O_7$ Pyrophosphate Cathodes, Chemistry of Materials 24(6), 1055-1061 (2012).

[265] A. Yamada, Iron-Based Materials Strategies, Materials Research Society 39(5), 423-428 (2014).

[266] M. G. Robert, M. Goreaud, P. Labbe and B. Raveau, The Pyrophosphate $NaFeP_2O_7$: A Cage Structure, Journal of Solid State Chemistry 45(3), 389-395 (1982).

[267] T. M. Pizarro, R. Salmon, L. Fournes, G. Flem, B. Wanklyn and P. Hagenmuller, Etudes Cristallographique Magnétique et par Résonance Mössbauer de la Variété de Haute Température du Pyrophosphate $NaFeP_2O_7$, Journal of Solid State Chemistry 53(3), 387-397 (1984).

[268] J. L. Soubeyroux, R. Salmon, L. Fournes and G. Flem, Magnetic Properties of $NaFeP_2O_7$ Studied by Neutron Diffraction and Mössbauer Resonance Techniques, Physica B+C 136(1-3), 447-450 (1986).

[269] K. Byrappa, G. S. Gopalakrishna and B. V. Umesh Dutt, Morphology of New Superionic Pyrophosphates, Journal of Materials Science 27(16), 4439-4446 (1992).

[270] S. Nasri, M. Megdiche and M. Gargouri, AC Impedance Analysis, Equivalent

Circuit, and Modulus Behavior of $NaFeP_2O_7$ ceramic, Ionics 21(1), 67-78 (2015).

[271] A. Leclaire, A. Benmoussa, M. M. Borel, A. Grandin and B. Raveau, Two Forms of Sodium Titanium(III) Diphosphate: α-$NaTiP_2O_7$ Closely Related to β-Cristobalite and β-$NaTiP_2O_7$ Isotypic with $NaFeP_2O_7$, Journal of the Solid State Chemistry 77(2), 299-305 (1988).

[272] A. Leclaire, M. M. Borel, A. Grandin and B. Raveau, A Mo(III) Phosphate with a Cage Structure: $NaMoP_2O_7$, Journal of Solid State Chemistry 76(1), 131-135 (1988).

[273] Y. P. Wang, K. H. Lii and S. L. Wang, Structure of $NaVP_2O_7$, Acta Crystallographica C45, 1417-1418 (1989).

[274] K. H. Lii, Y. P. Wang, Y. B. Chen and S. L. Wang, The Crystal Structure of $LiVP_2O_7$, Journal of Solid State Chemistry 86(2), 143-148 (1990).

[275] M. J. Mahesh, G. S. Gopalakrishna and Ashamanjari, Pre-Treated and Treated Hydrothermal Preparation of $NaVP_2O_7 \cdot H_2O$ Crystalline Material and its Characterization, Materials Characterization 57(1), 30-35 (2006).

[276] Y. Kee, N. Dimov, A. Staikov, P. Barpanda, Y. C. Lu, K. Minami and S. Okada, Insight into the Limited Electrochemical Activity of $NaVP_2O_7$, RSC Advances 5(80), 64991-64996 (2015).

[277] R. V. Panin, O. A. Drozhzhin, S. Fedotov, A. A. Suchkova, N. R. Khasanova and E. V. Antipov, Pyrophosphates $AMoP_2O_7$ (A = Li and Na): Synthesis, Structure and Electrochemical Properties, Materials Research Bulletin 106, 170-175 (2018).

[278] A. Hamady and T. Jouini, $NaYP_2O_7$, Acta Crystallographica C52(12), 2949-2951 (1996).

[279] A. Oueslati and M. Gargouri, Impedance Spectroscopy and Conduction Mechanism of $NaYP_2O_7$ Ceramic Compound, Journal of Electroceramics 41(103), 1-7 (2018).

[280] Y. B. Taher, R. Hajji, A. Oueslati and M. Gargouri, Infra-Red, NMR Spectroscopy and Transport Properties of Diphosphate $NaAlP_2O_7$, Journal of Cluster Science 26(4), 1279–1294 (2015).

[281] F. Erragh, A. Boukhari, B. Elouadi and E. M. Holt, Crystal Structures of two Allotropic Forms of $Na_2CoP_2O_7$, Journal of Crystallographic and Spectroscopic Research 21(3), 321-326 (1991).

[282] F. Sanz, C. Parada, J. M. Rojo, C. Ruiz-Valero and R. Saez-Puche, Studies on Tetragonal $Na_2CoP_2O_7$, a Novel Ionic Conductor, Journal of Solid State Chemistry 145(2), 604-611 (1999).

[283] P. Barpanda, J. Lu, T. Ye, M. Kajiyama, S. C. Chung, N. Yabuuchi, S. Komaba and A. Yamada, A Layer-Structured $Na_2CoP_2O_7$ Pyrophosphate Cathode for Sodium-Ion Batteries, RSC Advances 3(12), 3857-3860 (2013).

[284] L. Benhamada, A. Grandin, M. M. Borel, A. Leclaire and B. Raveau, $Na_2VP_2O_8$: A Tetravalent Vanadium Diphosphate with a Layered Structure, Journal of Solid State Chemistry 101(1), 154-160 (1992).

[285] A. Daidouh, M. L. Veiga and C. Pico, New Polymorphs of $A_2VP_2O_8$ (A = Na, Rb), Solid State Ionics 106(1), 103-112 (1998).

[286] K. M. S. Etheredge and S. J. Hwu, Synthesis of a New Layered Sodium Copper(II) Pyrophosphate, $Na_2CuP_2O_7$, via an Eutectic Halide Flux, Inorganic Chemistry 34(6), 1495-1499 (1995).

[287] F. Erragh, A. Boukhari, F. Abraham and B. Elouadi, The Crystal Structure of α- and β-$Na_2CuP_2O_7$, Journal of Solid State Chemistry 120(1), 23-31 (1995).

[288] E. Hafidi, M. Omari, M. Omari, A. Bentayeb, J. Bennazha, A. Maadi and M. Chehbouni, Conductivity Studies of Some Diphosphates with the General Formula $A^{I}_2B^{II}P_2O_7$ by Impedance Spectroscopy, Arabian Journal of Chemistry 6(3), 253-263 (2013).

[289] F. Erragh, A. Boukhari, A. Sadel and E. M. Holt, Disodium Zinc Pyrophosphate and Disodium (Europium) Zinc Pyrophosphate, Acta Crystallographica Section C Crystal Structure Communications 54(10), 1373-1376 (1998).

[290] I. Belharouak, P. Gravereau, C. Parent, J. P. Chaminade, E. Lebraud and G. L. Flem, Crystal Structure of $Na_2ZnP_2O_7$: Reinvestigation, Journal of Solid State Chemistry 152(2), 466-473 (2000).

[291] Y. F. Shepelev, M. Petrova, A. S. Novikova and A. E. Lapshin, Crystal Structures of $Na_2ZnP_2O_7$, $K_2ZnP_2O_7$, and $LiKZnP_2O_7$ Phases in the M_2O-ZnO-P_2O_5 Glass-Forming System (M= Li, Na, and K), Glass Physics and Chemistry 28(5), 317-321 (2002).

[292] M. Madegowda, S. P. Madhu, B. H. Doreswamy, G. S. Gopalakrishna, M. A. Sridhar, S. P. Javaregowda and K. G. Ashamanjari, Hydrothermal Synthesis, Crystal Structure and Characterisation of $Na_2ZnP_2O_7 \cdot HCl$, Materials Research Bulletin 38(8), 1309-1317 (2003).

[293] A. E. Lapshin, The Structure of Mixed Alkali-Zinc Diphosphates, Structural Chemistry 27(6), 1641-1646 (2016).

[294] M. A. Petrova, S. A. Petrov, O. Y. Sinel'shchikova, V. F. Popova and V. L. Ugolkov, Electroconductivity of Alkali-Zinc Diphosphates in Partial Sections of the $Zn_2P_2O_7$-$Li_2ZnP_2O_7$-$Na_2ZnP_2O_7$-$K_2ZnP_2O_7$ System, Glass Physics and Chemistry 41(5), 528-532 (2015).

[295] A. E. Lapshin, M. Petrova, Y. N. Osipova, A. S. Novikova and Y. S. Shepelev, Thermal Behavior of Alkali Zinc Phosphates, Glass Physics and Chemistry 31(5), 684-689 (2005).

[296] S. Chouaib, A. B. Rhaiem and G. Kamel, Dielectric Relaxation and Ionic Conductivity Studies of $Na_2ZnP_2O_7$, Bulletin of Materials Science 34(4), 915-920 (2011).

[297] T. Honma, T. Togashi, N. Ito and T. Komatsu, Fabrication of $Na_2FeP_2O_7$ Glass-Ceramics for Sodium Ion Battery, Journal-Ceramic Society Japan 120(1404), 344-346 (2012).

[298] P. Barpanda, T. Ye, J. Lu, Y. Yamada, S. C. Chung, S. Nishimura, M. Okubo, H. Zhou and A. Yamada, Splash Combustion Synthesis and Exploration of Alkali Metal Pyrophosphate ($A_2MP_2O_7$, A = Li, Na) Cathodes, ECS

Transactions 50, 71-77 (2013).

[299] J. Song, J. Yang, M. H. Alfaruqi, W. Park, S. Park, S. Kim, J. Jo and J. Kim, Pyro-Synthesis of $Na_2FeP_2O_7$ Nano-Plates as Cathode for Sodium-Ion Batteries with Long Cycle Stability, Journal of the Korean Ceramic Society 53(4), 406-410 (2016).

[300] C. Tealdi, M. Ricci, C. Ferrara, G. Bruni, V. Berbenni, E. Quartarone and P. Mustarelli, Glucose-Assisted Synthesis and Wet-Chemistry Preparation of Pyrophosphate Cathodes for Rechargeable Na-Ion Batteries, RSC Advances 6(102), 99735-99742 (2016).

[301] J. Cao, L. Ni, C. C. Qin, Y. F. Tang and Y. F. Chen, Synthesis of Hierarchical $Na_2FeP_2O_7$ Spheres with High Electrochemical Performance via Spray Drying, Ionics 23(7), 1783-1791 (2017).

[302] P. Barpanda, T. Ye, S. Nishimura, S. C. Chung, Y. Yamada, M. Okubo, H. Zhou and A. Yamada, Sodium Iron Pyrophosphate: A novel 3.0 V Iron-Based Cathode for Sodium-Ion Batteries, Electrochemistry Communications 24, 116-119 (2012).

[303] C. Y. Chen, K. Matsumoto, T. Nohira, C. Ding, T. Yamamoto and T. Hagiwara, Charge-Discharge Behavior of a $Na_2FeP_2O_7$ Positive Electrode in an Ionic Liquid Electrolyte between 253 and 363 K, Electrochimica Acta 133, 583-588 (2014).

[304] T. Honma, T. Togashi, N. Ito and T. Komatsu, Sodium Iron Phosphate $Na_2FeP_2O_7$ Glass-Ceramics for Sodium Ion Battery, Ceramic Engineering and Science Proceedings 34(9), 33-40 (2014).

[305] Y. H. Jung, C. H. Lim, J. H. Kim and D. K. Kim, $Na_2FeP_2O_7$ as a Positive Electrode Material for Rechargeable Aqueous Sodium-Ion Batteries, TSC Advances 4(19), 9799-9802 (2014).

[306] C. Y. Chen, K. Matsumoto, T. Nohira, R. Hagiwara, Y. Orikasa and Y. Uchimoto, Pyrophosphate $Na_2FeP_2O_7$ as a Low-Cost and High-Performance Positive Electrode Material for Sodium Secondary Batteries Utilizing an Inorganic Ionic Liquid, Journal of Power Sources 246, 783-787 (2014).

[307] P. Barpanda, L. Guandong, C. D. Ling, M. Tamaru, M. Avdeev, S. C. Chung, Y. Yamada and A. Yamada, $Na_2FeP_2O_7$: A Safe Cathode for Rechargeable Sodium-ion Batteries, ChemInform 25(17), 3480-3487 (2013).

[308] H. Kim, R. A. Shakoor, C. Park, S. Y. Lim, J. S. Kim, Y. N. Jo, W. Cho, K. Miyasaka, R. Kahraman, Y. Jung and J. W. Choi, $Na_2FeP_2O_7$ as a Promising Iron-Based Pyrophosphate Cathode for Sodium Rechargeable Batteries: A Combined Experimental and Theoretical Study, Advanced Functional Materials 23(9), 1147-1155 (2013).

[309] J. Ming, H. Ming, W. Yang, W. J. Kwak, J. B. Park, J. Zheng and Y. K. Sun, A Sustainable Iron-Based Sodium Ion Battery of Porous Carbon–Fe_3O_4/$Na_2FeP_2O_7$ with High Performance, RSC Advances 5(12), 8793-8800 (2015).

[310] N. V. Kosova, D. O. Rezepova, O. A. Podgornova, A. B. Slobodyuk, S. A. Petrov and M. Avdeev, A Comparative Study of Structure, Air Sensitivity and

Electrochemistry of Sodium Iron Pyrophosphates $Na_{2-x}Fe_{1+x/2}P_2O_7$ (x = 0; 0.44), Electrochimica Acta 235, 42-55 (2017).

[311] Q. Huang and S. J. Hwu, Synthesis and Characterization of Three New Layered Phosphates, $Na_2MnP_2O_7$, $NaCsMnP_2O_7$, and $NaCsMn_{0.35}Cu_{0.65}P_2O_7$, Inorganic Chemistry 37(22), 5869-5874 (1998).

[312] N. K. Lokanath, M. A. Sridhar, P. J. Sashidhara, G. S. Gopalakrishna and K. G. Ashamanjari, Synthesis and Structural Characterization of $Na_2MnP_2O_7$ Crystal, Bulletin of Materials Science 23(3), 175-178 (2000).

[313] M. Tanabe, T. Honma and T. Komatsu, Unique Crystallization Behavior of Sodium Manganese Pyrophosphate $Na_2MnP_2O_7$ Glass and its Electrochemical Properties, Journal of Asian Ceramic Societies 5, 209-215 (2017).

[314] P. Barpanda, T. Ye, M. Avdeev, S. C. Chung and A. Yamada, A New Polymorph of $Na_2MnP_2O_7$ as a 3.6 V Cathode Material for Sodium-Ion Batteries, Journal of Materials Chemistry A 1(13), 4194-4197 (2013).

[315] C. S. Park, H. Kim, R. A. Shakoor, E. Yang, S. Y. Lim, R. Kahraman, Y. Jung and J. W. Choi, Anomalous Manganese Activation of a Pyrophosphate Cathode in Sodium Ion Batteries: A Combined Experimental and Theoretical Study, Journal of the American Chemical Society 135(7), 2787-2792 (2013).

[316] J. M. Clark, P. Barpanda, A. Yamada and M. S. Islam, Sodium-Ion Battery Cathodes $Na_2FeP_2O_7$ and $Na_2MnP_2O_7$: Diffusion Behaviour for High Rate Performance, Journal of Materials Chemistry A 2(30), 11807-11812 (2014).

[317] R. A. Shakoor, C. S. Park, A. A. Raja, J. Shin and R. Kahraman, A Mixed Iron-Manganese Based Pyrophosphate Cathode, $Na_2Fe_{0.5}Mn_{0.5}P_2O_7$, for Rechargeable Sodium Ion Batteries, Physical Chemistry Chemical Physics 18(5), 3929-3935 (2016).

[318] A. E. Lapshin and M. A. Petrova, Mixed Alkali-Zinc Diphosphates: Synthesis, Structure, and Properties, Glass Physics and Chemistry 38(6), 491-503 (2013).

[319] L. Gacem, E. Artemenko, D. Ouadjaout, J. P. Chaminade, A. Garcia, M. Pollet and O. Viraphong, ESR and Fluorescence Studies of Mn-Doped $Na_2ZnP_2O_7$ Single Crystal and Glasses, Solid State Sciences 11(11), 1854-1860 (2009).

[320] T. Honma, N. Ito, T. Togashi, A. Sato and T. Komatsu, Triclinic $Na_{2-x}Fe_{1+x/2}P_2O_7$/C Glass-Ceramics with High Current Density Performance for Sodium Ion Battery, Journal of Power Sources 227, 31-34 (2013).

[321] N. V. Kosova, A. M. Tsapina, A. B. Slobodyuk and S. A. Petrov, Structure and Electrochemical Properties of Mixed Transition-Metal Pyrophosphates $Li_2Fe_{1-y}Mn_yP_2O_7$ ($0 \leq y \leq 1$), Electrochimica Acta 174, 1278-1289 (2015).

[322] P. Barpanda, G. Liu, Z. Mohamed, C. D. Ling and A. Yamada, Structural, Magnetic and Electrochemical Investigation of Novel Binary $Na_{2-x}(Fe_{1-y}Mn_y)P_2O_7$ ($0 \leq y \leq 1$) Pyrophosphate Compounds for Rechargeable Sodium-Ion Batteries, Solid State Ionics 268, 305-311 (2014).

[323] R. A. Shakoor, R. Kahraman and A. A. Raja, Thermal Insitu Analyses of Multicomponent Pyrophosphate Cathodes Materials, International Journal of Electrochemical Science 10, 8941-8950 (2015).

[324] B. Zhang, R. Tan, L. Yang, J. Zheng, K. Zhang, S. Mo, Z. Lin and F. Pan, Mechanisms and Properties of Ion-Transport in Inorganic Solid Electrolytes, Energy Storage Materials 10, 139-159 (2018).

[325] F. A. Kroger and H. J. Vink, Relations between the Concentrations of Imperfections in Crystalline Solids, Solid State Physics 3, 307-435 (1956).

[326] T. Kudo and K. Fueki, Solid State Ionics, Tokyo: Kodansha Ltd. (1990).

[327] P. Kofstad and T. Norby, Defects and Transport in Crystalline Solids, Oslo: University of Oslo (2007).

[328] S. T. Myung, N. Kumagai, S. Komaba and H. T. Chung, Effects of Al Doping on the Microstructure of $LiCoO_2$ Cathode Materials, Solid State Ionics 139(1-2), 47-56 (2001).

[329] R. Amin, C. Lin and J. Maier, Aluminium-Doped $LiFePO_4$ Single Crystals, Physical Chemistry Chemical Physics 10(24), 3524-3529 (2008).

[330] H. L. Tuller and S. R. Bishop, Point Defects in Oxides: Tailoring Materials Through Defect Engineering, Annual Review of Materials Research 41, 369-398 (2011).

[331] S. Shi, P. Lu, Z. Liu, I. Qi, L. G. Hector Jr, H. Li and S. J. Harris, Direct Calculation of Li-Ion Transport in the Solid Electrolyte Interphase, Journal of the American Chemical Society 134(37), 15476-15487 (2012).

[332] S. Shi, Y. Qi, H. Li and L. G. Hector Jr, Defect Thermodynamics and Diffusion Mechanisms in Li_2CO_3 and Implications for the Solid Electrolyte Interphase in Li-Ion Batteries, The Journal of Physical Chemistry C 117(17), 8579-8593 (2013).

[333] R. P. Buck, Transport Properties of Ionic Conductors, Sensors and Actuators 1, 137-196 (1981).

[334] J. B. Goodenough, Oxide-Ion Electrolytes, Annual Review of Materials Research 33, 91-128 (2003).

[335] J. T. Krummer, β-Alumina Electrolytes, Progress in Solid State Chemistry 7, 141-175 (1972).

[336] J. C. Bachman, S. Muy, A. Grimaud, H. H. Chang, N. Pour, S. F. Lux, O. Paschos, F. Maglia, S. Lupart, P. Lamp, L. Giordano and Y. S. Horn, Inorganic Solid-State Electrolytes for Lithium Batteries: Mechanisms and Properties Governing Ion Conduction, Chemical Reviews 116(1), 140-162 (2015).

[337] D. B. McWhan, S. J. Alens, J. P. Remeika and P. D. Dernier, Ion-Ion Correlations and Diffusion in β-Alumina, Physical Review Letters 35(14), 953-956 (1975).

[338] J. Gao, Y. S. Zhao, S. Q. Shi and H. Li, Lithium-Ion Transport in Inorganic Solid State Electrolyte, Chinese Physics B 25(1), 018211 (2016).

[339] S. Stramare, V. Thangadurai and W. Weppner, Lithium Lanthanum Titanates: A Review, Chemistry of Materials 15(21), 3974-3990 (2003).

[340] H. Kawai and J. Kuwano, Lithium Ion Conductivity of A-Site Deficient Perovskite Solid Solution $La_{0.67-x}Li_{3x}TiO_3$, Journal of The Electrochemical

Society 141(7), L78-L79 (1994).

[341] A. M. Juarez, C. Pecharroman, J. E. Iglesias and J. M. Rojo, Relationship Between Activation Energy and Bottleneck Size for Li^+ Ion Conduction in NASICON Materials of Composition $LiMM'(PO_4)_3$; M, M' = Ge, Ti, Sn, Hf, The Journal of Physical Chemistry B 102(2), 372-375 (1998).

[342] R. Tarneberg and A. Lund, Ion Diffusion in the High-Temperature Phases Li_2SO_4, $LiNaSO_4$, $LiAgSO_4$ and $Li_4Zn(SO_4)_3$, Solid State Ionics 90(1-4), 209-220 (1996).

[343] Y. Wang, W. D. Richards, S. P. Ong, L. J. Miara, J. C. Kim, Y. Mo and G. Ceder, Design Principles for Solid-State Lithium Superionic Conductors, Nature Materials 14(10), 1026-1032 (2015).

[344] A. R. Rodger, J. Kuwano and A. R. West, Li^+ Ion Conducting γ Solid Solutions in the Systems Li_4XO_4-Li_3YO_4: X=Si, Ge, Ti; Y=P, As, V; Li_4XO_4-$LiZO_2$: Z=Al, Ga, Cr and Li_4GeO_4-Li_2CaGeO_4, Solid State Ionics 15(3), 185-198 (1985).

[345] Y. W. Hu, I. D. Raistrick and R. A. Huggins, Ionic Conductivity of Lithium Orthosilicate-Lithium Phosphate Solid Solutions, Journal of The Electrochemical Society 124(8), 1240-1242 (1977).

[346] A. Khorassani and A. R. West, New Li^+ Ion Conductors in the System Li_4SiO_4–Li_3AsO_4, Solid State Ionics 7(1), 1-8 (1982).

[347] A. Khorassani and A. R. West, Li^+ Ion Conductivity in the System Li_4SiO_4-Li_3VO_4, Journal of Solid State Chemistry 53(3), 369-375 (1984).

[348] M. Itoh, Y. Inaguma, W. H. Jung, L. Chen and T. Nakamura, High Lithium Ion Conductivity in the Perovskite-Type Compounds $Ln_{12}Li_{12}TiO_3$ (Ln=La,Pr,Nd,Sm), Solid State Ionics 70-71(1), 203-207 (1994).

[349] K. Meier, T. Laino and A. Curioni, Solid-State Electrolytes: Revealing the Mechanisms of Li-Ion Conduction in Tetragonal and Cubic LLZO by First-Principles Calculations, The Journal of Physical Chemistry C 118(13), 6668-6679 (2014).

[350] S. Adams and R. P. Rao, Ion Transport and Phase Transition in $Li_{7-x}La_3(Zr_{2-x}M_x)O_{12}$ (M = Ta^{5+}, Nb^{5+}, x = 0, 0.25), Journal of Materials Chemistry 22(4), 1426-1434 (2012).

[351] N. Bernstein, M. D. Johannes and K. Hoang, Origin of the Structural Phase Transition in $Li_7La_3Zr_2O_{12}$, Physical Review Letters 109, 205702 (2012).

[352] E. Rangasamy, J. Wolfenstine and J. Sakamoto, The Role of Al and Li Concentration on the Formation of Cubic Garnet Solid Electrolyte of Nominal Composition $Li_7La_3Zr_2O_{12}$, Solid State Ionics 206, 28-32 (2012).

[353] R. Murugan, S. Ramakumar and N. Janani, High Conductive Yttrium Doped $Li_7La_3Zr_2O_{12}$ Cubic Lithium Garnet, Electrochemistry Communications 13(12), 1373-1375 (2011).

[354] H. E. Shinawi and J. Janek, Stabilization of Cubic Lithium-Stuffed Garnets of the Type $Li_7La_3Zr_2O_{12}$ by Addition of Gallium, Journal of Power Sources 225, 13-19 (2013).

[355] H. J. Deiseroth, S. T. Kong, H. Eckert, J. Vannahme, C. Reiner, T. Zaiss and M. Schlosser, Li_6PS_5X: A Class of Crystalline Li-Rich Solids with an Unusually High Li^+ Mobility, Angewandte Chemie International Edition 47(4), 755-758 (2008).

[356] A. Hayashi, K. Noi, A. Sakuda and M. Tatsumisago, Superionic Glass-Ceramic Electrolytes for Room-Temperature Rechargeable Sodium Batteries, Nature Communications 3(859), 1-5 (2012).

[357] N. Tanibata, K. Noi, A. Hayashi, N. Kitamura, Y. Idemoto and M. Tatsumisago, X-ray Crystal Structure Analysis of Sodium-Ion Conductivity in $94Na_3PS_4{\cdot}6Na_4SiS_4$ Glass-Ceramic Electrolytes, ChemElectroChem 1(7), 1130-1132 (2014).

[358] A. G. Belous, G. N. Novitskaya, S. V. Polyanetskaya and Y. I. Gornikov, Study of Complex Oxides of Composition $La_{2/3-x}Li_{3x}TiO_3$, Neorganiceskie Materialy 23(3), 470-472 (1987).

[359] O. Bohnke, C. Bohnke and J. L. Fourquet, Mechanism of Ionic Conduction and Electrochemical Intercalation of Lithium into the Perovskite Lanthanum Lithium Titanate, Solid State Ionics 91(1-2), 21-31 (1996).

[360] A. Rivera, C. Leon, J. Santamaria, A. Varez, O. V'yunov, A. G. Belous, J. A. Alonso and J. Sanz, Percolation-Limited Ionic Diffusion in $Li_{0.5-x}Na_xLa_{0.5}TiO_3$ Perovskites ($0 \leq x \leq 0.5$), Chemistry of Materials 14(12), 5148-5152 (2002).

[361] J. Sanz, A. Rivera, C. Leon, J. Santamaria, A. Varez, A. G. Belous and O. V'yunov, Li Mobility in $(Li,Na)_yLa_{0.66-y/3}TiO_3$ Perovskites ($0.09 < y < 0.5$). A Model System for the Percolation Theory, Materials Research Society Proc. 756, EE2.31-EE2.36 (2003).

[362] C. P. Herrero, A. Varez, A. Rivera, J. Santamaria, C. Leon, O. V'yunov, A. G. Belous and J. Sanz, Influence of Vacancy Ordering on the Percolative Behavior of $(Li_{1-x}Na_x)_{3y}La_{2/3-y}TiO_3$ Perovskites, The Journal of the Physical Chemistry B 109(8), 3262-3268 (2005).

[363] A. G. Belous, Properties of Lithium Ion-Conducting Ceramics Based on Rare-Earth Titanates, Ionics 4(5-6), 360-363 (1998).

[364] O. Bohnke, The Fast Lithium-Ion Conducting Oxides $Li_{3x}La_{2/3-x}TiO_3$ from Fundamentals to Application, Solid State Ionics 179(1-6), 9-15 (2008).

[365] O. Bohnke, J. Emery and J. L. Fourquet, Anomalies in Li^+ Ion Dynamics Observed by Impedance Spectroscopy and ^7Li NMR in the Perovskite Fast Ion Conductor $(Li_{3x}La_{2/3-x}\square_{1/3-2x})TiO_3$, Solid State Ionics 158(1-2), 119-132 (2003).

[366] O. Bohnke, J. Emery, A. Veron, J. L. Fourquet, J. Y. Buzare, P. Florian and D. Massiot, A Distribution of Activation Energies for the Local and Long-Range Ionic Motion is Consistent with the Disordered Structure of the Perovskite $Li_{3x}La_{2/3-x}TiO_3$, Solid State Ionics 109(1-2), 25-34 (1998).

[367] A. Belous, E. Pashkova, O. Gavrilenko, O. V'yunov and L. Kovalenko, Solid Electrolytes Based on Lithium-Containing Lanthanum Metaniobates, Journal of the European Ceramic Society 24(6), 1301-1304 (2004).

[368] A. Belous, E. Pashkova, O. Gavrilenko, O. V'yunov and L. Kovalenko, Solid

Electrolytes Based on Lithium-Containing Lanthanum Metaniobates and Metatantalates with Defect-Perovskite Structure, Ionics 9(1-2), 21-27 (2003).

[369] A. Belous, O. Gavrilenko, O. Pashkova, O. Bohnke and C. Bohnke, Structural Peculiarities and Electrophysical Properties of Lithium Ion Conducting Lanthanum Niobate Prepared by Solid-State Reaction and Precipitation from Solution, European Journal of Inorganic Chemistry 2008(30), 4792-4796 (2008).

[370] A. G. Belous, O. N. Gavrilenko, O. I. V'yunov, S. D. Kobilyanskaya and V. V. Trachevskii, Effect of Isovalent Substitution on the Structure and Ionic Conductivity of $Li_{0.5-y}Na_yLa_{0.5}\square Nb_2O_6$, Inorganic materials 47(3), 308-312 (2011).

[371] S. D. Kobylianska, O. I. V'yunov, A. G. Belous and O. Bohnke, Lithium Ion Conductors Based on System (Li,Na,La){Ti,Nb,Ta}O with Perovskite Structure, Solid State Phenomena 200, 279-285 (2013).

[372] R. Jimenez, V. Diez, J. Sanz, S. D. Kobylianska, O. I. V'yunov and A. G. Belous, Evidence for Changes on the Lithium Conduction Dimensionality of $Li_{0.5-y}Na_yLa_{0.5}Nb_2O_6$ ($0 \leq y \leq 0.5$) Perovskites, RSC Advances 5(35), 27912-27921 (2015).

[373] A. D. Robertson, A. R. West and A. G. Ritchie, Review of Crystalline Lithium-Ion Conductors Suitable for High Temperature Battery Applications, Solid State Ionics 104(1-2), 1-11 (1997).

[374] S. Megahed and B. Scrosati, Lithium-Ion Rechargeable Batteries, Journal of Power Sources 51(1-2), 79-104 (1994).

[375] D. W. Murphy and P. A. Christian, Solid State Electrodes for High Energy Batteries, Science 205(4407), 651-656 (1979).

[376] P. Simon and Y. Gogotsi, Materials for Electrochemical Capacitors, Nature Materials 7, 845-854 (2008).

[377] S. M. Haile, Materials for Fuel Cells, Materials Today 6(3), 24-29 (2003).

[378] K. Funke, AgI-Type Solid Electrolytes, Progress in Solid State Chemistry 11(4), 345-402 (1976).

[379] P. Lacorre, F. Goutenoire, O. Bohnke, R. Retoux and Y. Laligant, Designing Fast Oxide-Ion Conductors Based on $La_2Mo_2O_9$, Nature 404, 856-858 (2000).

[380] T. Takahashi, H. Iwahara and Y. Nagai, High Oxide Ion Conduction in Sintered Bi_2O_3 Containing SrO, CaO or La_2O_3, Journal of Applied Electrochemistry 2(2), 97-104 (1972).

[381] J. B. Goodenough, Ceramic Solid Electrolytes, Solid State Ionics 94(1-4), 17-25 (1997).

[382] T. Salkus, A. Kezionis, E. Kazakevicius, A. Dindune, Z. Kanape, J. Ronis, O. Bohnke, V. Kazlauskiene, J. Miskinis, M. Lelis and A. F. Orliukas, Preparation and Characterization of $Li_{2.9}Sc_{1.9-y}Y_yZr_{0.1}(PO_4)_3$ (where y = 0, 0.1) Solid Electrolyte Ceramics, Phase Transitions 83(8), 581-594 (2010).

[383] S. E. Sigaryov, E. A. Genkina and B. A. Maximov, Some Features of Li^+-Ion Distribution in Monoclinic Modifications of $Li_3M_2(PO_4)_3$ (M=Sc, Fe, In)

Superionic Conductors, Solid State Ionics 37(4), 261-265 (1990).

[384] O. Bohnke, J. C. Badot and J. Emery, Broadband Dielectric Spectroscopy Study of Li^+ Ion Motions in the Fast Ionic Conductor $Li_{3x}La_{2/3-x}TiO_3$ (x = 0.09); Comparison with ^7Li NMR Results, Journal of Physics Condensed Matter 15(44), 7571-7584 (2003).

[385] S. Raz, K. Sasaki, J. Maier and I. Riess, Characterization of Adsorbed Water Layers on Y_2O_3-doped ZrO_2, Solid State Ionics 143(2), 181-204 (2001).

[386] M. Shirpour, G. Gregori, R. Merkle and J. Maier, On the Proton Conductivity in Pure and Gadolinium Doped Nanocrystalline Cerium Oxide, Physical Chemistry Chemical Physics 13(3), 937-940 (2011).

[387] H. Takamura and N. Takahashi, Electrical Conductivity of Dense Nanocrystalline Ceria Under Humidified Atmosphere, Solid State Ionics 181(3-4), 100-103 (2010).

[388] A. B. Yaroslavtsev, Proton Conductivity of Inorganic Hydrates, Russian Chemical Reviews 63(5), 449-455 (2007).

[389] I. A. Stenina and A. B. Yaroslavtsev, Low and Intermediate Temperature Proton-Conducting Electrolytes, Inorganic Materials 53(3), 241-251 (2017).

[390] S. Cukierman, Et tu, Grotthuss! And Other Unfinished Stories, Biochimica et Biophysica Acta 1757(8), 876-885 (2006).

[391] T. J. T. Grotthuss, Sur la décomposition de l'eau et des corps q'uelle tient en dissolution à l'aide de l'électricité galvanique (in French), Annales de Chimie LVIII, 54-74 (1806).

[392] D. L. Nelson and M. M. Cox, Principles of Biochemistry, 5th ed., New York: W. H. Freeman and Company (2008).

[393] N. Agmon, The Grotthuss Mechanism, Chemical Physics Letters 244(5-6), 456-462 (1995).

[394] G. E. Walrafen, M. R. Fisher, M. Hokmabadi and W. H. Yang, Temperature Dependence of the Low and High Frequency Raman Scattering from Liquid Water, The Journal of Chemical Physics 85(12), 6970-6982 (1986).

[395] Y. Jin, Y. Shen and T. Hibino, Proton Conduction in Metal Pyrophosphates (MP_2O_7) at Intermediate Temperatures, Journal of Materials Chemistry 20(30), 6214-6217 (2010).

[396] T. Shirai, S. Satou, Y. Saito, M. Saito, J. Kuwano and H. Shiroishi, Proton Conducting Solid Electrolytes Based on Diphosphates, Phosphorous Research Bulletin 21, 31-37 (2007).

[397] M. Ermrich and D. Opper, X-ray Powder Diffraction. XRD for the Analyst. Getting acquainted with the principles, 2nd ed., Almelo: PANalytical B.V. (2013).

[398] K. Christmann, Introduction to Surface Physical Chemistry, New York: Steinkopff Verlag, Darmastdt, Springer-Verlag (1991).

[399] D. Lexa and L. Leibowitz, Differential Thermal Analysis and Differential Scanning Calorimetry, in “Characterization of Materials”, John Wiley & Sons (2003).

[400] A. W. Coats and J. P. Redfern, Thermogravimetric Analysis. A review, Analyst 88(1053), 906-924 (1963).

[401] E. Barsoukov and J. R. Macdonald, Impedance Spectroscopy: Theory, Experiment, and Applications, 2nd ed., New Jersey: A John Wiley & Sons, Inc. (2005).

[402] W. Bogusz and F. Krok, Elektrolity State (in Polish), Warsaw: Wydawnictwa Naukowo-Techniczne (1995).

[403] V. F. Lvovich, Impedance Spectroscopy: Applications to Electrochemical and Dielectric Phenomena, New Jersey: A John Wiley & Sons, Inc. (2012).

[404] F. Kremer and A. Schonhals, Eds., Broadband Dielectric Spectroscopy, New York: Springer-Verlag Berlin Heidelberg (2003).

[405] J. E. Bauerle, Study of Solid Electrolyte Polarization by a Complex Admittance Method, Journal of Physics and Chemistry of Solids 30(12), 2657-2670 (1969).

[406] A. K. Jonscher, Dielectric Relaxation in Solids, London: Chelsea Dielectrics Press (1996).

[407] A. F. Orliukas, A. Kezionis and E. Kazakevicius, Impedance Spectroscopy of Solid Electrolytes in the Radio Frequency Range, Solid State Ionics 176(25-28), 2037-2043 (2005).

[408] A. Kezionis, E. Kazakevicius, T. Salkus and A. F. Orliukas, Broadband High Frequency Impedance Spectrometer with Working Temperatures up to 1200 K, Solid State Ionics 188(1), 110-113 (2011).

[409] D. Blackham, Calibration Method for Open-Ended Coaxial Probe/Nector Network Analyzer System, Materials Research Society Symposium Proceedings 269, 595-599 (1992).

[410] O. M. Andrade, M. F. Iskander and S. Bringhurst, High Temperature Broadband Dielectric Properties Measurement Techniques, Materials Research Society Symposium Proceedings 269, 527-539 (1992).

[411] M. Arai, J. G. P. Binner, G. E. Carr and T. E. Cross, High Temperature Dielectric Measurements on Ceramics, Materials Research Society Symposium Proceedings 269, 611-616 (1992).

[412] M. Arai, J. G. P. Binner and T. E. Cross, Comparison of Techniques for Measuring High-Temperature Microwave Complex Permittivity: Measurements on an Alumina/Zircona System, The Journal of Microwave Power and Electromagnetic Energy 21(1), 12-18 (1996).

[413] S. Bringhurst and M. F. Iskander, Open-Ended Metallized Ceramic Coaxial Probe for High-Temperature Dielectric Properties Measurements, IEEE Transactions on Microwave Theory and Techniques 44(6), 926-935 (1996).

[414] A. Kezionis, P. Butvilas, T. Salkus, S. Kazlauskas, D. Petrulionis, T. Zukauskas, E. Kazakevicius and A. F. Orliukas, Four-Electrode Impedance Spectrometer for Investigation of Solid Ion Conductors, Review of Scientific Instruments 84(1), 013902 (2013).

[415] A. F. Orliukas, A. Kezionis, V. Mikucionis and R. Vaitkus, LF, HF, and

Microwave Techniques for Studying Superionic Conductors, Electrochimija 23(1), 98 (1987).

[416] A. Kezionis, A. F. Orliukas, K. Paulavicius and V. Samulionis, Methods for Determination of Electrical and Acoustic Properties of Superionics and Mixed Ionic-Electronic Conductors, Materials Science Forum 76, 229-232 (1991).

[417] A. Kezionis and S. Kazlauskas, High Temperature Ultra Broadband Impedance Spectrometer, in International Impedance Spectroscopy Workshop, Chemnitz, Germany (2013).

[418] A. Kezionis, S. Kazlauskas, D. Petrulionis and A. F. Orliukas, Broadband Method for the Determination of Small Sample's Electrical and Dielectric Properties at High Temperatures, IEEE Transactions of Microwave Theory and Techniques 62(10), 2456-2461 (2014).

[419] M. N. M. Kehn, L. Shafai and S. Noghanian, Permittivity Measurement of Disk and Annular Dielectric Samples Using Coaxial Transmission Line Fixtures. Part I: Theory and Formulation, Canadian Journal of Electrical and Computer Engineering 34(1-2), 21-29 (2009).

[420] J. Banys, S. Lapinskas, S. Rudys, S. Greicius and R. Grigalaitis, High Frequency Measurements of Ferroelectrics and Related Materials on Coaxial Line, Ferroelectrics 414(1), 64-69 (2011).

[421] J. Bennazha, F. Erragh, A. Boukhari and E. M. Holt, Identification of a New Family of Diphosphate Compounds, $A^{I}_{2}B^{II}_{3}(P_2O_7)_2$: Structures of $Ag_2Co_3(P_2O_7)_2$, $Ag_2Mn_3(P_2O_7)_2$, and $Na_2Cd_3(P_2O_7)_2$, Journal of Chemical Crystallography 30(11), 705-716 (2000).

[422] H. Liu, Y. Zhao, H. Zhang, X. Lian, Y. Dong and Q. Kuang, Structural and Electrochemical Properties of Fe-Doped $Na_2Mn_{3-x}Fe_x(P_2O_7)_2$ Cathode Material for Sodium Ion Batteries, Journal of Power Sources 370, 114-121 (2017).

[423] М. С. Слободяник, П. Г. Нагорний and Р. С. Бойко, Кристалічна будова подвійного дифосфату $Na_2Mn_3(P_2O_7)_2$ (in Ukrainian), Доповіді На¨¨іональної академії наук України 12, 12, 114-119 (2013).

[424] B. S. Geller and J. L. Durand, Refinement of the Structure of $LiMnPO_4$, Acta Crystallographica 13, 325-331 (1960).

[425] S. Daugela, T. Salkus, A. Kezionis, V. Venckute, D. Valdniece, A. Dindune, M. Barre and A. F. Orliukas, Anomalous Temperature-Dependent Electrical Properties of $Na_2MnP_2O_7$, Solid State Ionics 302, 72-76 (2017).

[426] A. F. Orliukas, V. Venckute, S. Daugela, A. Kezionis, A. Dindune, D. Valdniece, J. Ronis, M. Lelis, M. Mosialek and T. Salkus, Synthesis, Structure and Impedance Spectroscopy of $NaCsZn_{0.5}Mn_{0.5}P_2O_7$ Pyrophosphate Ceramics, Solid State Ionics 302, 92-97 (2017).

[427] V. D. Castro and G. Polzonetti, XPS Study of MnO Oxidation, Journal of Electron Spectroscopy and Related Phenomena 48(1), 117-123 (1989).

[428] R. P. Gupta and S. K. Sen, Calculation of Multiplet Structure of Core p-vacancy Levels, Physical Review B 10(1), 71-77 (1974).

[429] H. W. Nesbitt and D. Banerjee, Interpretation of XPS Mn(2p) Spectra of Mn

Oxyhydroxides and Constraints on the Mechanism of MnO_2 Precipitation, American Mineralogist 83(3-4), 305-315 (1998).

[430] C. N. R. Rao, D. D. Sarma, S. Vasudevan and M. S. Hegde, Study of Transition Metal Oxides by Photoelectron Spectroscopy, Proceedings of the Royal Society of London A 367(1729), 239-262 (1979).

[431] N. S. McIntyre and D. G. Zetaruk, X-ray Photoelectron Spectroscopic Studies of Iron Oxides, Analytical Chemistry 49(11), 1521-1529 (1977).

[432] A. R. Pratt, I. J. Muir and H. W. Nesbitt, X-ray Photoelectron and Auger Electron Spectroscopic Studies of Pyrrhotite and Mechanism of Air Oxidation, Geochimica et Cosmochimica Acta 58(2), 827-841 (1994).

[433] J. C. Dyre, P. Maass, B. Roling and D. L. Sidebottom, Fundamental Questions Relating to Ion Conduction in Disordered Solids, Reports on Progress in Physics 72(4), 046501 (2009).

[434] E. Kazakevičius, A. Kezionis, L. Zukauskaite, M. Barre, T. Salkus, A. Zalga, A. Selskis and A. F. Orliukas, Characterization of $Na_{1.3}Al_{0.3}Zr_{1.7}(PO_4)_3$ Solid Electrolyte Ceramics by Impedance Spectroscopy, Solid State Ionics 271, 128-133 (2015).

[435] E. Kazakevicius, A. Kezionis, L. Zukauskaite, M. Barre, T. Salkus and A. F. Orliukas, Characterization of NASICON-type Na Solid Electrolyte Ceramics by Impedance Spectroscopy, Functional Materials Letters 7(6), 1440002 (2014).

[436] W. Bogusz, J. R. Dygas, F. Krok, A. Kezionis, R. Sobiestianskas, E. Kazakevicius and A. F. Orliukas, Electrical Conductivity Dispersion in Co-Doped NASICON Samples, Physica Status Solidi A 183(2), 323-330 (2001).

[437] X. Sun, S. Wang, Z. Wang, X. Ye, T. Wen and F. Huang, Proton Conductivity of CeP_2O_7 for Intermediate Temperature Fuel Cells, Solid State Ionics 179(21-26), 1138-1141 (2008).

[438] B. Klinkert, M. Jansen and Z. Anorg, Darstellung und Kristallstruktur von $Cs_2Mn(PO_3)_4$ (in German), Journal of Inorganic and general Chemistry 570(1), 102-108 (1998).

[439] V. Venckute, P. Dobrovolskis, T. Salkus, A. Kezionis, A. Dindune, Z. Kanape, J. Ronis, K. Z. Fung and A. F. Orliukas, Preparation and Characterization of Solid Electrolytes Based on TiP_2O_7 Pyrophosphate, Ferroelectrics 479(1), 101-109 (2015).

[440] S. Villain, E. Nigrelli and G. Nihoul, Ionic Conductivity of Pure Sodium Pyrophosphate $Na_4P_2O_7$, Solid State Ionics 116(1-2), 73-83 (1999).

[441] G. S. Gopalakrishna, M. J. Mahesh, K. G. Ashamanjari and J. Shashidharaprasad, Hydrothermal Synthesis, Morphological Evolution and Characterization of $Na_2CoP_2O_7$ Crystals, Journal of Crystal Growth 281(2-4), 604-610 (2005).

[442] A. Piecha, G. Bator and R. Jakubas, Critical Slowing Down of Low-Frequency Dielectric Relaxation in Ferroelectric $(C_3N_2H_5)_5Bi_2Cl_{11}$, Journal of Physics: Condensed Matter 17(41), L411-L417 (2005).

[443] A. Niemer, R. Pankrath, K. Betzler, M. Burianek and M. Muehlberg, Dielectric Properties and the Phase Transition of Pure and Cerium Doped Calcium-Barium-Niobate, World Journal of Condensed Matter Physics 2(2), 80-84 (2012).

[444] Y. Okada, M. Ikeda and M. Aniya, Non-Arrhenius Ionic Conductivity in Solid Electrolytes: A Theoretical Model and its Relation with the Bonding Nature, Solid State Ionics 281, 43-48 (2015).

LIST OF PUBLICATIONS

1. S. Daugėla, T. Šalkus, A. Kežionis, V. Venckutė, D. Valdniece, D. Dindune, M. Barre, A. F. Orliukas. *Anomalous temperature dependences of $Na_2MnP_2O_7$ electrical properties*. Solid State Ionics 302, 72-76 (2017).
2. S. Daugėla, A. Kežionis, T. Šalkus, A. F. Orliukas, A. G. Belous, O. I. V'yunov, S. D. Kobylianska, L.O. Vasylechko. *Peculiarities of ionic conduction in $Li_{0.5-y}Na_yLa_{0.5}Nb_2O_6$ system at high temperatures.* Solid State Ionics 300, 86-90 (2017).
3. A. F. Orliukas, V. Venckutė, S. Daugėla, A. Kežionis, A. Dindune, D. Valdniece, J. Ronis, M. Lelis, M. Mosiałek, T. Šalkus. *Synthesis, structure and impedance spectroscopy of $NaCsZn_{0.5}Mn_{0.5}P_2O_7$ pyrophosphate ceramics*. Solid State Ionics 302, 92-97 (2017).
4. V. Venckutė, A. Dindune, D. Valdniece, A. Krumina, M. Lelis, V. Jasulaitienė, A. Maneikis, S. Daugėla, T. Šalkus, A. Kežionis. *Preparation, structure, surface and impedance analysis of $Na_2Zn_{0.5}Mn_{0.5}P_2O_7$ ceramics*. Lithuanian Journal of Physics 57(3), 183-193 (2017).

NOTES

NOTES

Vilnius University Press
Sauletekio ave. 9, 10222 Vilnius
e-mail info@leidykla.vu.lt,
www.leidykla.vu.lt
Print run copies 20